High Resolution Flood Illumination Retinal Imaging System with Adaptive Optics

by Marwan Suheimat

Supervisor: Chris Dainty

A thesis submitted in partial fulfilment of the requirements for the degree of Doctor of Philosophy,

School of Physics, Science Faculty,
National University of Ireland, Galway

April 2012

ABSTRACT

Retinal imaging has its advantages both in the research laboratory and medical applications. Acquiring high resolution *in-vivo* images of the retina requires some form of correction for aberrations. To address that, the field of adaptive optics was adopted from astronomy over a decade ago. High resolution retinal imaging has been achieved using more than one imaging modality coupled with adaptive optics; however, the high cost associated with building those instruments has confined them to research laboratory until now. Retinal imaging instruments could assist in early diagnosis of certain progressive retinal pathologies, which increases the chances of impeding their progress, and therefore, saving the visual function of some patients. To fully achieve this potential, such instruments must be made accessible to more people.

The aim of this project is to design and build an adaptive optics assisted retinal imaging system that is affordable to optometrists. The goal is to image a 4° field-of-view on the retina, with the capability to resolve single cones near the fovea. The approach to cost minimisation was to use commercial off-the-shelf optical elements, light emitting diodes to replace current illumination techniques, and a potentially lower cost deformable mirror. Once the preliminary results were acquired, the retinal imaging system was designed and optimised using Zemax. The optimised setup was then built and the control algorithms were written using Labview. The level of detail achieved using the built instrument is discussed in this thesis. This project is a proof-of-concept, and serves as a first step toward building a commercial instrument. This thesis explains the optical design issues and the computer algorithms involved in building the retinal imaging system. We conclude with a few improvement suggestions for the next step in the design process.

CONTENTS

LIST OF TABLES

LIST OF FIGURES

ACKNOWLEDGEMENTS

This research is supported by Science Foundation Ireland (07/IN.1/I906).

First and foremost, I would like to express my gratitude towards Prof. Chris Dainty. Thank you for being a brilliant mentor and friend throughout the PhD programme.

To my friends and colleagues at NUI Galway: thank you for all the good times, interesting discussions (science and otherwise), taking the time out to help me with my project, and sitting as subjects. You have been amazing. Special thanks go to Mehdi Bahrami, Dr. Derek Coburn, Elie DeLestrange, Dr. Nicholas Devaney, Dr. Liz Daly, Dr. Alexander Goncharov, Dr. Conor Leahy, Emer McHugh, Dr. Andrew O'Brien, Margaret O'Halloran, Gomathy Ramaswamy, and Matt Sheehan for their continuous support.

To my friends and colleagues outside NUI Galway, or those who were here at a certain point in history: your contribution to my life and thesis is much appreciated as well. Special thanks go to Dr. Dirk De Brouwere, Tom Brennan, Dr. Karine Chamaillard, Sabine Chiesa, Dr. Eugénie Dalimier, Dr. Adam Dubis, Dr. Alfredo Dubra, Dr. Hamid Fallah, Zachary Harvey, Dr. Andrew Lambert, Dr. Charles-Edouard Leroux, Dr. Eric Logean, Dr. Ruth Mackey, Dr. Erez Ribak.

I am grateful to Prof. Larry Thibos for supplying the model for the simulation we ran in the thesis. I am grateful to our collaborators in the Ophthalmology Department at University College Hospital, Galway with special thanks to Dr Eamonn O'Donoghue.

To my previous professors and lecturers throughout my studies, I am very grateful as I would not be here without the knowledge and list of transferrable skills you have equipped me with.

I consider myself blessed with the love and empathy of family and friends throughout this research process. They have shown nothing less than I expected. In fact, although it had to be a long distance relationship, I have never been given the opportunity to feel left out of their daily life.

I. LIST OF ABBREVIATIONS

AMD	age-related macular degeneration
AO	adaptive optics
BAOSO	broadband adaptive optics scanning ophthalmoscope
BMC	Boston Micromachines Corporation
CCD	charge-coupled device
CMOS	complementary metal-oxide-semiconductor
DM	deformable mirror
FOV	field-of-view
FPGA	field programmable gate array
GS	guide star
HOA	higher-order aberrations
LCA	longitudinal chromatic aberration
LC-SLM	liquid crystal spatial light modulator
LED	light-emitting diode
LOA	lower-order aberrations
LRT	laser ray-tracing
MCAO	multiconjugate adaptive optics
MEMS	micro-electro-mechanical system

OCT	optical coherence tomography
PSF	point spread function
PWS	pyramid wavefront sensor
RMS	root-mean-square
SLD	superluminescent diode
TCA	transverse chromatic aberration
TEM	transverse electromagnetic

1. INTRODUCTION

1.1 Quick review of the problem

Retinal imaging is a useful tool in two main streams; ophthalmology and scientific research. In ophthalmology, high-resolution images of the retina could be used to diagnose and monitor the progress of certain diseases (such as glaucoma [1] and age-related macular degeneration (AMD) [2]), study the health of the retinal tissues, and perform oximetry measurements [3]. In research, retinal imaging is used to study cone ratios (trichromatic vision) [4], cone arrangement and dystrophy [5]; and studies to understand those images better and extract more information from raw data are being carried out [6].

Currently available adaptive optics (AO) fundus cameras are too expensive, limiting their availability to a few hospitals and universities. We argue that developing a low-cost AO fundus camera will increase the volume of basic research in this field, to help us better understand retinal pathology. We also argue that commercialising a low-cost AO fundus camera, which is affordable to optometrists, will serve as a widespread early detection tool for progressive retinal diseases; some of which which can be cured or mitigated if discovered at an early stage [6].

The reasons above indicate both a medical need and a market need for such an instrument. This study is a proof-of-concept that building such a low-cost AO fundus camera with minimum compromise on image quality could be achieved. The images should contain features as small as 1.5 μm and the adaptive optics correction should be down to the diffraction limit.

1.2 Aims of this study

The human eye, even a young healthy eye, has been demonstrated to suffer various amounts of aberrations [7]. The wavefront of light reflected off the retina deteriorates while passing through the optical media, which reduces image quality. In order to achieve high-resolution images of the retina, these aberrations should be

corrected for. AO was developed first to correct the wavefront of light in astronomy, to correct the aberrations the light suffers while propagating through the atmosphere [8], but has been adopted to correct for those aberrations in the human eye around the end of last century. AO can be used to eliminate aberrations and achieve diffraction-limited images.

The aim of this project is to design and build a high-resolution AO flood illumination retinal imaging system, capable of resolving single cones on the retina, compact, and cost-efficient as compared to commercially available systems. The idea is to prove in principle that a commercial AO fundus camera can be built for a price range affordable to optometrists, and not only to hospitals or research laboratories. We are looking to image a 4° field-of-view (FOV) on the retina with diffraction-limited performance in young healthy eyes and eyes that suffer mild high-order aberrations. We chose 4° because of the size of the isoplanatic patch in the human eye[1], measured by Dubinin and Cherezova [9].

The objectives of this study could be summarised as:

- To design a fully integrated retinal imaging system with AO, where a 4° FOV on the retina can be imaged. The system shall be able to resolve single cones on the retina.
- To build, align, and calibrate the two main arms in the system (imaging arm and wavefront sensing arm) to work simultaneously and achieve the intended high-resolution images.
- Design the software tools that will control the main components (such as the imaging scientific camera, the deformable mirror (DM), and the wavefront sensor), and create a single interface to control the whole system.
- After building the system and checking its conformation to safety standards, to try it on human subjects with normal vision, and slight to moderate aberrations, to prove that the system can achieve, in practice, the intended resolution.

To determine the success of this project, the optical system should meet the following testing criteria:

[1] Isoplanatic patch including all aberrations ($1.28° \pm 0.07°$), and excluding tip and tilt ($2.44° \pm 0.1°$), in the measurement reported in [9]

- The system model should have a diffraction limited-performance (see section 5.2).
- The system must match safety regulations (see section 5.4).
- The system should have a rigid structure, and maintain its alignment (see section 6.1).
- The system should achieve diffraction-limited performance when used with a model eye (see section 6.2).
- The system should achieve good wavefront correction ($< 0.05\ \mu m$ of residual RMS - see section 6.2).
- The system should acquire good quality retinal images of real subjects, and resolve structures larger than 1.5 μm (limited by the cut-off frequency, which equals 0.679 $cycles/\mu m$ for a 6 mm pupil. See chapter 8).

1.3 Contribution to the field

The field of high-resolution retinal imaging is continuously evolving. While the main focus of the field is to achieve higher quality *in-vivo* images to resemble those achieved in histology, the use of such expensive devices is restricted to research groups and large hospitals. This study is to investigate cost-minimisation steps with minimum compromise on image quality, as a proof-of-concept for a potentially low cost system. These steps include:

- The use of a Boston Micromachines deformable mirror, which could potentially be less expensive upon mass production.
- The use of non-coherent light sources (light-emitting diodes) for both wavefront sensing and imaging, which reduces the complexity of the system.
- The whole system is built using off-the-shelf optical components (no custom parts were ordered).

We hope that by achieving the aforementioned aims, we will introduce a widely available high-resolution fundus camera, which assists in the early detection of some retinal pathologies and help build larger sets of data for further research in the topic. Furthermore, we hope to contribute to a more positive attitude towards

cost-minimisation in this field, which would make such devices more useful to more people.

1.4 Thesis outline

Chapter 2: This chapter covers the research which has been done in the fields of retinal imaging and adaptive optics. It starts with a general review of both fields, and then goes on to discuss in detail several imaging modalities: flood illumination systems, scanning laser ophthalmoscope, optical coherence tomography. The last section discusses the latest advances in the field (at the time of writing) represented by two state-of-the-art instruments.

Chapter 3: This chapter explains the scientific foundation including a minor introduction to the layers of the human eye, the factors that affect image quality, and the theory of aberrations. The last section introduces the principles of adaptive optics, and discusses several devices which have been used as sensors and correctors in an adaptive optics instrument. Section 3.4.3 explores the mathematics and algorithms involved in controlling an adaptive optics system.

Chapter 4: This chapter explains two experiments that were carried out prior to designing the optical system, and whose results shaped the next stage in the design process.Those experiments were a simulation run to characterise the performance of the Boston Micromachines Corporation deformable mirror performance, and the investigation of light emitting diodes for both wavefront sensing and illumination of the retina.

Chapter 5: This chapter starts by discussing the various considerations that were taken into account when designing the adaptive optics assisted retinal imaging system. The following step was to optimise the optical system using Zemax, and model its performance. Section 5.3 then sets the final design parameters to be used when building the retinal imaging system. The last section then addresses the health and safety issues involved with building and using this instrument.

Chapter 6: This chapter discusses the techniques that were considered during building the instrument. Since accurate alignment is vital to achieving high resolution images, the first section discusses, in detail, the steps taken during the alignment. To verify accurate alignment has been achieved, section 6.2 introduces verification methods for different paths in the system. Matching a wavefront sensor to a wavefront corrector requires an accurate calibration method, since that affects the correction limits. This calibration method is discussed in section 6.3.

Chapter 7: This chapter discusses the software part of the retinal imaging system; the main programmes that were written to calibrate and control the adaptive optics loop, and to acquire images. The graphical user interface of those programmes are shown, in addition to a flowchart depicting the underlying algorithms. The settings of each interface are discussed in detail, to serve as a basic user manual for the retinal imaging system.

Chapter 8: This chapter contains sample images produced by the adaptive optics retinal imaging system. Since the whole project is a proof-of-concept, those images which were acquired with real human subjects show the level of detail this instrument was able to achieve, with a detailed investigation of the characteristics of the fine structure which exists in the images.

Chapter 9: This chapter concludes the thesis, and suggests a few modifications to achieve a better image quality and an easier imaging experience.

2. HISTORY OF THE FIELD

Imaging of the human retina has been a growing field of interest ever since the first fundus camera was built by Jackman and Webster in 1886 [10]. Before the end of the century, the first fairly clear image of a human retina was achieved by Gerloff using flash powder for illumination [11]. More than fifty years have passed before the electronic flash tube was invented and was implemented in fundus cameras [11]. Images taken using those fundus cameras were far from being diffraction-limited. This is due to aberrations and scattering that light suffers while passing through the ocular media as well as those of the cornea. Towards the end of the twentieth century, Liang et al. imported the field of adaptive optics (AO) from astronomy, and built the first AO fundus camera [12]. Other retinal imaging modalities were combined with AO later on to improve their performance [13, 14]. The most recent review paper to date can be found in [15].

The following sections describe the field of AO with the three main imaging modalities of the human eye, then go on to describe state-of-the-art technology in the field.

2.1 History of adaptive optics

When light passes through inhomogeneous media (e.g. atmosphere, ocular media), aberrations are introduced to the light's wavefront. The idea of AO was first introduced to correct these aberrations in real time, to give a better resolution of the sky to ground-based telescopes. This idea was proposed by Babcock in 1953 [16], and it took twenty-four more years for the technology to catch up, making it possible for the first implementation of an AO system, correcting at a 1 kHz rate [17]. Real-time AO correction was first imported into vision science in 1989 [18], but it was only used to correct for lower-order aberrations (LOA) at that time.

In 1997, Liang et al. published the first paper demonstrating the use of AO to achieve high transverse resolution retinal images [12]. They used a 37-actuator

Xinetics DM, and produced 1° field images showing the cone mosaic with clear cones in it. They also demonstrated that correcting higher-order aberrations (HOA) as well as LOA could provide subjects with supernormal vision. HOA in the human eye are dynamic, and they change at the rate of $\sim 70\ Hz$ [19]. The system demonstrated by Liang et al. did not track these changes [20].

In 2001, Fernández et al. [21] prototyped a closed-loop AO device to measure the dynamic changes in HOA of the human eye at 25 Hz, and correct for them at a 5 Hz rate. They used a 37-actuator OKO DM, and achieved a residual RMS of 0.1 μm for a 4.3 mm pupil diameter. After that, the use of AO extended to cover a wide base of ocular-related applications including psychophysical experiments and different imaging modalities, which will be discussed later in this chapter.

An adaptive optics system consists of three main parts; a sensor, a corrector, and a controller[1]. Different types of sensors have been demonstrated, with the Shack-Hartmann dominating the field since it had proven beneficial in wavefront measurements in astronomical applications. Most commercially available aberrometers for vision science still use a Shack-Hartmann, with the exception of "iTrace" (which uses the ray tracing method) and "Allegro Analyzer" (which uses the Tscherning method) [22]. Other types of aberrometers were built in-house by other groups. Navarro et al. reported a laser ray tracing method to measure the aberrations of the eye for five different field angles [23]. It gave consistent results with other studies of the off-axis aberrations of the eye [24]. The use of a pyramid wavefront sensor was demonstrated by Iglesias et al. [25] in 2002. Four years later, Chamot et al. [26] used a pyramid sensor with closed-loop operation. The system allowed a 55 Hz operation rate, and achieved a residual RMS of $\lambda/5$ over a 6 mm pupil diameter.

Two main types of correctors have been demonstrated and implemented in vision science; DMs and liquid crystal spatial light modulators (LC-SLMs). A DM is a mirror whose surface is continuous or a segmented reflective layer, which can be changed to correct the wavefront by phase conjugation. Currently available DMs are classified into six main types (segmented mirrors: see Figure 2.1, continuous membrane mirrors: see Figure 2.2). DMs are characterised mainly by their stroke and number of actuators. In general, higher stroke means more correction capability and more actuators means more spatial resolution. However, different types of DMs render the correction in a different manner, thus exhibiting some

[1] This is an overview of the work done in the field. A more complete discussion of the methods used in adaptive optics is found in 3.4.

Fig. 2.1: Segmented deformable mirrors: (a) piston only and (b) piston, tip and tilt. [20]

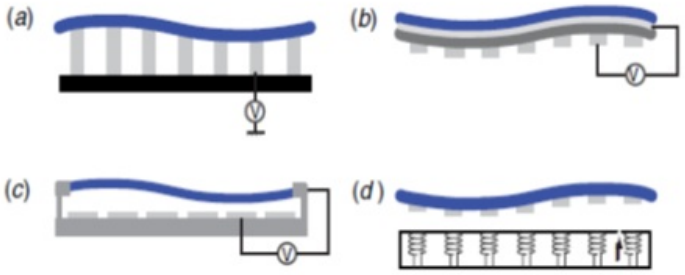

Fig. 2.2: Types of continuous membrane mirrors: (a) mirror actuated by actuators that expand or contract (b) bimorph mirror (c) membrane mirror, and (d) magnetic deformable mirror. [20]

advantages and trade-offs. Several groups worked on characterising and setting the requirements for different types of DMs [27, 28].

A liquid crystal spatial light modulator is a cheaper alternative since it is built using the currently available LCD technology. It corrects the wavefront in one of two methods. In the first method, an intensity map is imaged onto the LC device to optically correct the wavefront [29]. In the second method, electrodes are used to apply voltages to nematic liquid crystals, causing the liquid crystal molecules to change their alignment, which in turn changes the refractive index and alters the phase of the light consequently. Liquid crystal devices have more flexibility regarding the number of pixels (corresponding to the number of actuators in a DM) and stroke [20]. On the other hand, liquid crystals can only deal with linearly-polarised light. Even using a linearly-polarised light source, light reflected off the retina is depolarised; thus, using an LC-SLM would drop the intensity passing through the rest of the setup. This might be considered a drawback for using LC-SLMs since there are safety limitations to the intensity of light that can be shone into the eye. Despite their limitations, LC-SLMs have been shown to produce good correction results [30, 31]. The LC-SLM was used as a corrector in a binocular visual simulator for psychophysical studies on human eyes.

The controller in AO normally refers to a computer that analyses the measured wavefront, calculates the influence function, then sends it to the corrector.

That is convenient for the case of AO in vision science, while that might be too slow in some astronomical applications. A field programmable gate array (FPGA) has been suggested as a dedicated processing unit that would be a cheap alternative, capable of processing in the kHz regime required for the quickly varying aberrations of the atmosphere [32].

Adaptive optics has been used for many applications in vision science (e.g. psychophysics, imaging), but we include a detailed review of three main imaging modalities next; the fundus camera, the scanning laser ophthalmoscope, and optical coherence tomography.

2.1.1 Flood illumination fundus camera

The first reported *in-vivo* image of the human retina was reported by Jackman and Webster in 1886 [10]; however, the modern fundus cameras trace back to the direct ophthalmoscope model suggested by Helmholtz in 1851 [11]. The first high quality images were produced by the end of the nineteenth century [11]. The developments during the twentieth century were mainly improvements on the illumination process (e.g. introducing the electronic flash tube), commercialisation, and image processing.

It was not until 1997 that the first images were obtained using an AO fundus camera. Liang et al. reported images where single photoreceptors were resolved (see Figure 2.3). The main differences between fundus cameras since then could be summarised as changes in the wavefront sensor, the corrector, the control algorithm, and the illumination source. These design variations are mainly due to the different applications these fundus cameras are designed for.

In 1999, Roorda and Willams published a paper where they used multiple wavelength sources to image the S, M, and L cones on the retina [33]. An application of this scheme was the study of their different arrangements and their effects on colour rendering in the eye, which led to colour-blindness therapy reported in [34]. During the same year, Shin et al. designed a software package to process retinal images and quantify drusen to help diagnose AMD and its progress (see Figure 2.4) [35]. More studies have been done to automatically diagnose and quantify the progress of glaucoma (see Figure 2.5) [36] and diabetic retinopathy [37].

Up to the date of this study, the only AO fundus camera that is commercially available is the Imagine Eyes $rtx1$, which does not have a CE mark or FDA approval yet, and sold for research purposes for about €150,000 [38]. It uses a

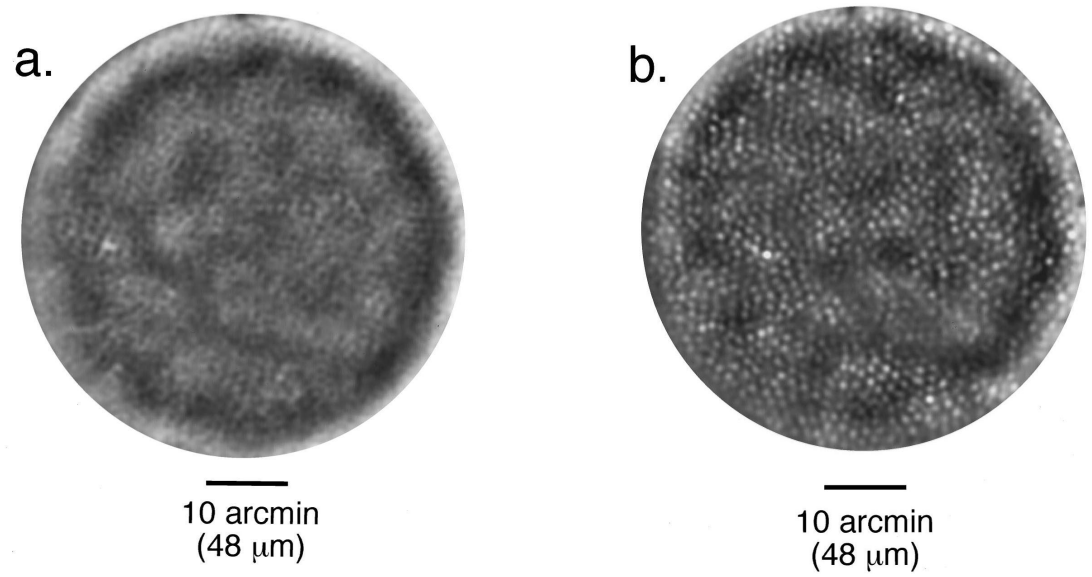

Fig. 2.3: Image of the retina at 4° eccentricity for subject DM (a) without adaptive compensation, and (b) with adaptive compensation. Each image subtends $\sim 1°$ or 291 μm at the retina. [12]

mirao™ 52-e DM developed by their sister company, Imagine Optics.

2.1.2 Scanning laser ophthalmoscope (SLO)

While a fundus camera focuses on a single plane on the retina, an SLO has the ability of axial sectioning to produce an in-focus image of multiple layers of the retina due to having a more complex design. The first AOSLO was reported by Roorda et al. [13] in 2002, which operated in an open-loop scheme. They reported two advantages for the AOSLO back then. First, an SLO can operate in real-time (at a 30 Hz frame rate), and that allows us to monitor blood flow in the retinal capillaries. Second, AO correction in an SLO increases both transverse resolution and axial resolution. In 2003, Diaz-Santana et al. [39] presented an ocular AO system which could operate in a closed-loop scheme, correcting at a bandwidth of $10 - 12$ Hz.

In 2006, Grieve et al. [40] demonstrated the use of multiple wavelengths in an AOSLO. They used sources at 532 nm, 658 nm, and 840 nm. This configuration has been shown earlier [41] to improve the visibility of different features on the retina (e.g. nerve fibre layer, blood vessels, choroid). Several implementation difficulties were reported due to the multi-wavelength configuration such as different focal points and different magnifications. During the same year, Hammer et

Fig. 2.4: An example of a drusen automatically located by a computer algorithm. [35].

Fig. 2.5: An example of glaucoma diagnosis done by calculating the cup-to-disc ratio. [36].

al. [42] reported an AOSLO with eye tracking. The system tracked and corrected for eye movements at a 1 kHz rate, $10-15$ μm accuracy. This correction alongside AO correction got the system's residual RMS down to < 0.1 μm. An alternative method for tracking was demonstrated a year later by Burns et al. [43].

Merino et al. [44] demonstrated an adaptive optics system which allowed for simultaneous *en face* optical coherence tomography and scanning laser ophthalmoscopy. They reported closed-loop operation which increased the signal-to-noise ratio in OCT by up to 6 dB and in SLO by up to 9 dB, and an improvement of lateral resolution to 5 μm.

In 2007, Chen et al. demonstrated the advantage of using two DMs in an SLO [45]. They used a bimorph AOptix DM (35 actuators, 18 μm stroke) and a MEMS BMC[2] DM (140 actuators, 1.5 μm stroke) in a woofer-tweeter arrangement, both conjugate to the pupil plane. They reported an increase of Strehl ratio from 0.02 without correction, to 0.55 using the first DM, and 0.89 using both DMs at the same wavelength.

In 2011, Dubra and Sulai [46] developed a state-of-the-art scanning ophthalmoscope, which is described in more detail in section 2.1.4.

[2] MEMS: micro-electro-mechanical system. BMC: Boston Micromachines Corporation

2.1.3 Optical coherence tomography (OCT)

OCT is an imaging technique based on a Michelson interferometer. It uses a broadband low-coherence source, and achieves high axial resolution because it records the interference pattern. Axial resolution of an OCT depends on the bandwidth of the source, while transverse resolution depends on the AO system performance (unlike SLO where both depend on the AO performance) [20]. The first AO-OCT was reported by Miller et al. in 2003 [14]. They operated their OCT in time-domain model, and achieved a high transverse resolution ($3-5\ \mu m$). In 2004, Hermann et al. [47] demonstrated an AO-OCT with an axial resolution of $3\ \mu m$; however, it was more sensitive to eye movements. The first Fourier domain AO-OCT was demonstrated in 2005 [48], where images of the inner and outer segments of the photoreceptors could be achieved.

Since the OCT uses a broadband source, chromatic aberrations become significant. To solve this problem, Fernndez et al. [49] illustrated the successful implementation of an achromatising lens in OCTs and SLOs in the near infrared. An ultra-broadband source, two deformable mirrors scheme, and an achromatising lens were all used to build an ultra-high volumetric resolution ($3.5\times3.5\times3.5\ \mu m^3$) AO-OCT system in 2008 [50].

2.1.4 State-of-the-art technology

Two systems will be briefly described as they were state-of-the-art technology around the time of this study. The first one is a dual-conjugate AO fundus camera for wide-field imaging demonstrated by Thaung et al. in 2009 [51]. The second is a very high resolution scanning ophthalmoscope capable of resolving rods near the fovea demonstrated by Dubra and Sulai in 2011 [46].

Multiconjugate adaptive optics technique has been used in telescopes to increase the isoplanatic patch, and correct the wavefront over a wider viewing angle [52]. To achieve wide-field high resolution images of the retina, Thaung et al. [51] built a system where two DMs were conjugated to the pupil plane and a plane in front of the retina (see Figure 2.6). Using five guide stars (GS) on retina (see Figure 2.7), the isoplanatic patch, and hence the AO corrected region, was increased to $6.7^\circ \times 6.7^\circ$.

Dubra and Sulai [46] reported a broadband adaptive optics scanning ophthalmoscope (BAOSO) which can achieve diffraction-limited performance over a 3 dioptre vergence range. Afocal telescopes formed of non-planar spherical mirrors

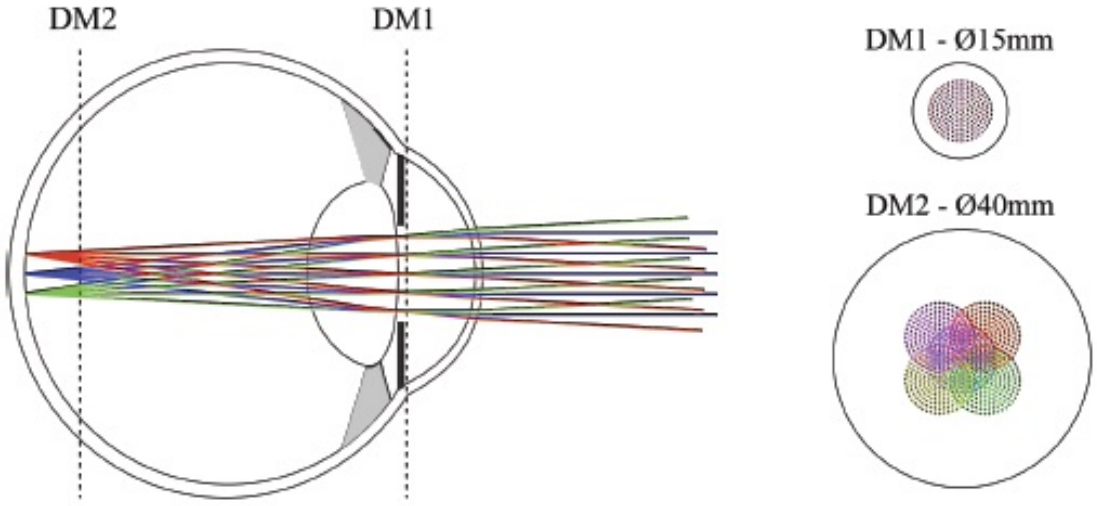

Fig. 2.6: Side view of GS light paths through the optics of the eye (left). Also shown are the GS footprints on DM1 (top right) and DM2 (bottom right). [51]

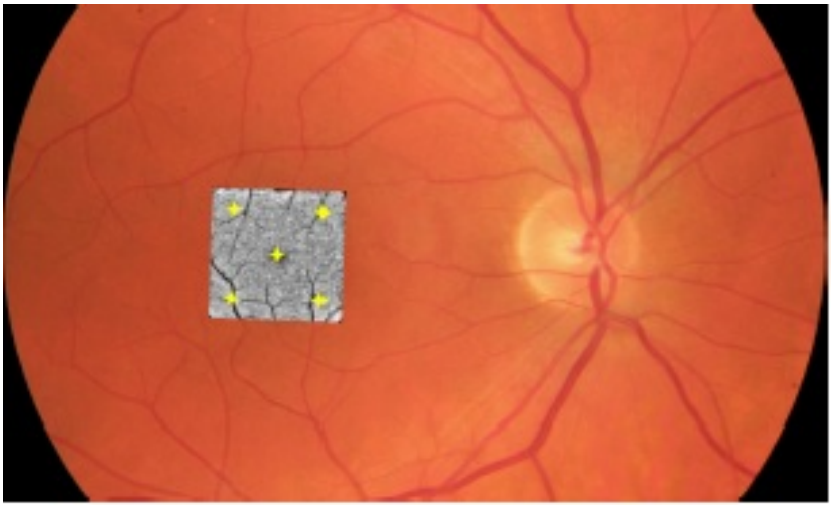

Fig. 2.7: Fundus photograph with an inset of the actual FOV and GS positions. Retinal center-to-center separation of peripheral GS from central GS is 3.1° (880 μm). [51]

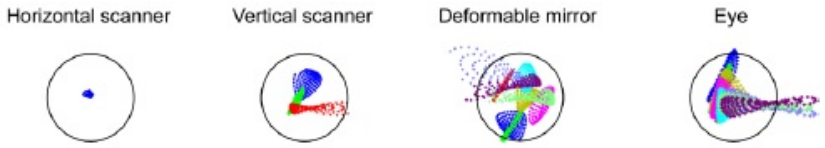

Fig. 2.8: Spot diagrams for all 4 pupil planes of the BAOSO for 450 nm wavelength over a 1.5° FOV, assuming a point source at the pupil plane in front of the Shack-Hartman wavefront sensor telescope. The black circles represent the Airy disk. [46]

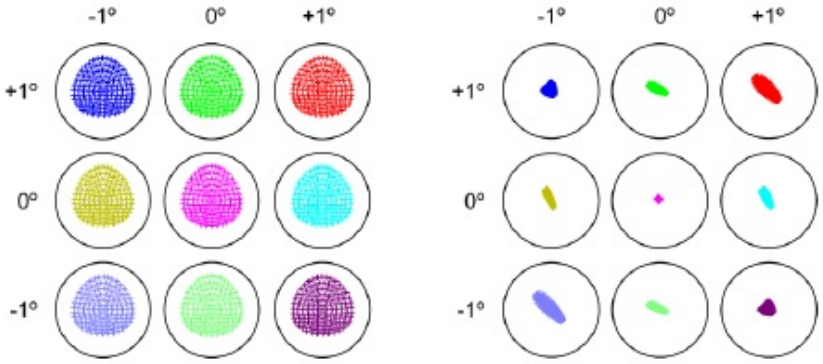

Fig. 2.9: Spot diagrams corresponding to the image plane of a 1:1 off-axis reflective afocal telescope that consists of two spherical mirrors with 800 mm radii of curvature in a planar configuration (left) and orthogonal configuration (right). The black circles correspond to the first minimum of the Airy disk. [46]

were used to reduce image and pupil plane astigmatism simultaneously. Zemax modelling was used to optimise system performance at every pupil plane (see Figure 2.8), and a pinhole smaller in size than the Airy disc was used. These considerations led to a narrower geometrical spot size below the diffraction limit (see Figure 2.9), producing yet better results. They reported diffraction-limited performance in the $450 - 850$ nm wavelength range, allowing for simultaneous imaging of different layers of the retina.

3. THEORETICAL BACKGROUND

This chapter explores in detail the theoretical basis for the work done. It starts by discussing the factors that affect image quality in human eyes, with an emphasis on the domain where adaptive optics proves advantageous. The next section has a brief anatomical view of the retina in which the reflectivity of different layers of the retina to light is discussed. Section 3.3 explains different types of aberrations seen in optical systems, and their characteristics in human eyes. The last section explains the science involved in adaptive optics correction for the eye, discussing different wavefront sensors, correctors, and control algorithms.

3.1 Factors affecting image quality

Retinal image quality is affected by diffraction, scattering, and aberrations. Diffraction is a consequence of the wave nature of light. When light waves go through an obstruction (the pupil in the case of human eyes), a diffraction pattern is introduced. This phenomenon imposes a theoretical limit on image quality, known as the diffraction limit. Due to diffraction, the ideal point spread function (PSF)[1] is an Airy disc whose radius is inversely proportional to the pupil size (see Figure 3.1) [53].

In reality, even young healthy eyes suffer various amounts of scattering and aberrations. Scattering occurs at every discontinuity that light rays pass through (e.g. cornea, lens), and light is even backscattered from the retina. This might affect our vision by introducing glare; however, unless high amounts of scattering exists (e.g. where cataracts exist), retinal image quality should not be deteriorated.

More focus is given to aberrations due to their relevance to our study. Chromatic and monochromatic aberrations exist in the eye. Longitudinal chromatic aberration (LCA) is the difference in effective focal length of the eye as a function of wavelength; where a plane wave of shorter (or longer) wavelength would

[1] Point spread function: the image of a point source after its light passes through an optical system.

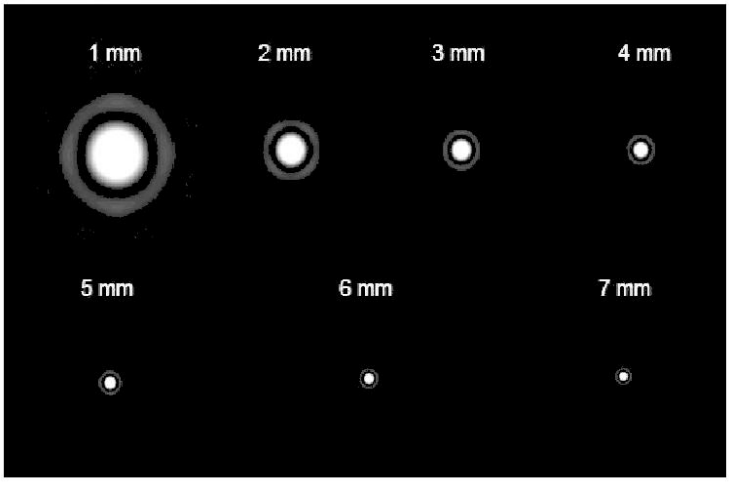

Fig. 3.1: The size of the point spread function is inversely proportional to the pupil size. A natural logarithm scale was used to increase the visibility of the diffraction rings. [54]

focus in front of (or behind) the photoreceptors layer in an emmetropic eye with a relaxed lens. Transverse chromatic aberrations (TCA) are of two types; those due to the chromatic difference of magnification [55], and those due to the chromatic difference of position [56]. Both chromatic aberration types (longitudinal and transverse) are caused by the wavelength dependence of the optical media refractive indices. Several groups have studied the effects of chromatic aberrations on retinal imaging [49, 57], and achromatising lenses have been used to correct LCA.

Monochromatic aberrations consist of lower order aberrations (LOA) and higher order aberrations (HOA). LOA (e.g. defocus, astigmatism) have been corrected for using spectacles for centuries. HOA (e.g. coma, trefoil) are less significant due to their lower magnitudes in young eyes. HOA become more significant when trying to image the retina with fine resolution, as they blur the image. HOA have been corrected for using AO (more details in sections 3.3, 3.4).

3.2 Reflective layers of the retina

Several groups studied the reflection and absorption of different layers of the retina [58–61]. It was shown that shorter wavelengths have higher reflectance from the photoreceptor layer, while longer wavelengths have higher reflectance

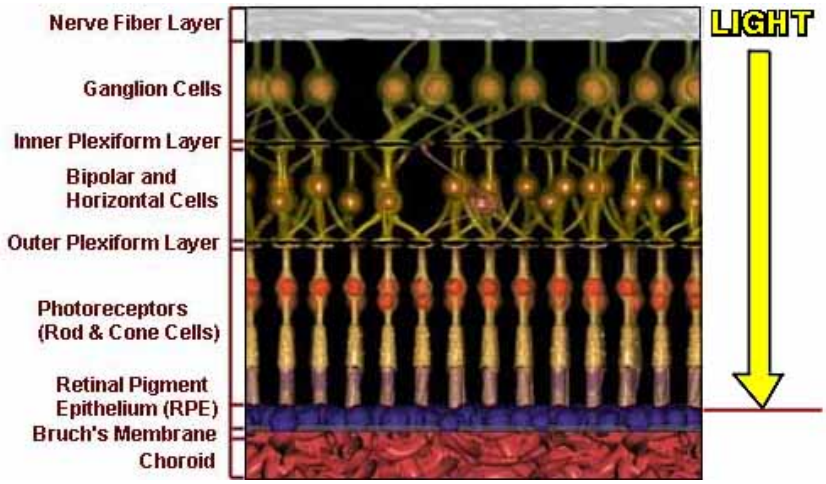

Fig. 3.2: Layers of a human retina. Shorter wavelengths have been shown to reflect off the photoreceptor layer while longer wavelengths have been shown to reflect off the choroid. [62]

from the choroid (see Figure 3.2) [59]. Since the lens of the eye suffers some chromatic aberrations, longer wavelengths are focused at a deeper layer of the retina of an emmetropic eye. In our case, since we are using infrared light for the probe beam and green light for illumination, a special correction factor should be calculated to correct for different reflective layers and chromatic aberrations throughout the system. A detailed modelling of layers reflectivities can be found in [59].

Another important result discussed in these experiments was the low reflectivity of the retina ($< 10\%$) compared to that of the cornea ($\sim 80\%$) [59]; thus, corneal reflections should be extinguished so that they would not obscure the retinal image.

Both concerns raise design challenges, and are discussed further in chapter 5.

3.3 Aberrations

Aberrations are departures of the performance of an optical system from the predictions of paraxial optics. If not compensated for correctly, aberrations decrease the image quality of an optical system. Aberrations are mainly divided into monochromatic and chromatic aberrations, which are discussed in detail as follows.

3.3.1 Monochromatic aberrations

Monochromatic light passing through optical media could suffer deviations from the paraxial approximation [53] due to:

- Third order term in the series expansion of $\sin\theta$ approximation, or Seidel aberrations.
- Localised optical path differences caused by inhomogeneities in the optical media cause variable amounts of retardation to different parts of the wavefront, or monochromatic wavefront aberrations.

Seidel aberrations

The Taylor expansion of $\sin\theta$ is given by [54]:

$$\sin\theta = \theta - \frac{\theta^3}{3!} + \frac{\theta^5}{5!} - \frac{\theta^7}{7!} + \dots \tag{3.1}$$

where θ is defined in Figure 3.3. In the paraxial approximation, where only the first term is considered (or $\sin\theta \approx \theta$), we get the lens maker's formula [54]:

$$\frac{n_1}{s_o} + \frac{n_2}{s_i} = \frac{n_2 - n_1}{R} \tag{3.2}$$

where n_1 and n_2 are the refractive indices of media 1 and 2 respectively, and s_i, s_o, and R are defined in Figure 3.3. For rays passing further away from the optic axis of the lens (SP in Figure 3.3), or as θ increases; the third order term in the Taylor expansion becomes significant. When considered, equation 3.2 becomes [54]:

$$\frac{n_1}{s_o} + \frac{n_2}{s_i} = \frac{n_2 - n_1}{R} + h^2\left[\frac{n_1}{2s_o}\left(\frac{1}{s_o} + \frac{1}{R}\right)^2 + \frac{n_2}{2s_i}\left(\frac{1}{R} - \frac{1}{s_i}\right)^2\right] \tag{3.3}$$

This yields different types of aberrations (spherical, astigmatism, coma). For simplicity, an example of Seidel spherical aberration is shown in Figure 3.4.

Monochromatic wavefront aberrations

Wavefront aberrations are caused by the inhomogeneity of the optical media the light wave passes through. They could be mathematically modelled using a set of orthonormal modes called Zernike polynomials (more information in Appendix A).

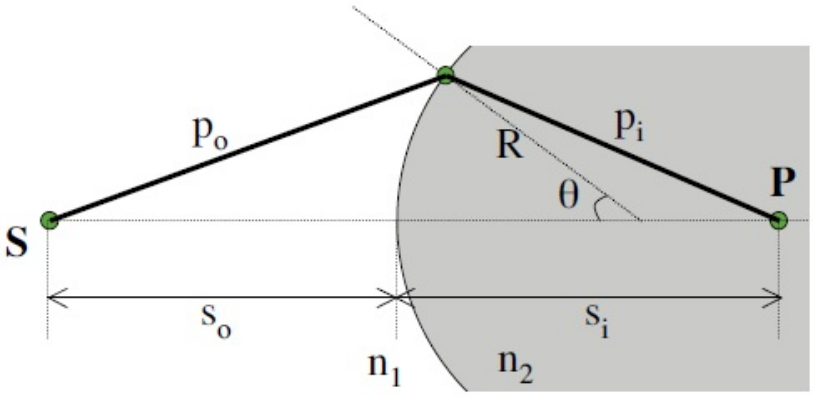

Fig. 3.3: Paraxial optics demonstration. [54]

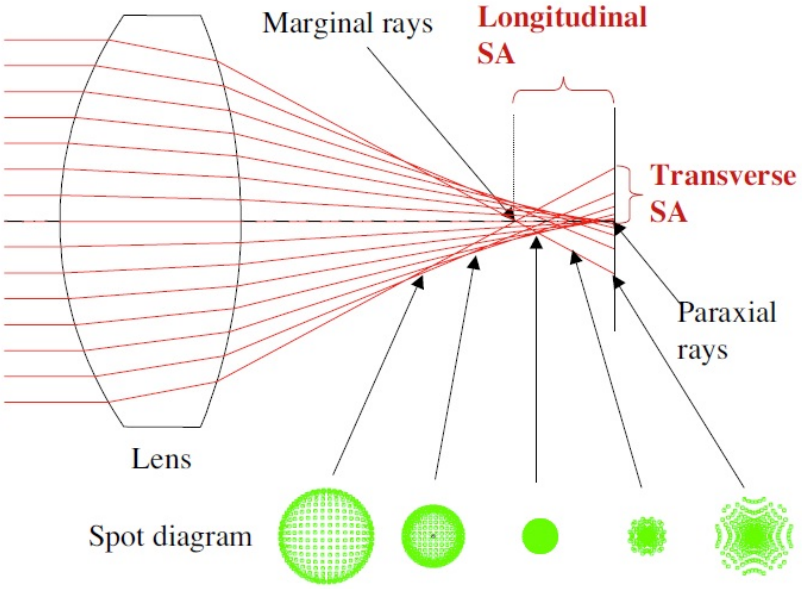

Fig. 3.4: Seidel spherical aberration. [54]

As a standard model of reporting wavefront aberrations, the phase of a wavefront passing through a circular pupil is described as the linear sum of weighted Zernike polynomials (see Figure 3.5). The spatial frequency of Zernike modes increases with their order. A wavefront phase map can be represented as a weighted summation of Zernike polynomials (in polar coordinates) as follows:

$$W(\rho,\theta) = \sum_{i=0}^{\infty} c_{nm} Z_n^m(\rho,\theta) \tag{3.4}$$

where c_{nm} is the weighting factor, and Z_n^m is the Zernike polynomial of order n and frequency m, and has the general form given by [63]:

$$Z_n^m(\rho,\theta) = \left\{ \begin{array}{ll} N_n^m R_n^{|m|}(\rho)\cos m\theta & for\ m \geq 0 \\ -N_n^m R_n^{|m|}(\rho)\sin m\theta & for\ m < 0 \end{array} \right\} \tag{3.5}$$

where N_n^m is a normalisation factor given by equation 3.7 below, and $R_n^{|m|}(\rho)$ is given by [63]:

$$R_n^{|m|}(\rho) = \sum_{s=0}^{(n-|m|)/2} \frac{(-1)^s (n-s)!}{s!\,[0.5(n+|m|-s]!\,[0.5(n-|m|-s]!} \rho^{n-2s} \tag{3.6}$$

$$N_n^m = \sqrt{\frac{2(n+1)}{1+\delta_{m0}}} \tag{3.7}$$

where $n = 0, 1, 2, ...$, and where $m = -n, -n+2, -n+4, ..., n$, and δ_{m0} is the Kronecker delta (i.e. $\delta_{m0} = 1$ for $m = 0$, $\delta_{m0} = 0$ otherwise).

Tip and tilt are considered during the alignment of the setup, but no correction for it is included later on in vision-related AO systems. In atmospheric AO systems, a tip/tilt mirror is used to correct for that in real time. Second order Zernike polynomials (typically referred to as LOA) describe defocus and astigmatism. They have been corrected for since the thirteenth (defocus) and nineteenth (astigmatism) centuries using spectacles [65]. HOA aberrations are dynamic in nature (in human eyes). They vary at a rate of up to 70 Hz [19].

In adaptive optics systems, a wavefront corrector is used to correct HOA, and sometimes LOA. To correct HOA in our instrument, a BMC deformable mirror was used (discussed further in section 3.4.2). Since LOA are static (when accommodation is medically frozen) and have higher magnitudes, a one pass correction method could be used to minimise LOA. A Badal optometer has been demon-

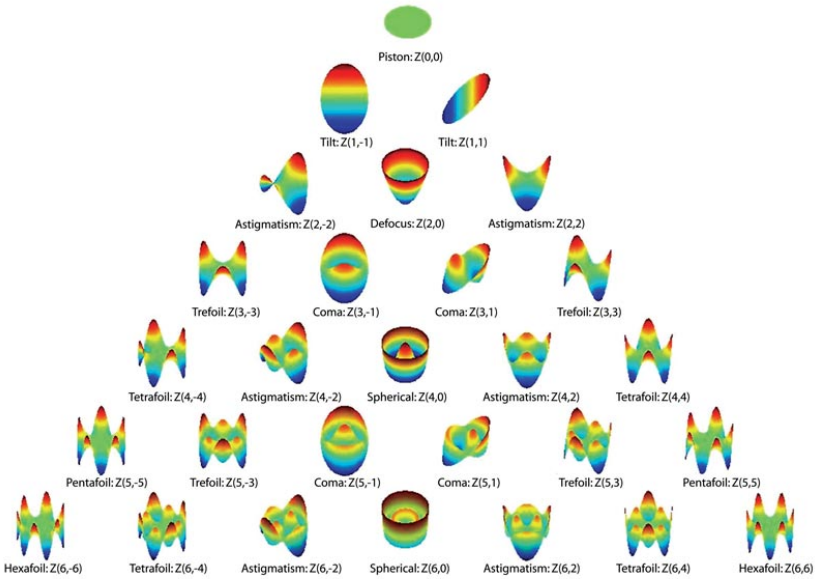

Fig. 3.5: The first twenty-eight Zernike modes. [64]

strated to reduce defocus, while solutions such as rotating cylinders and trial lenses have been demonstrated to reduce astigmatism. A diffractive Alvarez lens has been suggested to corrected all LOA in one go [66].

Three variations of the Badal optometer were studied, and their advantages and limitations were characterised by Atchison et al. [67]. The first variation was a single lens Badal system, where the target is movable, and the maximum negative vergence is theoretically limited to $-P$ (where P is the Badal lens power). To increase the vergence, a second system was proposed where an auxiliary lens was introduced. The auxiliary lens and the target moved together to increase the range of ocular vergence. The third variation only moves the auxiliary lens relative to the Badal lens' position, and uses a distant target (see Figure 3.6). This variation allows for larger targets. In this variation, ocular vergence (Q) and the angular magnification at the eye (M) are given by:

$$Q = -P - P^2(1 - dP_a)/P_a \tag{3.8}$$

$$M = -P/P_a \tag{3.9}$$

where P is the Badal lens equivalent power, P_a is the auxiliary lens equivalent power, and d is the distance between the two lenses.

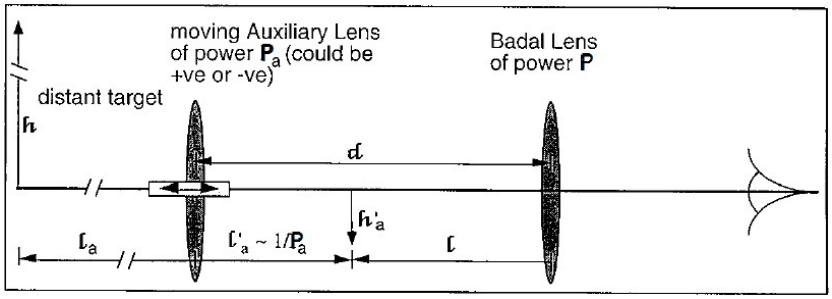

Fig. 3.6: Schematics of a two lens Badal optometer proposed by Atchison el al. to correct for ocular vergence (modified). [67]

3.3.2 Chromatic aberrations

The refractive index of a medium is defined as the ratio between the speed of light in vacuum and the speed of light in that medium. Different wavelengths of light pass through media at different speeds; therefore, the refractive index is a function of wavelength and is given by [68]:

$$n^2(\lambda) = a_0 + a_1\lambda^2 + a_2\lambda^{-2} + a_3\lambda^{-4} + a_4\lambda^{-6} + a_5\lambda^{-8} \tag{3.10}$$

Since the angle of refraction of a light ray is given by Snell's law:

$$n_0 \ \sin\theta_i = n_1(\lambda)\sin\theta_r \tag{3.11}$$

where θ_i is the angle of incidence, θ_r is the angle of refraction, and assuming the first medium to be air with refractive index n_0; then n_1 being a function of wavelength will cause different angles of refraction depending on the wavelength. This dispersion causes the focal length of a lens to be a function of wavelength, too; and the distance between the first and last focal points is referred to as longitudinal chromatic aberration (LCA, see Figure 3.7(a)). In addition, an off-axis beam will suffer from transverse chromatic aberrations (TCA, see Figure 3.7(b)).

This is a simplified picture of chromatic aberrations in the eye. In fact, modelling chromatic aberrations in the eye is a more complex task, since the lens of the human eye was shown to have a gradient refractive index (GRIN lens). Not only is the refractive index a function of wavelength, but also a function of position. Several groups used empirical data to simulate the GRIN lens of the eye. The refractive index as a function of position is given by [68]:

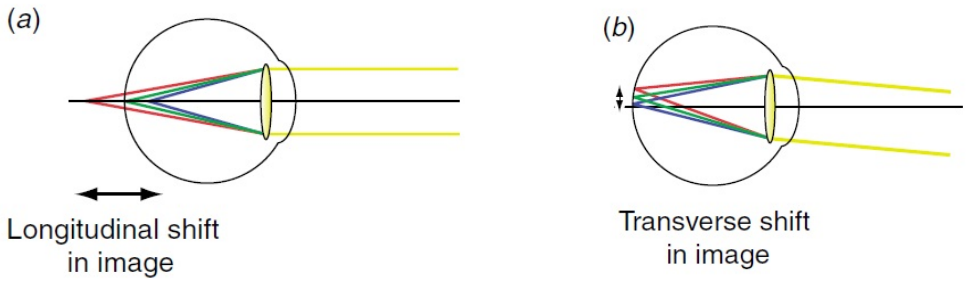

Fig. 3.7: Longitudinal (a) and transverse (b) chromatic aberrations (exaggerated) in the human eye. [69]

$$n_{ref} = n_0 + n_{r2}r^2 + n_{r4}r^4 + n_{z1}z + n_{z2}z^2 + n_{z3}z^3 + n_{z4}z^4 \quad where \quad r = (x^2 + y^2)^{1/2} \tag{3.12}$$

The values of those coefficients are found by fitting experimental data. The most recent wide-field eye model to date is explained in Goncharov and Dainty [70], where the topic is explored in more detail.

Chromatic aberrations could be minimised in an optical setup using achromatic doublets and apochromatic lenses (see Figures 3.8, 3.9), the latter used to obtain high quality coloured images such as in a microscope objective. Chromatic aberrations in the eye have been corrected for using an achromatising lens (further explained in [57]).

3.4 Principles of adaptive optics

An adaptive optics system has three main components: a wavefront sensor, a wavefront corrector, and a computer to control the adaptive optics loop. Figure 3.10 shows a general AO system to correct for the eye aberrations, which could be combined with an imaging modality or a psychophysics experiment. This section discusses several different methods that have been used in the field, with an emphasis on the methods used in our setup. A more complete review can be found in [72].

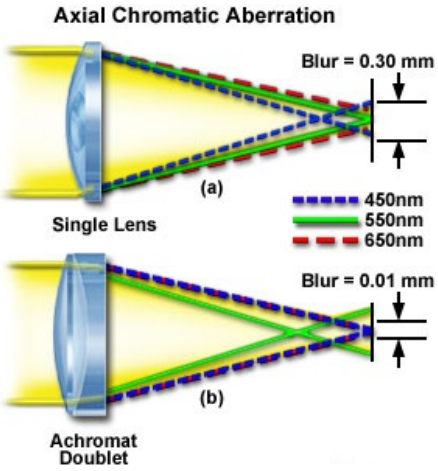

Fig. 3.8: Minimising chromatic aberrations using an achromatic doublet. [71]

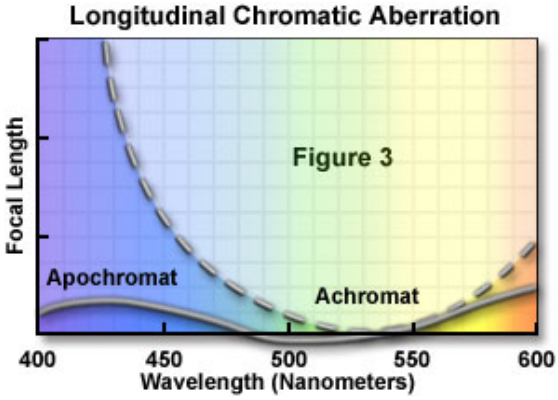

Fig. 3.9: Comparison between achromatic and apochromatic lenses in terms of longitudinal chromatic aberrations. [71]

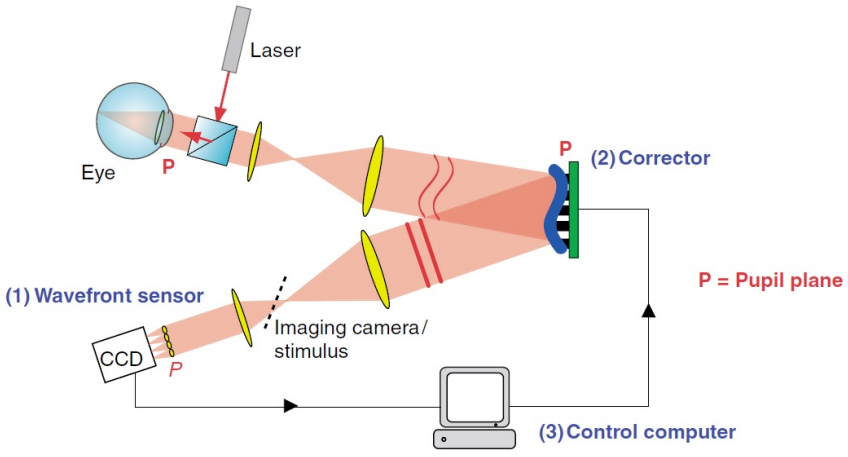

Fig. 3.10: General AO system showing how the three main components; the sensor, corrector and controller, are coupled together. "Imaging camera/stimulus" marks the position where the science arm is integrated. [20]

3.4.1 Wavefront sensor

Three types of wavefront sensors that are used in the field are compared here; the ray-tracing technique, the pyramid wavefront sensor, and the Shack-Hartmann wavefront sensor (SHWS).

Ray-tracing technique

The laser ray-tracing (LRT)[2] technique was proposed by Navarro and Losada [74]. It works by shining one ray at a time, at different positions in the pupil plane, and tracing it in the imaging plane; therefore tracing the path the ray took within the aberrated medium. Sampling the full pupil one ray at a time makes it possible to reconstruct a phase map of the full pupil. A main advantage of ray-tracing is the flexibility of sampling, where the beams could be directed in any geometry to sample the pupil during the experiment (as opposed to the fixed lenslet array in a SHWS). On the other hand, since the matching occurs between one ray in the pupil plane and the position it arrives at in the image plane, ray-tracing should be performed one ray at a time. Thus, the wavefront sensing process is slow, and simultaneous measurement of phase for the whole pupil is not possible. Navarro and Moreno-Barriuso [73] compared the reconstructed PSF using an LRT measurement and a SHWS to the PSF directly recorded on a CCD camera (see Figure 3.11). The comparison showed good agreement in results between the two methods.

Pyramid wavefront sensor

The pyramid wavefront sensor (PWS) was first proposed for use in astronomy in 1996 [75], and was later adapted for use in vision applications in 2002 [25]. A four-faceted glass pyramid is positioned in the Fourier plane of the aberrated wave (see Figure 3.12). This forms four images of the pupil at the detector level, each representing a Foucault knife-edge test [76] blocking three quarters of the pupil plane. The relative point-to-point intensity of the four images allows for the local tilt to be computed (see equation 3.13). The wavefront is then reconstructed from the local tilts (further explained with the SHWS below). In the case of a plane wavefront (aberration-free wavefront), the four images are identical. The

[2] It was originally referred to as "shining light pencils into the eye". The term "laser ray-tracing" was coined in a later paper [73].

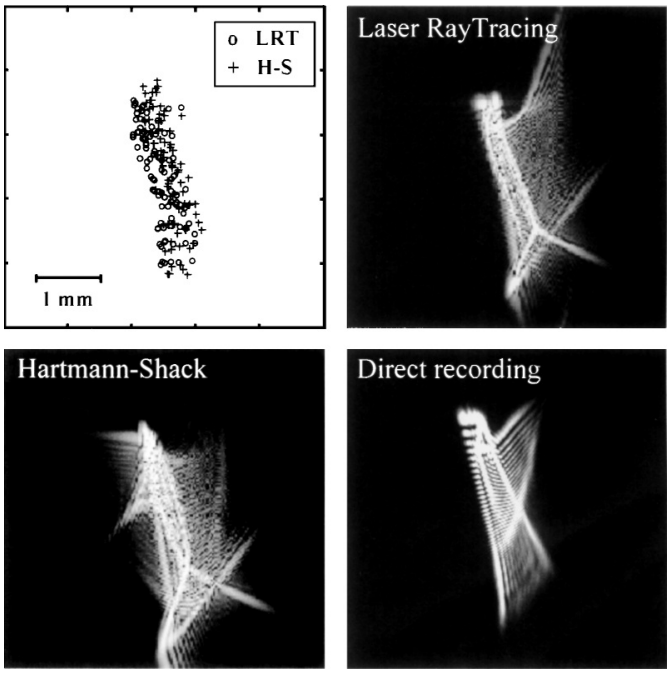

Fig. 3.11: Top left, spot diagrams (raw experimental data or geometric aberrations); top right, bottom left, PSF's computed from wave aberration data; and bottom right, PSF recorded directly on the CCD. [73]

coordinates in the Fourier plane due to a single point (x, y) in the pupil plane are given by [75]:

$$(X, Y) = f(\frac{\partial W}{\partial x}, \frac{\partial W}{\partial y}) = f \stackrel{\rightarrow}{\nabla} W \tag{3.13}$$

where f is the focal length of the focusing lens, and W is the wave aberration function for the exit pupil coordinates (x, y). This system could be used to predict the sign of the phase derivative, but not its amplitude; since an aberrated beam would pass through only one quadrant of the pyramid [75, 77]. To solve this problem, the system could be modulated by transversely oscillating the pyramid [75], or by rotating the beam using a tip/tilt mirror (which is the case considered in equation 3.15) [78]. A ratio between intensities in the x and y directions, which could be used to reconstruct the wavefront, is given by [78]:

$$\begin{aligned} S_x(x, y) &= \frac{(I_2(x, y) + I_4(x, y)) - (I_1(x, y) + I_3(x, y))}{\sum_{i=1}^{4} I_i(x, y)} \\ S_y(x, y) &= \frac{(I_1(x, y) + I_2(x, y)) - (I_3(x, y) + I_4(x, y))}{\sum_{i=1}^{4} I_i(x, y)} \end{aligned} \tag{3.14}$$

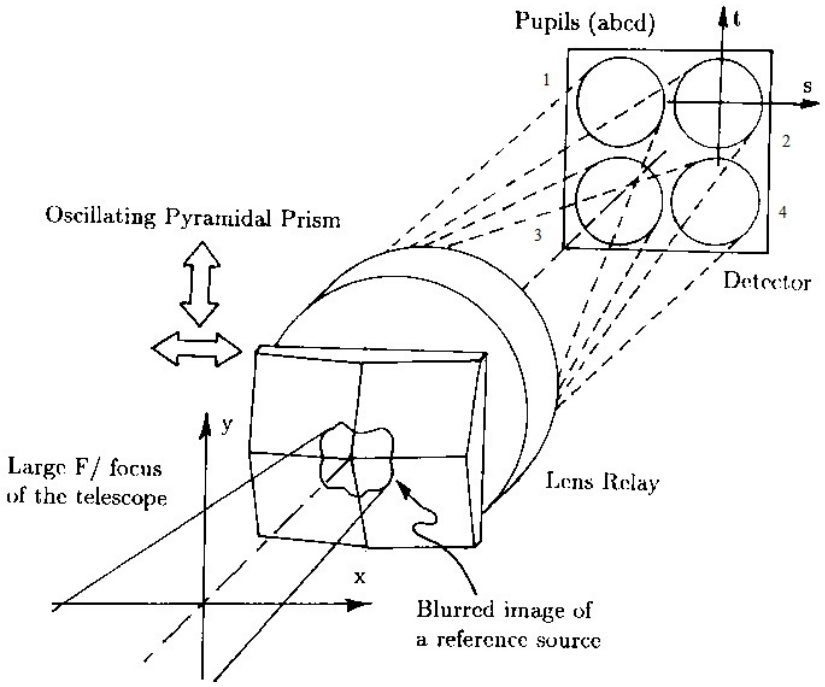

Fig. 3.12: General layout of a pyramid wavefront sensor (modified). [75]

where $I_i(x, y)$ is the intensity at point (x, y) in the i^{th} pupil image (as defined in Figure 3.12). The local wavefront slopes, in the geometrical optics regime, are then given by [78]:

$$\begin{aligned} \frac{\partial W(x,y)}{\partial x} &= \frac{R}{f} \sin \frac{\pi}{2} S_x(x,y) \approx \frac{R}{f} \left(\frac{\pi}{2} S_x(x,y) \right) \\ \frac{\partial W(x,y)}{\partial y} &= \frac{R}{f} \sin \frac{\pi}{2} S_y(x,y) \approx \frac{R}{f} \left(\frac{\pi}{2} S_y(x,y) \right) \end{aligned} \tag{3.15}$$

where R is the radius of dynamic modulation at the pyramid vertex, f is the focal length of the lens before the pyramid, and S_x, S_y are assumed to be small.

The main advantage of the pyramid wavefront sensor is its variable sensitivity, which is changed by varying the modulation amplitude. Another advantage of the PWS over a SHWS is the large dynamic range; however, it has been shown recently that a SHWS's sensitivity could be manipulated to extend the dynamic range [79]. The main disadvantage of the PWS is the need for modulation, which translates into a dynamic object within the wavefront sensing system [77].

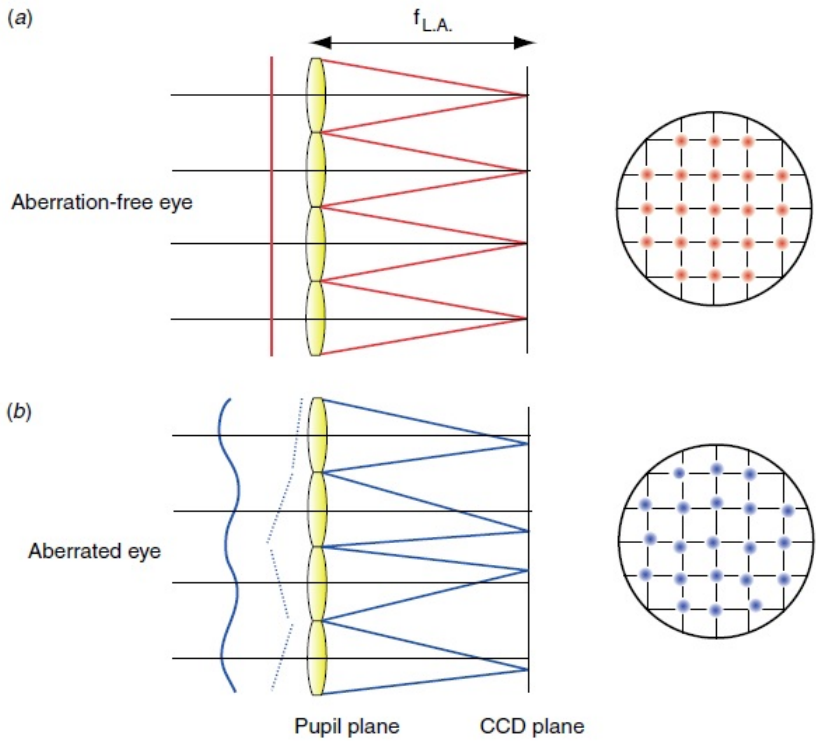

Fig. 3.13: Principle of a Shack-Hartmann wavefront sensor. A lenslet array is placed at a pupil conjugate plane, where the wavefront slope is measured in smaller subapertures. *(a)* A plane wavefront forms a uniform spots array in the CCD plane (used as reference spots). *(b)* An aberrated plane forms a non-uniform array of spots whose deviation from the reference spots is correlated to the local slopes in the pupil plane. [20]

Shack-Hartmann wavefront sensor

The Shack-Hartmann wavefront sensor (SHWS) was first adopted from astronomy to objectively measure the aberrations of the eye by Liang et al. in 1994 [80]. It reconstructs the phase map from local slopes within the pupil. Using a fixed lenslet array, the pupil plane is divided into smaller subapertures. When a plane wave passes through the lenslet array, it produces a uniform grid (used for calibration) of spots in the CCD plane, placed in the focal plane of the lenslets (see Figure 3.13a). When an aberrated wave passes through the lenslet array, the spots in the CCD plane deviate from the calibration grid (see Figure 3.13b). Geometrically, these deviations can be used to calculate the local tilts in the pupil plane (see Figure 3.14), which can then be used to reconstruct the phase map.

The local slopes in the x and y directions, assuming the deviations are small, are given by [20]:

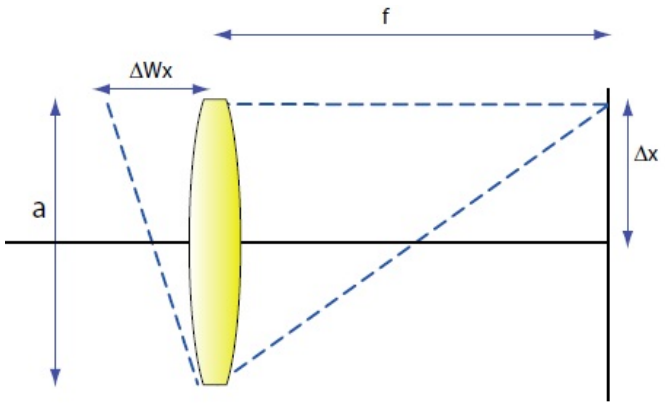

Fig. 3.14: Relationship between the local slope in the pupil plane and the spot deviation from reference spot in the CCD plane. [20]

$$\begin{aligned} \frac{\partial W}{\partial x} &\approx \frac{\Delta W_x}{a} = \frac{\Delta x}{f} \\ \frac{\partial W}{\partial y} &\approx \frac{\Delta W_y}{a} = \frac{\Delta y}{f} \end{aligned} \tag{3.16}$$

where a is the diameter of the lens, f is the focal length, and $\Delta x, \Delta y$ are the deviation from the reference spot in the x and y directions respectively.

The deviations are calculated by a computer algorithm that looks for the spot within a search-block whose size and position are the same as those of the lenslet. Since the spot can only move by $a/2$ before it escapes the search-block, the dynamic range of a SHWS is given by [20]:

$$\Delta W_{max} = \frac{\Delta x_{max}\ a}{f} = \frac{a^2}{2f} \tag{3.17}$$

and the sensitivity of the SHWS is given by [20]:

$$\Delta W_{min} = \frac{\Delta x_{min}\ a}{f} \tag{3.18}$$

where Δx_{min} depends on the resolving power of the centroiding algorithm among other system specific parameters. Thus, there is an inherent trade-off between dynamic range and sensitivity of a SHWS, which needs to be considered when choosing the lenslet array to sample the pupil.

In 2009, Leroux and Dainty [79] introduced a search algorithm that significantly increases the dynamic range of a SHWS. It starts by acquiring a raw frame

from the CCD camera of the SHWS, and uses the least square method [81] to reconstruct the LOA (tip/tilt, defocus, and astigmatism) from that. Using a linear combination of reduced Zernike polynomials for LOA:

$$Z_0 = \sum_{i=2}^{6} a_i Z_i \tag{3.19}$$

where Z_i are Zernike polynomials as defined in Appendix A, and a_i are their coefficients, a new set of reference spots is calculated using:

$$\widetilde{X} = X_{ref} + MZ_0 \tag{3.20}$$

where X_{ref} is the set of reference spot positions, and M is the interaction matrix. The coefficients a_i are optimised by the algorithm to achieve:

$$\sum_{pupil} \left(X[i] - \widetilde{X}\,[i] \right)^2 = minimum \tag{3.21}$$

where X is the set of measured spots. Then $\widetilde{X}$ is used as the new set of reference spots for the calculation of spot deviations.

When sampling the pupil plane, two more considerations need to be taken into account. First, light level in the lenslet array plane is typically very low, due to the low damage threshold of the human retina coupled with its low reflectivity. A lower number of lenslets spanning the pupil plane translates into a higher signal-to-noise ratio at the SHWS. Second, the more lenslets used to sample the pupil, the higher Zernike orders can be reconstructed; therefore, a better correction can be achieved. It was estimated that the number of Zernike poynomials which could be reconstructed from the data is equal to the number of lenslets sampling the pupil [82].

Due to scatter in the ocular media and other noise sources, the signal that reaches the CCD is not purely formed of spots. Furthermore, the spot size is of the same order of magnitude as the pixel size, hence a sub-pixel determination of the spot position is required for an accurate measurement of phase. Two methods have been used to determine the positions of the spots on the CCD; centroiding and cross-correlation.

- **Centroiding:** Consider a spot that falls within the search-block of a lenslet array. Assuming a uniform intensity profile of the spot, the sub-pixel po-

sition can be calculated using the variation of intensity between the pixels, and the centre of gravity position (c_x, c_y) of the centroid can be estimated as [72]:

$$c_x = \frac{\sum_{i,j} x_{i,j} I_{i,j}}{\sum_{i,j} I_{i,j}}$$
$$c_y = \frac{\sum_{i,j} y_{i,j} I_{i,j}}{\sum_{i,j} I_{i,j}} \tag{3.22}$$

where $I_{i,j}$ and ($x_{i,j}$, $y_{i,j}$) are the signal and the position coordinates of the CCD pixel (i, j). The accuracy of this centroiding algorithm decreases with noise and irregular spot shapes. Further improvements to reduce the effect of noise and improve the performance of centroiding algorithms have been suggested (e.g. [83]).

- **Cross-correlation:** In this method, a source of light (could be an extended source) is convolved with the reference spot positions as shown in Figure 3.15. A small square is taken as a reference cell (black square in Figure 3.16) with coordinates $r(x, y)$ in the reference signal, with Fourier transform $R(u, v)$. During wavefront sensing, a smaller square is taken from measurement (white square in Figure 3.16) with coordinates $s_i(x, y)$ and Fourier transform $S_i(u, v)$. The cross-correlation for each signal box i is then given by [84]:

$$C_i(u, v) = R^*(u, v) S_i(u, v) \tag{3.23}$$

where (*) denotes a complex conjugate. Further iterative processing is required (explored further in [84]), until the position of the spot is determined as the position with the highest correlation to the original source. This is later used to reconstruct the phase map using either a zonal or a modal approach (explored in detail in [7]).

When using coherent light as a beacon, speckle is formed due to the diffusive properties of the retina. Speckle size is affected by the sizes of the pupil and scattering objects. In this system, a low coherence light source is used for wavefront

Fig. 3.15: (a) A point source spot-image of a Shack-Hartmann sensor. (b) An example of an object scene image used to create an SH extended-scene image. (c) The SH extended-scene created by convolving (a) with (b). [84]

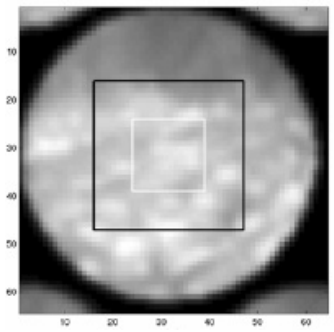

Fig. 3.16: Reference cell (black box) and signal cell (white box) as defined in the CCD plane, for cross-correlation wavefront sensing. [84]

sensing.

3.4.2 Wavefront corrector

Light is a form of electromagnetic radiation, whose electric field magnitude could be represented in the general form:

$$E = A \exp(-i\phi) \tag{3.24}$$

where A is the amplitude, and ϕ is the phase. When the light wave falls on the wavefront sensor, ϕ is measured. Correction is achieved by calculating the complex conjugate of the electric field, by introducing a phase difference of $(-\phi)$ to the wavefront. Now the phase is defined as:

$$\phi = \frac{2\pi\ OPL}{\lambda} \tag{3.25}$$

where λ is the wavelength of light, and OPL is the optical path length which is given by:

$$OPL = n.z \tag{3.26}$$

where n is the refractive index of the medium and z is the distance travelled by light wave.

It follows from Equation 3.26 that phase can be corrected either by changing the refractive index (as in liquid crystals) or the distance (as in deformable mirrors), across the wavefront. This correction was made possible when devices (discussed in the following sections) allowed for locality of phase modulation.

Liquid crystal spatial light modularors

Liquid crystal spatial light modulators (LC-SLMs) use the existing technology of nematic liquid crystals to correct the wavefront in transmission or reflection mode. Varying the voltage applied to LCs, their alignment changes causing a modulation in their refractive index, and hence the phase of the light wave passing through them. An example of an LC-SLM operating in reflection mode is shown in Figure 3.17.

Since LC-SLMs share the technology with mass production LCDs, they have a much lower cost than deformable mirrors. They typically have higher resolution ($\sim$ 1 million pixels compared to $\sim$ 100 actuators for DMs), which allows them

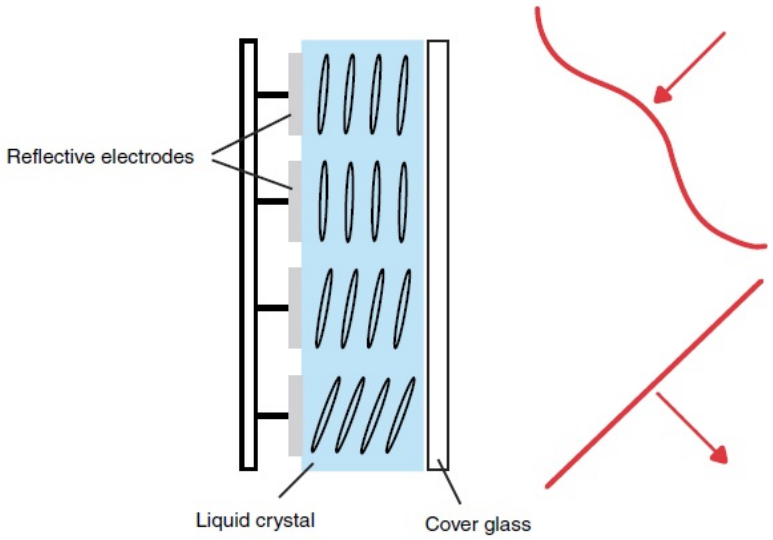

Fig. 3.17: An example of a nematic liquid crystal spatial light modulator operating in reflection mode. Voltage applied to the electrodes causes a realignment of liquid crystals, which causes a change in their refractive index, and hence changes the phase of the wavefront. [20]

to correct high frequency aberrations. They have a 2π phase correction range, although this can be expanded using phase wrapping techniques [20].

On the other hand, LC-SLMs are limited by their ability to process linearly polarised light. Even using a linearly polarised light source, the retina acts as a depolariser. The intensity of light reflected from the retina is then lowered by a factor of two. Since safety limits apply to the amount of light going into the eye, this is a drawback of using LC-SLMs. Another drawback of LC-SLMs, which is more relevant to astronomy applications is their relatively lower speed (60 Hz compared to $\sim$ 30 kHz in DMs). This has been shown sufficient to correct the slow varying aberrations of the eye.

Deformable mirrors

Different types of deformable mirrors (DMs) were discussed in section 2.1. This section describes the advantages and limitations of those types, and goes on to explain the operating principles of a MEMS DM for its relevance to this project.

The first type of DM is the segmented mirror. The mirror's surface consists of a number of independent actuators, each can move in one or three degrees of freedom (see Figure 2.1(a), (b) respectively). The main advantage of this type is that there is no coupling between actuators since there is no membrane attached

to the actuators. Their control algorithm is more straight-forward than membrane mirrors (although the continuity of the wavefront remains an issue). They can be used to correct for high frequency aberrations. However, light suffers from diffraction and other artefacts due to their discontinuity and the edges of their actuators.

Continuous membrane mirrors vary in the physical principle used to shape their membrane. One method is to use pistons just like those in the segmented mirror, attached to a membrane (see Figure 2.2(a)). This introduces a continuous phase variation, more similar to the phase map of a normal eye; however, it introduces a coupling factor between actuators and makes it harder to correct high frequency aberrations.

A second method uses more than one layer of material, bonded in a similar fashion to a thermocouple (see Figure 2.2(b)). Voltage applied to one surface causes it to expand, thus reshaping the surface of the mirror. This method is more suitable to correct lower frequency aberrations, and can have high stroke values.

A third method uses electrostatic attraction to alter the shape of an edge-clamped membrane (as shown in Figure 2.2(c)). This method has high control over the surface, and does not suffer from hysteresis. However, since the edge is typically clamped in this type of mirror, the active area is significantly smaller than the mirror's size.

A more recent method uses a magnetic field [38] to control the shape of the membrane in a DM (see Figure 2.2(d)). This allows for a very high stroke, and consequently higher correction abilities. Drawbacks to this method are stability for a fixed amount of correction and overshooting when applying a phase correction. Software fixes have been investigated to account for the latter.

Due to their different operating principles, DMs capability of correcting aberrations for different applications vary. For instance, the magnitude of correctable aberrations is directly proportional to the stroke, for the same mirror; however, the optimum correction capability depends on hysteresis, number of actuators, stability, amongst other factors. Thus, the performance of a mirror is measured for the whole ensemble, and one cannot say a mirror corrects aberrations better based on larger stroke alone. Several DMs were characterised by Devaney et al. [85], and compared according to their applicability for vision and astronomical applications. The characterisation started by investigating the optimum active area of the DMs to be used for correction, based on their geometry and influence

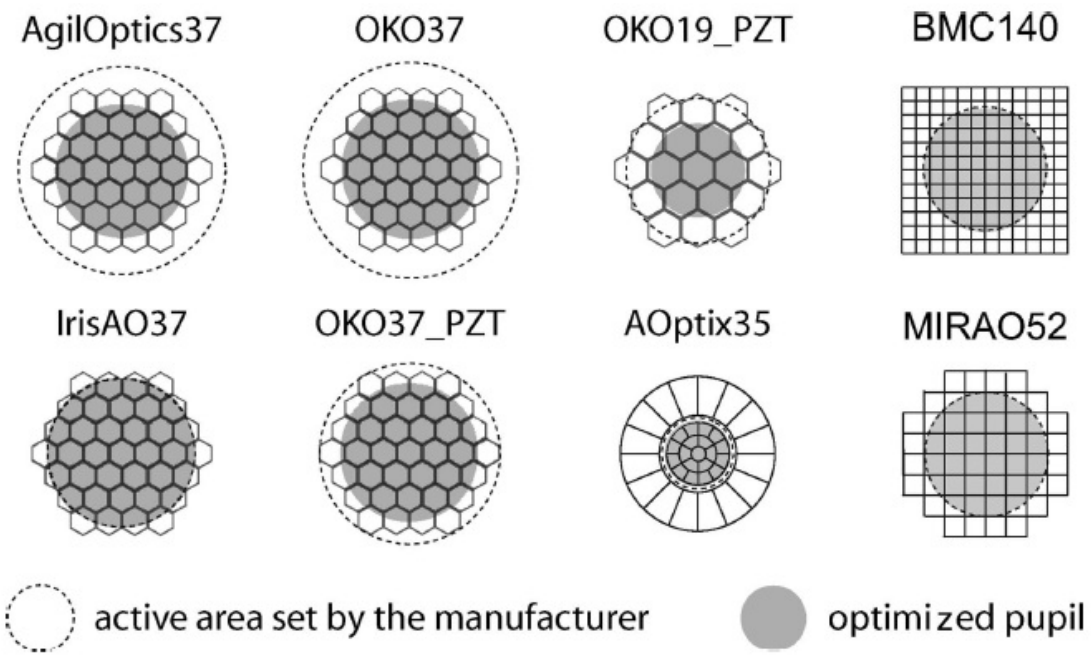

Fig. 3.18: Initial and optimised pupil superimposed on the actuators layout. [85]

functions. For example, the BMC DM is edge clamped, which means the edge actuators are not as free to move as the centre actuators. Therefore, the edge actuators are only used to shape the edge of the wavefront. The optimised pupils are shown in Figure 3.18.

The performance of those DMs was then simulated using the method explained in section 3.4.3, and their ability to correct ocular aberrations was quantified in terms of residual wavefront error RMS and Strehl ratio after their correction. These comparisons are shown in Figure 3.19. It is worth mentioning at this stage that the BMC 140 depicted in this paper is a different model compared to the one used in our setup. It has a 3.5 μm stroke, and 4.4 mm aperture (in comparison, ours has a 5.5 μm stroke, and 4.95 mm aperture).

The Boston Micromachines Corporations Multi-DM deformable mirror (BMC DM) used in this setup has a continuous gold plated membrane, operated by piston actuators (with one degree of freedom). A close-up of the mirror's surface is shown in Figure 3.20. It has a pitch (or actuator spacing) of 450 μm, and an interactuator coupling of 22% [86]. The influence function of a single actuator could then be modelled as a Gaussian deformation of the surface given by [7]:

$$I(x,y) = \exp\left[\frac{\ln(coup)}{r_c^2} r^2\right] \tag{3.27}$$

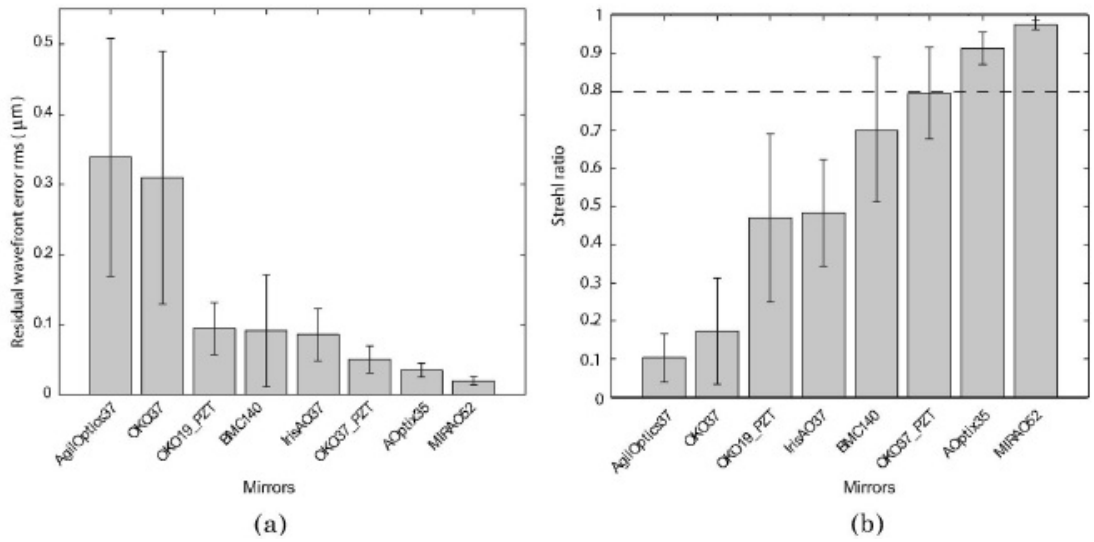

Fig. 3.19: Performance of the mirrors in correcting ocular aberrations: (a) Mean residual wavefront error RMS after the best fit given by the mirrors. (b) Mean Strehl ratio after the best fit given by the mirrors. The error bars represent ±1 standard deviation. [85]

where *coup* is the interactuator coupling, r_c is the pitch, and r is the radial distance between the actuator and the centre of the subpupil being corrected. However, the surface of this specific DM has been microstructured by design to minimise coupling between neighbouring actuators. Therefore, the Gaussian approximation is not accurate for this case [87]. A thorough investigation has been carried out to characterise the influence function matrix of the BMC DM (see section 6.3) and to test its performance (see section 4.1).

3.4.3 System control

In adaptive optics, the wavefront sensor and corrector are treated as a whole system. The control algorithm has to consider several aspects of this ensemble; the geometry by which they are matched, correction loop operation, phase reconstruction method, etc. This section discusses how these different factors come together in creating the control algorithm suitable to control an adaptive optics system.

First, consider the aberrations being corrected. Defocus changes as the eye accommodates to near and far objects [88]; however, medications are used in such experiments to dilate the pupil and freeze accommodation. Therefore in this study, defocus is considered a static term, and is corrected once at the beginning of the experiment. Higher order aberrations (HOA) are dynamic in nature. They are

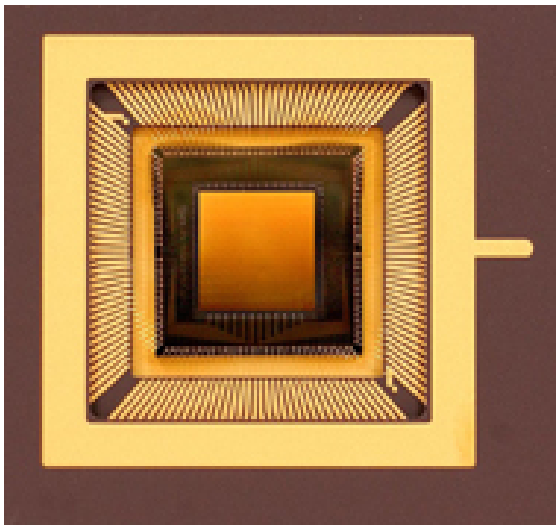

Fig. 3.20: A close-up of the Boston Micromachines Corporation deformable mirror with 140 actuators, 5.5 μm of stroke, 4.95 mm clear aperture. [86]

influenced by heartbeat, minor changes within the crystalline lens, microsaccades of the eye, and dynamics of the tear film [89]. Variations up to 70 Hz have been reported [19]; however, no advantages were reported, up to our knowledge, for correcting aberrations beyond $20 - 30$ Hz.

There are two different methods of reconstructing phase; zonal and modal. In the first method, phase is reconstructed over subapertures in one of several geometries. Consider a SHWS with square subapertures. The matrix equation relating the measurements matrix $\mathbf{S}$ and the phase matrix $\mathbf{\Phi}$ is then given by [72]:

$$\mathbf{S} = \mathbf{A}\mathbf{\Phi} \tag{3.28}$$

where $\mathbf{A}$ is an $(N \times M)$ matrix which expresses the slopes in terms of discrete phase values on a grid. Matrix $\mathbf{A}$ differs based on the sampling geometry. For the Fried model (see Figure 3.21), the measured slopes are given by [90]:

$$\begin{aligned} \mathbf{S}^x_{i,j} &= \left[(\phi_{i+1,\ j+1} + \phi_{i+1,\ j}) - (\phi_{i,\ j} + \phi_{i,\ j+1})\right]/2d \\ \mathbf{S}^y_{i,j} &= \left[(\phi_{i+1,\ j+1} + \phi_{i,\ j+1}) - (\phi_{i,\ j} + \phi_{i+1,\ j})\right]/2d \end{aligned} \tag{3.29}$$

where $\phi_{i,j}$'s are the phase values at the four corners of the subaperture, and $\mathbf{S}^x_{i,j}$, $\mathbf{S}^y_{i,j}$ are the measured slopes.

In modal reconstruction, a phase map over the full pupil is reconstructed, and

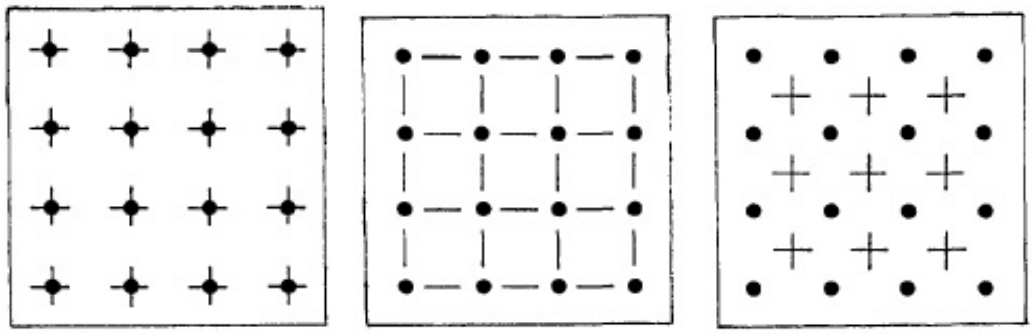

Fig. 3.21: Left-to-right: Southwell, Hudgin, and Fried sampling geometries. The horizontal dashes indicate positions of $x-$slope sampling. The vertical dashes indicate the $y-$slope sampling positions. The dots are mated phase points. [91]

represented using a set of orthonormal polynomials (e.g. Zernike polynomials). In this case, matching actuator positions in the corrector to their corresponding position on the sensor can be achieved by calculating the system influence function matrix [92]. After aligning the SHWS and DM within the optical setup, the actuators are poked one by one, and their influence functions are recorded using the SHWS. Then using a set of equations described later in this section, a matrix $\mathbf{M}^+$ is obtained, later used to control the corrector using phase information.

Adaptive optics operates according to one of two modes: open-loop and closed-loop. In the first mode, aberrations are measured and compensated for once at the beginning of the experiment, thus the corrector is set to a fixed position throughout the experiment. In the second mode, the wavefront sensor and corrector are parts of a feedback loop, where the phase is measured and corrected throughout the experiment. Some systems such as the one described here have fixed correction for some aberrations, and closed-loop operation for others. Another similar arrangement is the use of two DMs in a woofer-tweeter geometry [93], where the woofer DM is used to correct LOA in open-loop mode, and the tweeter DM is used to correct HOA in a closed-loop mode.

To create a closed-loop system, one needs to calibrate the system formed of the SHWS and DM, and measure its modes. Two methods are considered here:

- **Influence function matrix using phase:**

  After the SHWS - DM system is aligned into the optical setup, a plane wavefront is propagated throughout the setup where both the DM's surface in bias position and the lenslet array are conjugate to the pupil plane. It is important that the pupil size be the same as that used during the experiment.

The system modes [92] are then acquired by poking a single actuator at a time[3], and recording the resultant phase maps (see Figure 6.10). Assuming the bias position of each actuator to be zero, maximum push to be +1, and maximum pull to be -1; each actuator is set to +0.5, -0.5, and phase maps ϕ_{i+}, ϕ_{i-} are recorded. The normalised influence function of a single actuator is then a column matrix of size m, given by:

$$\phi_i = \phi_{i+} - \phi_{i-} \tag{3.30}$$

where i is the actuator index. The influence function matrix $\mathbf{M}$ $(m \times n)$ is formed such that:

$$\mathbf{M} = [\phi_1 \quad \phi_2 \quad ... \quad \phi_n] \tag{3.31}$$

The pseudo-inverse of $\mathbf{M}$, $\mathbf{M}^+$, could be computed using a singular value decomposition of $\mathbf{M}$ [27]:

$$\mathbf{M} = \mathbf{U}\mathbf{W}\mathbf{V}^T \tag{3.32}$$

where $\mathbf{W}$ is a diagonal matrix, with the diagonal entries representing the singular values. The pseudo-inverse is then calculated from [27]:

$$\mathbf{M}^+ = \mathbf{V}\mathbf{W}^{-1}\mathbf{U}^T \tag{3.33}$$

The set of commands to be sent to the DM, to correct a phase ϕ is then given by [27]:

$$c = \mathbf{M}^+\phi \tag{3.34}$$

Now since $\mathbf{M}$ was acquired using normalised stroke vectors, c is given according to the same notation, i.e. c entries range between -1 and 1, with 0 being the bias position. Therefore, the voltage matrix to be sent to the DM is calibrated according to the actuator deflection versus voltage graphs (see Figure 6.7).

[3] Predetermined clusters of actuators could be chosen instead, especially when calibrating DMs with a large number of actuators

- **Influence function matrix using slopes:**

  In this method, the influence function matrix $\mathbf{B}$ is formed from slopes rather than phase maps. Each column matrix S_i is formed of the set of slopes in the $x-$direction, followed by the set of slopes in the $y-$direction, and a single entry for the piston term. The latter serves to make sure the matrix does not become singular [7]. The matrix of slopes is given by [7]:

$$S_i = \begin{pmatrix} S_{i1x} \\ S_{i2x} \\ \vdots \\ S_{imx} \\ S_{i1y} \\ S_{i2y} \\ \vdots \\ S_{imy} \\ p \end{pmatrix} \tag{3.35}$$

  where i is the system mode index, S_{ijx}, S_{ijy} are the slopes of the ith mode at the jth position[4], in the x and y directions, respectively. $\mathbf{B}$ is then given by [7]:

$$\mathbf{B} = (S_1 \quad S_2 \quad ... \quad S_n) \tag{3.36}$$

  The set of actuator commands is then given by [7]:

$$c = \left[\mathbf{B}^T\mathbf{B}\right]^{-1}\mathbf{B}^T S \tag{3.37}$$

  where S is the measured wavefront slopes to be corrected for, rearranged as in Equation 3.35. Same note regarding the notation for c applies as above.

The first method was used to simulate the performance of the deformable mirror. After acquiring the influence function matrix, a hundred randomly generated eyes phase maps were generated according to the Thibos' model [94]. The actual phase projected on the DM is given by [27]:

$$\phi_M = \mathbf{U}\mathbf{U}^T\phi \tag{3.38}$$

[4] corresponding to a lenslet in the pupil plane

where $(\phi - \phi_M)$ represents the fitting error. The DM's ability to create the conjugate phase maps, to correct those hundred eyes was simulated (see section 4.1, and the residual RMS was reported as a figure of merit.

4. PRELIMINARY EXPERIMENTS

Two main experiments were carried out prior to designing the system. The experiments investigated the deformable mirror (DM) and the investigation of proposed light-emitting diodes (LEDs) for both wavefront sensing and illumination of the retina, in order to achieve a clearer understanding before finalising the optical design.

4.1 Deformable mirror characterisation

The BMC Multi-DM was chosen for its high resolution (140 actuators), small size, and potentially-lower price (compared to the Imagine Optics mirao™ 52-e and the ALPAO DM52). It has a clear square aperture of side 4.95 mm, not too far away from a 1:1 ratio with the eye's pupil (a 6 mm pupil is used in our experiments). The manufacturer supplies a LabVIEW driver for it, which could be easily embedded into our system control panel. It suffers from a limitation in stroke (5.5 μm); and since it is a membrane mirror, the edge actuators should be avoided [20].

Due to its limitations, the prospective mirror had to be characterised to confirm a good level of correction before placing an order for the actual mirror, or designing the whole system around it. We did not have that mirror in the group, so we used the closest available DM to simulate its function. A BMC DM (140 actuators, 3.5 μm stroke, and 4.4 mm side) was characterised using a commercial Fisba© Twyman-Green interferometer. Actuators were poked one by one, then chosen clusters were poked, and the resulting phase maps were recorded and analysed later using IDL 7.0.6. A random sample of a hundred eyes' aberration maps were generated according to the Thibos' model [94] using Matlab® 2009a, and the DM's ability to correct those aberrations was calculated (see Table 4.1). To extrapolate from the 3.5 μm to the 5.5 μm stroke, the ratio of peak-to-valley stroke values taken from the manufacturer's specification sheets was used to scale the acquired phase maps, with the assumption that the inter-actuator coupling

Tab. 4.1: Simulated performance of the BMC DM (140 actuators, 5.5 μm stroke). The errors are measurement percentage errors of the interferometer used to characterise the deformable mirror.

DM corrects:	defocus astigmatism and HOA	astigmatism and HOA only	HOA only
Residual RMS (nm)	89.4 ± 4.3	59.1 ± 2.8	45.8 ± 2.2
Strehl ratio (@ 633 nm)	0.455 ± 0.022	0.708 ± 0.034	0.813 ± 0.039

for both mirrors remains unchanged. Although the inter-actuator coupling for the new DM was higher, it was compensated for using a larger pupil, and consequently, larger inter-actuator spacing. The theory involved in calculating the influence function matrix from phase maps, and how adaptive optics correction is achieved is described in detail in section 3.4. Three cases were considered:

- The DM corrects defocus, astigmatism, and higher-order aberrations (HOA).
- The DM corrects astigmatism and HOA only, defocus is corrected separately.
- The DM corrects only HOA, and both defocus and astigmatism are corrected separately.

The procedure was repeated after the new BMC DM was received to verify the simulation results, and similar results were obtained. These results simulated the ability of the DM to correct randomly generated aberration maps formed of a linear combination of a large number of orders or Zernike modes. This meant that in a practical setup, correcting defocus separately using a Badal optometer, the wavefront of light could be corrected near the diffraction limit[1]. Adding more optics to correct astigmatism has a quality advantage, but adds to the complexity of the setup; thus this decision was deferred until retinal images were obtained and assessed. The method used to calibrate the BMC DM is explored further in section 6.3.

Devaney et al. compared the performance of several deformable mirrors in correcting ocular aberrations [85]. Better performance was achieved (in terms of residual RMS) by this BMC DM, which is expected due to the higher actuator

[1] Zernike polynomials up to fifth order were considered in this simulation.

stroke (5.5 μm versus 3.5 μm); however, the correction was still not sufficient to use the DM without a separate defocus correction mechanism.

4.2 Investigation of light emitting diodes

Light emitting diodes (LEDs) that are directional with high power are being manufactured. Compared to a laser or a superluminescent diode (SLD), an LED is much cheaper, less coherent, and less directional. High coherence sources typically produce a speckle pattern when illuminating the retina, which in turn affects measurement precision. Solutions to the speckle problem (such as scanning mirror) could be expensive, and add complexity to the system. Due to these facts, LED candidates were considered as light sources for both wavefront sensing and imaging arms.

An infrared LED was suggested as a probe beam source, and two LED candidates were investigated. The first candidate was a *Thorlabs LED780E* with the specifications in Table 4.2 and radial intensity distribution shown in Figure 4.1. It was chosen because it emits in the infrared, which is safer and more comfortable for the human eye. With a total radiant flux of 18 mW (of which 7.2 mW are within the 10° divergence half-angle), it appeared as a good candidate for wavefront sensing. In practice, we were able to achieve 1.8 mW of optical power immediately after the collimator. Modelling the few optical components that fall between the source and the eye (including a pinhole to produce a point source), the flux at the pupil plane was calculated to be $< 1\ \mu W$. Due to the low reflectance of the retina, the light coming out would not be sufficient for the wavefront sensing task. This candidate was eliminated because it does not deliver sufficient power for wavefront sensing.

The second candidate was an *OSRAM SFH4550* with the specifications listed in Table 4.2 and radial intensity distribution shown in Figure 4.1. This LED has more power and less divergence. We were able to achieve 8.44 μW at the pupil plane. Using a slightly high gain (~ 1.2) at the SHWS camera, a consistent phase map could be achieved. At 850 nm, the safety limit is higher, and so we could shine more light into the eye. On the other hand, due to chromatic aberrations, the large wavelength difference between the probe and imaging beams should be accounted for while designing the system. Although 850 nm travels deeper into the retina, it had been shown that it can be used for wavefront sensing [95]. The main aberration affected by LCA in this case is defocus [49], and the difference was

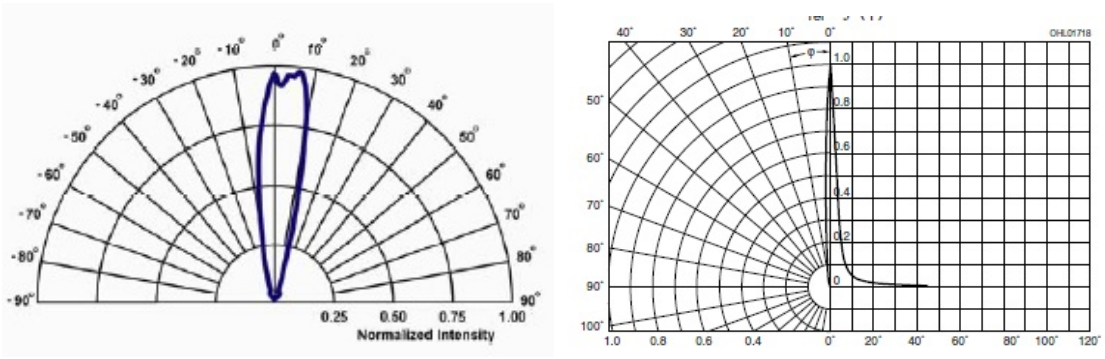

Fig. 4.1: Typical radiant intensity distribution of the *Thorlabs LED780E* (left) and the *OSRAM SFH4550* (right) LEDs. [96, 97]

Tab. 4.2: Specifications of candidate LEDs. [96, 97]

	*Thorlabs LED*780*E*	*OSRAM SFH*4550
Wavelength (nm)	780 ± 10	850 ± 35
Divergence half-angle(°)	10	3
Total radiant flux (mW)	18	50
Measured flux(mW)	1.8	> 20
Emitter size (mm^2)	0.4×0.4	0.3×0.3

calculated and included in the distance between the imaging lens ($L6$ in Figure 5.7) and the CCD camera. Another factor to consider here is the bandwidth of the light source ($\sim 70\ nm$), which causes about ($0.14\ D$) of defocus range.

The emitter size of the LED is $0.3 \times 0.3\ mm^2$ and has a varying intensity profile. To produce a point source at the retina ($\sim 20\ \mu m$ in diameter), a pinhole was put in place to choose a smaller portion of the emitter size, and it was demagnified. Figure 4.2 is an image of the emitter shape. Figure 4.3 shows the plane wavefront produced from the chosen area, used to form a point source on the retina for wavefront sensing.

For the imaging LED, the *Luxeon MR-M0100-20T Rebel Tri-Star* (shown in Figure 4.4) was suggested since it has been shown to work in a similar setup [98] albeit with a large area of retinal illumination. Our setup has a few more optical elements after the eye, which translates to more losses (especially at the DM), and longer exposure is needed for image acquisition. The *Tri-Star* consists of three LEDs forming a triangle on a circle's circumference. Each has a typical luminous flux of 161 lm (or 2.36 W) at 700 mA. They have a typical spectral half-width of 30 nm ($520 - 550\ nm$) and a typical viewing half-angle of 62.5° (as shown in

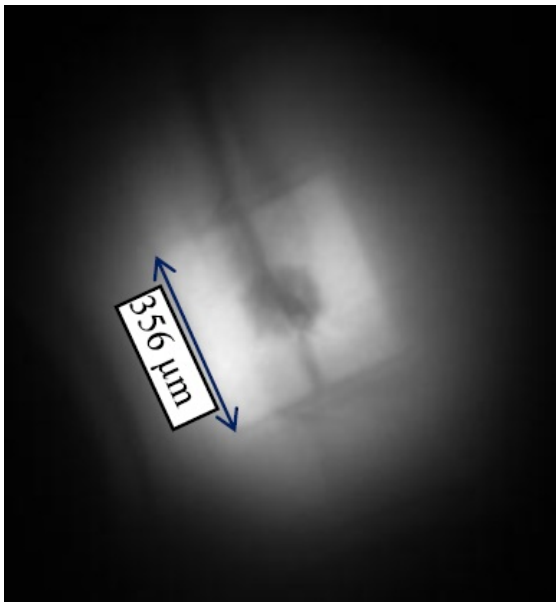

Fig. 4.2: Emitter size on the CCD corresponding to 121 μm on the retina.

Figure 4.5) [99]. When imaged onto the pupil, the three LEDs enter through the outer 1 mm of the dilated pupil. The images of the three LEDs coincide on the retina forming a large homogeneous illuminated circle (shown in Figure 4.6). The standard deviation of intensity within the 4° FOV is $< 1\%$. The total intensity at the level of the pupil is 60 μW.

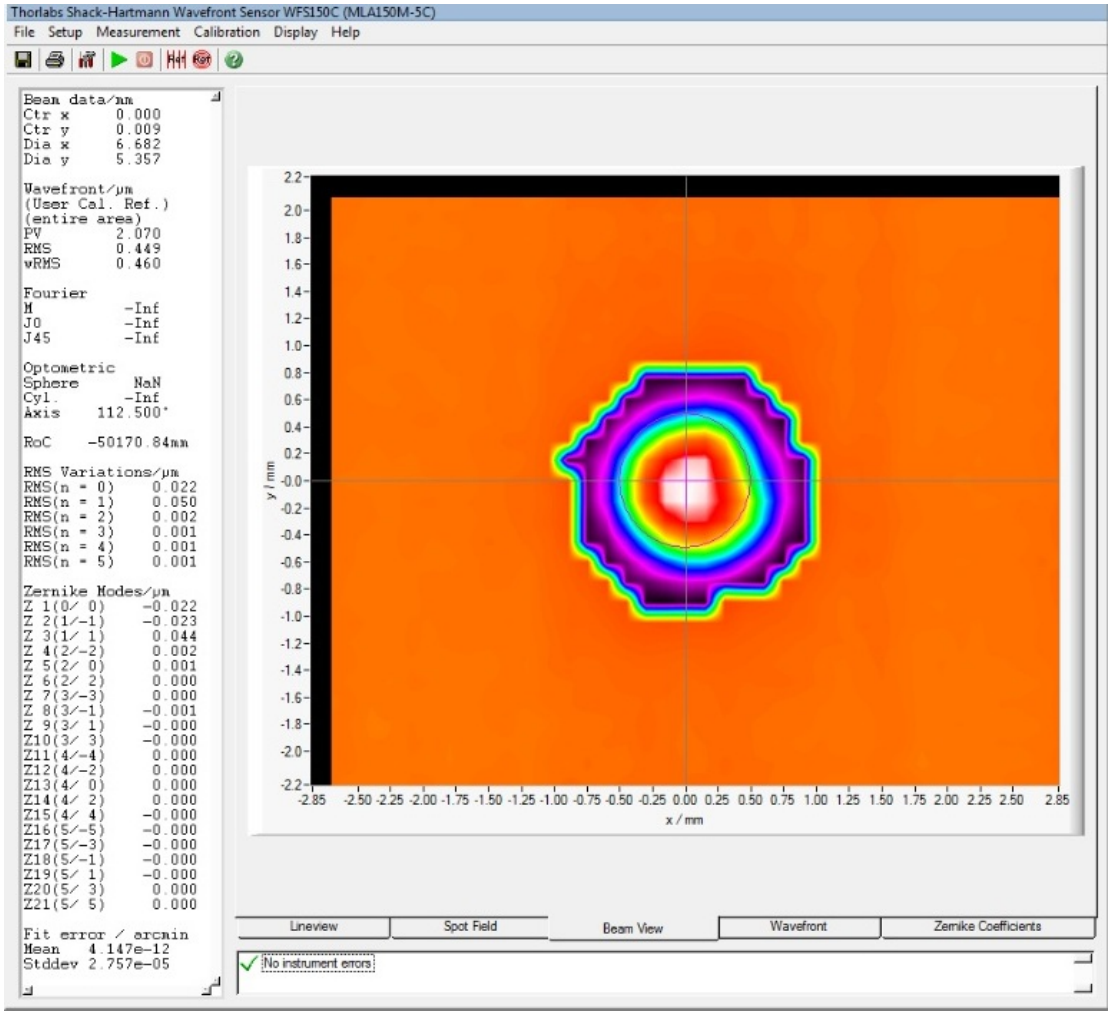

Fig. 4.3: Plane wavefront used for wavefront sensing. The LED is imaged with a lens of focal length f, where the wavefront sensing LED and its image are positioned at $-2f$ and $+2f$, respectively. A diaphragm is then placed in the image plane to choose a predetermined uniform illumination region of the LED image. This is then collimated to produce the plane wavefront shown in this figure.

Fig. 4.4: The geometry of the three LEDs in the *Luxeon MR-M0100-20T Rebel Tri-Star*.

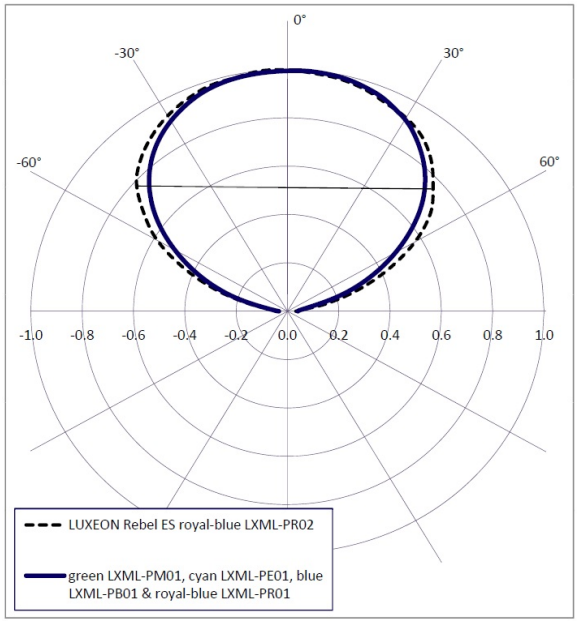

Fig. 4.5: Typical radial intensity distribution of the *Luxeon LXML-PM01-0100* LED; part of the LED assembly on the left. [99]

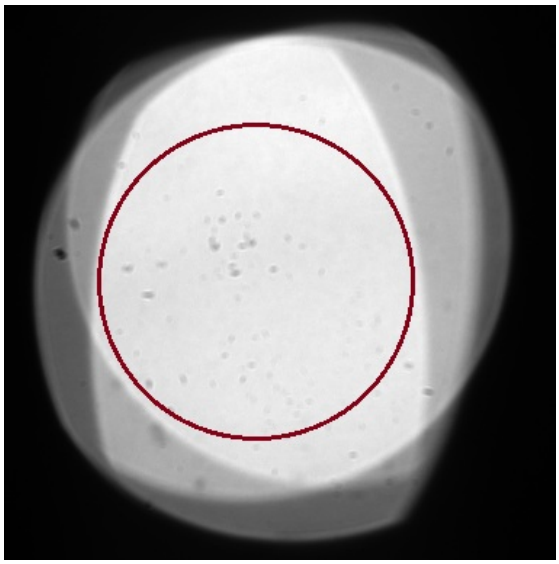

Fig. 4.6: The uniform illumination ($< 1\%$ standard deviation) formed on the retina as the overlap of the three LEDs. Circle diameter $= 4°$.

5. SYSTEM DESIGN

5.1 General considerations in optical design

Several variables should be considered when designing an optical system, from light path through the system and image quality to ergodynamics and space considerations. The major variables associated with designing this optical system are discussed in this section.

- **Deformable mirror:** The main component which the system is designed around is the deformable mirror. The Boston Micromachines Corporation deformable mirror (BMC DM, 140 actuators, 5.5 μm stroke) was chosen for this system after it was studied, and its performance was simulated (see section 4.1). It has a square active surface of side 4.95 mm. It can be used to correct higher-order aberrations (HOA) in one of two configurations; retroreflection (where the incident ray is reflected upon itself) and reflection at an angle (separating the incident and reflected rays). The first configuration involves the addition of an extra beamsplitter, cutting the light intensity by at least a factor of four. Since the light coming out of the eye is already weak, and we are limited with the amount of light we could shine into the eye for safety reasons, this configuration was discarded.

  In the second configuration, choosing the reflection angle introduces a trade-off. The smaller the angle is, the longer distance is needed to separate both rays, introducing more light losses and increasing the size of the system. On the other hand, increasing the angle causes some tilt, where the circular beam becomes an ellipse at the DM level. Due to the deviation from a circle, some actuators will be omitted. Taking this trade-off and other geometrical reasons into account, the DM was placed to form a 22.5° angle of incidence with the beam. The beam diameter was set to avoid the edge actuators. The beam would form an ellipse whose major diameter is 3.9 mm (horizontal) and minor diameter is 3.6 mm (vertical).

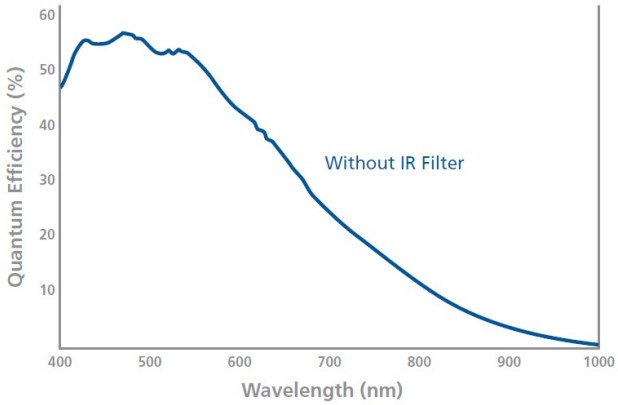

Fig. 5.1: Spectral response of the Retiga-2000R CCD camera. [101]

- **Shack-Hartmann wavefront sensor:** The second component to be considered was the Shack-Hartmann wavefront sensor (SHWS). Another trade-off governs the choice of the lenslet array associated with the SHWS. To better sample the wavefront and get a more accurate reading of phase, the number of lenslets sampling the pupil should be increased. On the other hand, the amount of light reaching the lenslet array level is a constant, and is divided between the lenslets; therefore, a higher number of lenslets would lower the signal-to-noise ratio. A *Thorlabs WFS150-5C* SHWS was chosen for wavefront sensing. It offers a 150 μm pitch[1] lenslet array. Choosing to use 16 lenslets across the pupil diameter of 6 mm delivered a fair compromise between sampling and signal-to-noise ratio. The SHWS operates over a wide wavelength range ($300 - 1100$ nm), and has an effective focal length of 3.7 mm, a lenslet pitch of 150 μm, and a 1.3 megapixels CCD camera [100].

- **CCD camera:** The science camera to image the retina was chosen to meet three criteria. First, high quantum efficiency at the imaging wavelength (530 nm, see Figure 5.1). Second, high resolution where 1 μm on the retina is matched to 1 pixel on the camera. Third, monochromaticity; since colour CCD arrays have one blue, one red, and two green pixels for each pixel in a monochromatic camera; therefore, to achieve the intended high resolution without any artefacts caused by pixels displacement, the camera had to be monochromatic. The Retiga-2000R (1600×1200 pixels, 12-bit digital output, pixel size of 7.4 μm) [101] was found to best match those requirements.

[1] Pitch: distance between the centres of two adjacent lenslets.

The defocus term which appears as a consequence of longitudinal chromatic aberrations (LCA) due to the wavelength difference between the wavefront sensing and illumination light sources was modelled using Zemax (see section 5.2), and accounted for by moving the imaging camera closer to the imaging lens (L6 in Figure 5.7). Since defocus is still measured in the infrared and corrected for using the Badal optometer, a residual defocus term (for green) should appear when we deal with non-emmetropic eyes. Hence, the imaging camera was given one degree of freedom by placing it on a *z-axis* translational stage, to help achieve best focus, and add the ability to focus on different layers of the retina.

- **Lenses:** The choice of lenses was based on five main considerations: minimising aberrations, full-field propagation, beam size, tolerance, and coating. Monochromatic aberrations increase with high numerical aperture (see section 3.3.1); therefore, low numerical aperture lenses were chosen. This has a second advantage, which is allowing the whole 4° field-of-view (FOV) to propagate throughout the system without vignetting. The beam cross-section started as a circle at the eye's pupil ($d = 6\ mm$), to an ellipse at the DM ($d_1 = 3.9\ mm, d_2 = 3.6\ mm$), to a circle at the SHWS lenslet array ($d = 2.4\ mm$). This magnification was achieved by altering the ratios between the focal lengths of the lenses in two $4f$ systems. The imaging lens was chosen to obtain a 1 μm (on the retina) to1 pixel correspondence. Lenses were chosen to have longer focal lengths to allow for a good performance over small misalignment errors, especially with the positioning of the human subject. Lens coatings were chosen according to the light passing through them. In the common path, anti-reflective coating in the visible range was chosen after a personal communication with Thorlabs engineers was made, and an extrapolated curve of reflectance (into the infrared) was obtained (see Figures 5.2, 5.3). All lenses were chosen to be achromatic (to minimise chromatic shifts) and off-the-shelf (to minimise cost). The system was modelled using Zemax to confirm those five criteria were met (see section 5.2).

- **Cold mirror:** To separate the wavefront sensing and imaging beams, a *Thorlabs FM03* was chosen due to its transmission curve (see Figure 5.4) and its finesse ($3 - 4$ waves flatness @633 nm over the whole 25.4 mm diameter) [103]. It was placed at 45° to the incident beam.

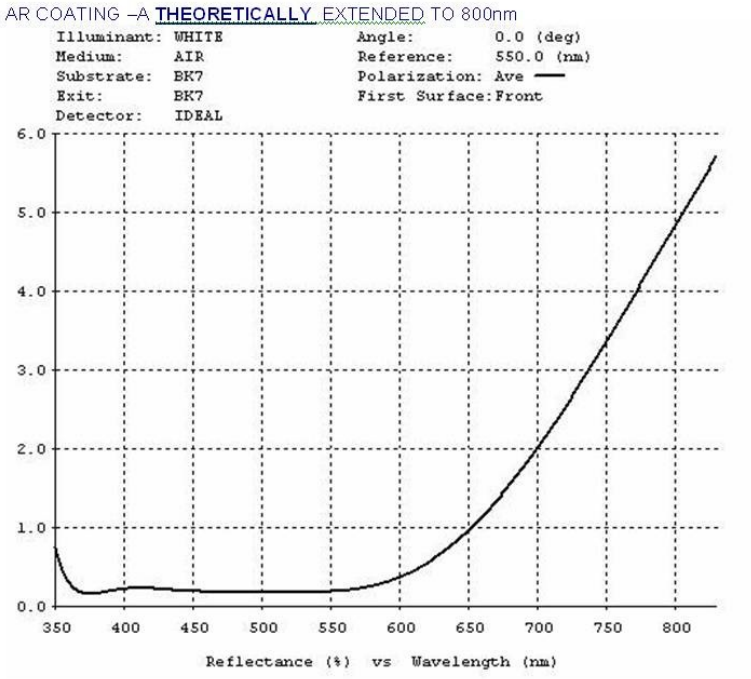

Fig. 5.2: Reflectance of anti-reflective coating -A, theoretically extended to 800 *nm*. [102]

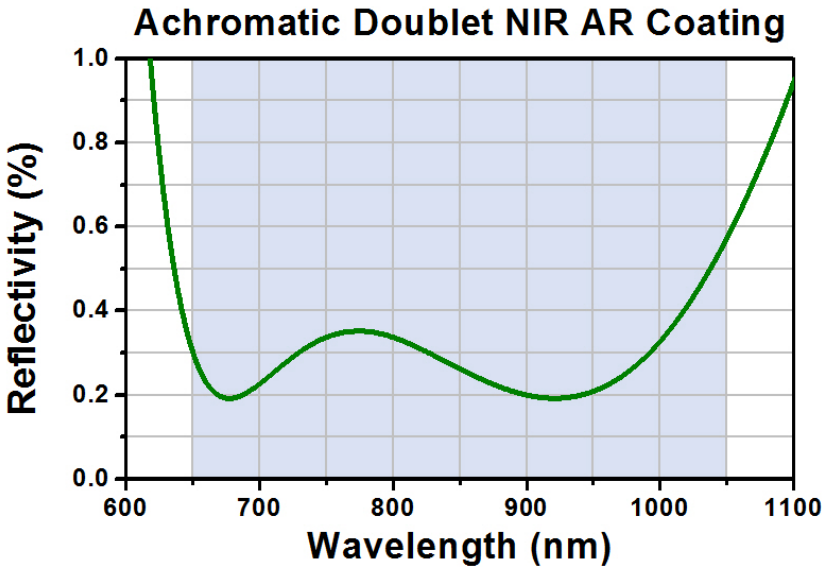

Fig. 5.3: Reflectance of anti-reflective coating -B. [102]

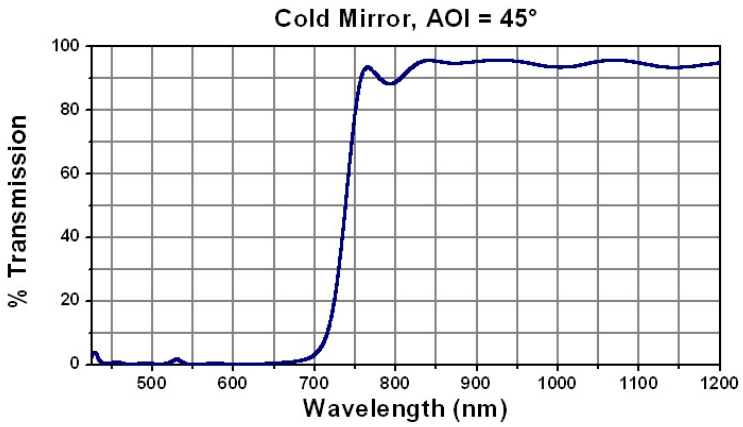

Fig. 5.4: Transmission curve of the *Thorlabs FM03* cold mirror. [103]

- **Badal optometer:** The Badal optometer was added to correct for defocus once at the beginning of the experiment. Since the subject's eye accommodation is to be frozen during the experiment, the defocus term is considered constant throughout. The Badal optometer was formed using two fixed lenses ($L4$ & $L5$ in Figure 5.7) where two mirrors were mounted on a translational stage to vary the distance between the two lenses, therefore affecting the wavefront vergence. Choosing longer focal lengths gives the advantage of more sensitivity (smaller steps) in correcting defocus, but it requires a longer translation distance. The Badal optometer was designed to correct for at least ± 4 D. A computer controlled electrical translational stage was chosen for precision, repeatability, and ease of access.

- **Cage system:** A Thorlabs cage assembly system was chosen as a rigid structure that simplifies the alignment process, and is compatible with the different optical components used to build the system. The cage system, however, has two disadvantages; it allows neither for tip/tilt correction, nor for lateral shift correction. For example, the lateral shift, however small, introduced by a beamsplitter would propagate throughout the system. To correct for that, the two beamsplitters in our design were mounted so that one would correct the lateral shift introduced by the other.

- **Light budget:** The retina of the human eye is very sensitive to light, but it has a low damage threshold. Therefore, health and safety regulations must be adhered to when shining light into the eye. Moreover, the reflectivity of the retina is very low (discussed further in section 3.2). Due to to those

reasons, the light levels should be controlled within a window that is bright enough to be sensed by the SHWS and the science camera, yet significantly below the safety limit of the eye (see Appendix B). The radiant flux values in the pupil plane were measured to be 8.44 μW at 850 nm for wavefront sensing, and 60 μW at 530 nm for illumination. These values are $< 10\%$ of the safety limits, and produce a sufficient signal-to-noise ratio at the detectors.

The investigation that led to the choice of the light sources is fully discussed in section 4.2.

- **Comfort of the subject:** Subject comfort is an essential part in the design of the optical system. It is vital for the success of the experiment as well as for the safety of the subject. A UHCOTech HeadSpot was chosen and positioned at a comfortable height, and coupled to a height adjustable seat. It is a fast and comfortable method to align the subject into the system. Its repeatability is lower than a bite bar, yet it is more convenient for the subject. The Headspot offers three degrees of freedom for quick alignment. The experiments will run for short periods of time, and the subjects will be informed that they can relax at any time (further discussed in section 5.4).

- **Ease of access:** The equipment is controlled either mechanically or electronically. The mechanical parts are to be aligned prior to the subject's arrival. The rest of the equipment is controlled using a computer during the experiment. The only two parts to be mechanically moved during the experiment are the Headspot (for the alignment of the subject) and the science camera (to achieve best focus). The latter is controlled from the side of the table, made easily reachable by design.

5.2 Zemax modelling of the optical setup

Two main arms were simulated using Zemax; to achieve best performance, minimise aberrations, ensure the FOV is not truncated, and optimise the distances between the lenses. The system was unfolded, and treated as a static system where the Badal optometer was set to an emmetropic eye position. The two main arms considered here were:

- **Wavefront sensing arm:** This arm starts with a plane wavefront coming out of the eye's pupil, with the rays parallel to the optic axis considered

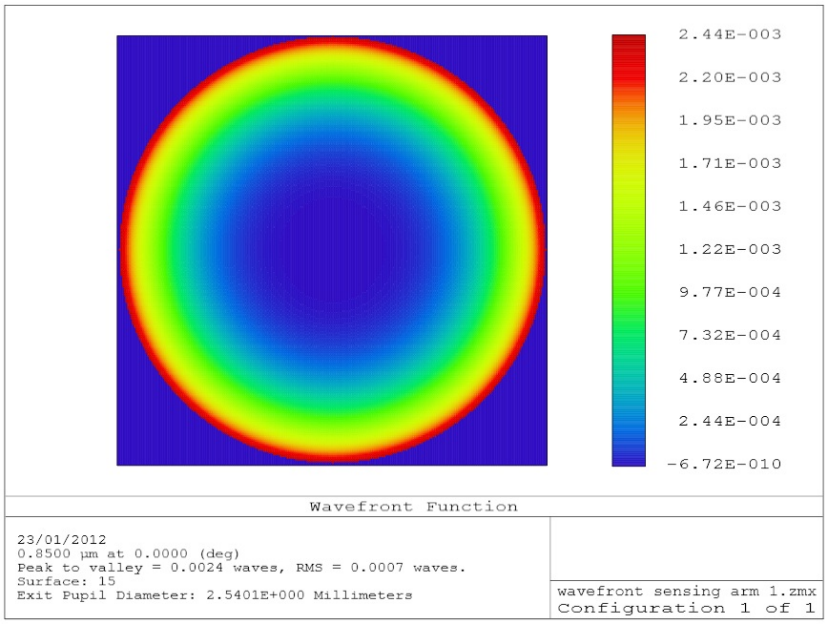

Fig. 5.5: Residual RMS wavefront error of the wavefront sensing arm in the Shack-Hartmann wavefront sensor lenslet array plane, predicted by Zemax.

(field angle = 0°). The light then propagates through the Badal optometer, reflects off the deformable mirror (considered flat in this case), through a telescope and onto the SHWS. This arm was optimised to achieve a plane wavefront in the SHWS lenslet array plane. The optimisation resulted in a residual RMS wavefront error of 7×10^{-4} waves (see Figure 5.5).

- **Imaging arm:** This arm starts with a plane wavefront coming out of the eye's pupil, with a ±2° FOV. The common path was copied from the optimised values for the wavefront sensing arm, while the non-common path was the variable optimised for best images at 530 *nm*. The simulation reveals a diffraction-limited performance over the whole 4° FOV (see Figure 5.6).

5.3 Design parameters

The schematics of the retinal imaging system with adaptive optics are shown in Figure 5.7. It was designed after careful consideration of the design parameters in sections 5.1 and the Zemax optimisation in section 5.2. The design parameters are displayed in Table 5.1.

The system consists of two main arms. The wavefront sensing arm uses an infrared LED as a light source. A point source is formed by imaging the LED

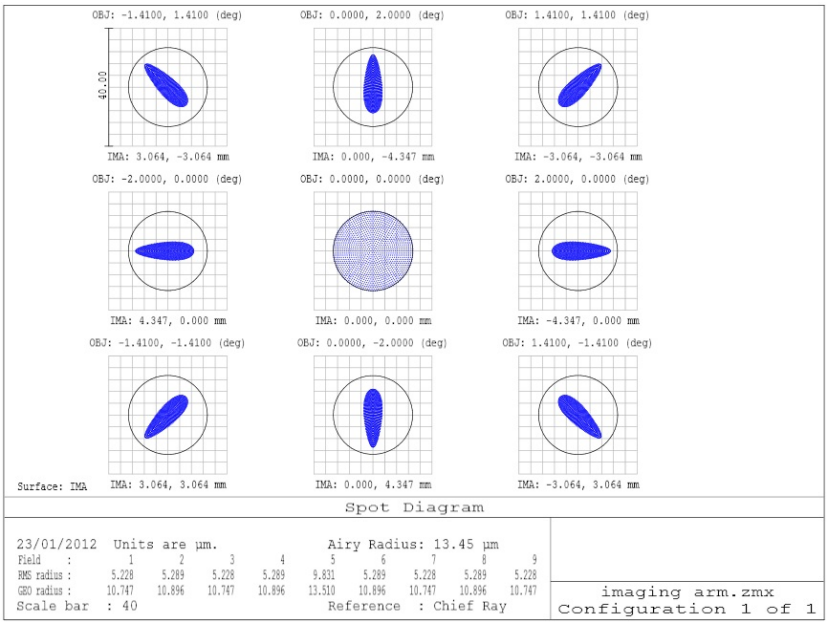

Fig. 5.6: Spot diagram covering a 4° field-of-view in the retinal camera plane, with a diffraction-limited performance predicted by Zemax. The system was optimised by setting a weight of 1 for on-axis propagation and of 0.5 for the ±2° FOV points, so that aberrations would be minimised across the 4° field while limiting the geometrical PSF size to the Airy disc diameter. The black circle represents the Airy disc.

Tab. 5.1: Design parameters - Lenses

Lens	$f(mm)$	$f_b(mm)$	Anti-reflective coating
L1	300.2	297.0	visible
L2	150.0	146.1	visible
L3	100.0	97.1	infrared
L4	250.0	246.7	visible
L5	150.0	146.1	visible
L6	74.9	70.3	visible
L7	75.0	69.9	infrared
L8	50.0	45.0	infrared

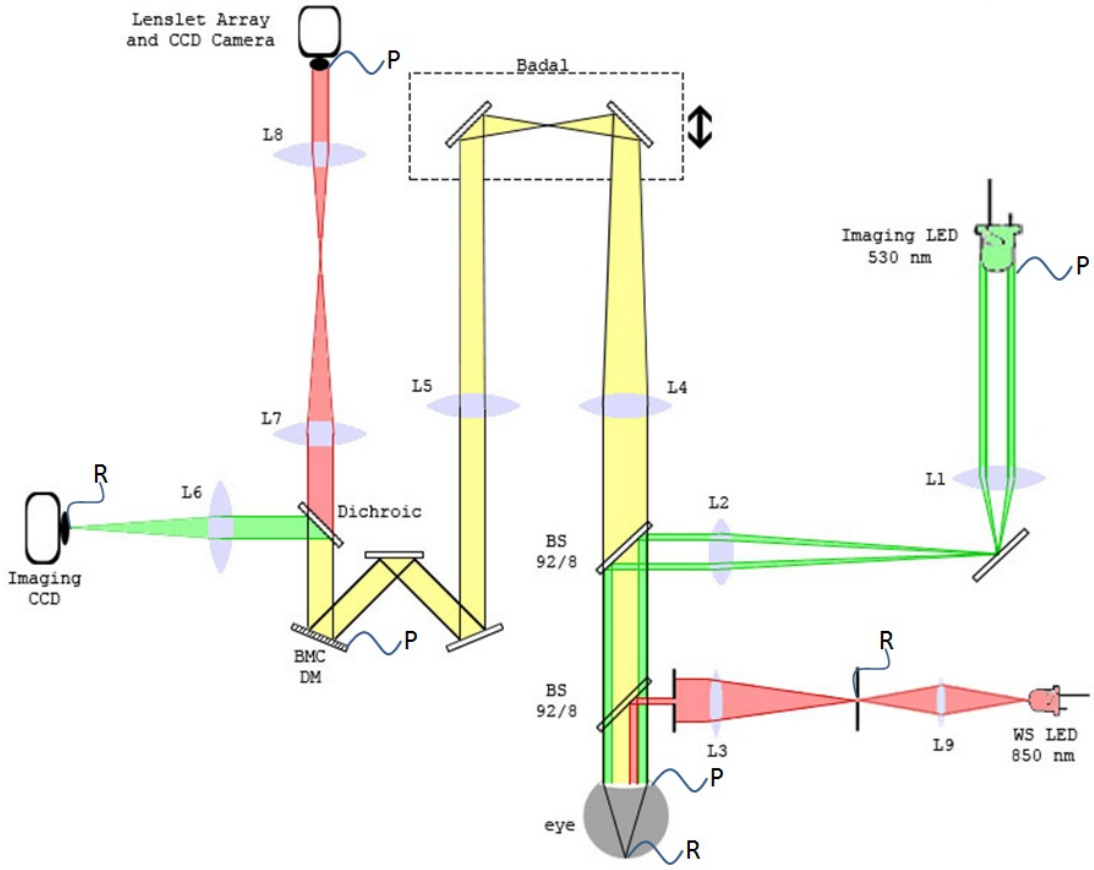

Fig. 5.7: Schematics of the retinal imaging system with adaptive optics. Red beam represents the 850 *nm* light used for wavefront sensing. Green beam represents the 530 *nm* light used as a flashlight. Yellow beam represents the common path. BS: beamsplitter. BMC DM: Boston Micromachines Corporation deformable mirror. P: pupil conjugate plane. R: retinal conjugate plane. (Figure not drawn to scale.)

Tab. 5.2: Design parameters - Distances

Between	Distance (mm)
Imaging LED & L1	296.9
WS LED & L9	57.5
L9 & L3	150.8
Eye & L3	100.0
Eye & L2	146.1
Eye & L4	250.0
L4 & L5	394.2
L5 & BMC DM	150.0
BMC DM & L6	74.9
BMC DM & L7	75.0
L6 & CCD	69.3
L7 & L8	114.8
L8 & SHWS	50.0

emitter onto a pinhole. This forms a spot with a diameter of about 20 μm on the retina. The light coming out of the eye is then corrected for defocus using the Badal optometer, and is reflected off the DM onto the SHWS. This forms a closed feedback loop where the wavefront of the light is measured using the SHWS, and is corrected for using the DM. The loop runs at $7-8\ Hz$, with the SHWS camera exposure time as the bottleneck. The DM and the lenslet array of the SHWS are conjugated to the pupil plane.

The imaging arm uses three green LEDs which are conjugated to the pupil plane, uniformly illuminating a 4° patch of the retina. The reflected light is corrected for defocus using the Badal optometer. The residual aberrations are corrected for at the DM. The green light is then reflected onto the science camera. The camera could be moved in respect to the imaging lens to correct for chromatic shifts, and focus on different layers of the retina. The 4° FOV corresponds to 1192 pixels on the camera (0.2 arcmin : 1 pixel). The size of the smallest cones (0° eccentricity) is 0.5 acrmin [104]. Since the smallest feature we intend to image is foveal cones, the science camera was chosen to satisfy the Nyquist criterion (2 pixels per feature) [105]. The science camera is conjugated to the retinal plane.

Two secondary elements (not shown in Figure 5.7) were added to the system; a webcam which is used for pupil alignment, and an artificial eye (made of a lens and a black scattering surface). Both could be temporarily in-line with the system during the alignment process, and are then removed to eliminate any unnecessary reflections.

A picture of the final setup is shown in Figure 5.8.

5.4 Health and safety

This section discusses the health and safety code followed throughout this work. It is essential that anyone attempting to use the equipment, or else, replicate the procedure will abide by these safety rules. We start by discussing general laboratory safety rules where the researcher must be familiar with the equipment they are using, and all the hazards and warnings concerned with that equipment. The researcher must be aware of unstable objects, flammable objects, and the emergency rules that have to do with the work space. Three main hazards are discussed in more detail here due to their relevance to this particular work.

Light emitting diodes (LEDs) have been omitted from safety standards until recently, when their technology advanced and they became commercially available with high intensities [106]. Both LEDs (wavefront sensing source and illumination source) in this setup are **not** eye-safe if powered fully on and held in front of the eye; however, the light levels at the pupil in the system have been shown to be $< 10\%$ of the maximum permissible radiant exposure set by European and American safety standards (see Appendix B). Both LEDs were enclosed along their travel path to protect accidental damage to human eyes. Special precautions must be taken when uncovering those LEDs. As an extra precaution, the light intensity at the level of the pupil should be measured prior to starting any experiment with a human subject.

Tropicamide ($0.5 - 1\%$) is a medical eye drop used to dilate the pupil and freeze the accommodation of the subject's eye during the experiment. As for most medicine, Tropicamide has some adverse effects. Thus, a collaboration was formed with the Ophthalmology Department at University College Hospital where subjects are tested prior to the experiment for eligibility (e.g. angle-closure glaucoma). They were then given a contact at the hospital in case any adverse effects arise in the twenty-four hours that follow the experiment.

Comfort of the subject and accessibility to the device were taken into account, since they have an effect on the subject's safety. Adjustable chin rest and seat are provided to guarantee that the subject's back and neck are placed safely throughout the experiment. It is made clear to the subjects that they are to blink, pause, or even quit the experiment as they please. They are frequently asked if they are comfortable. The experiment is not to take place for longer than

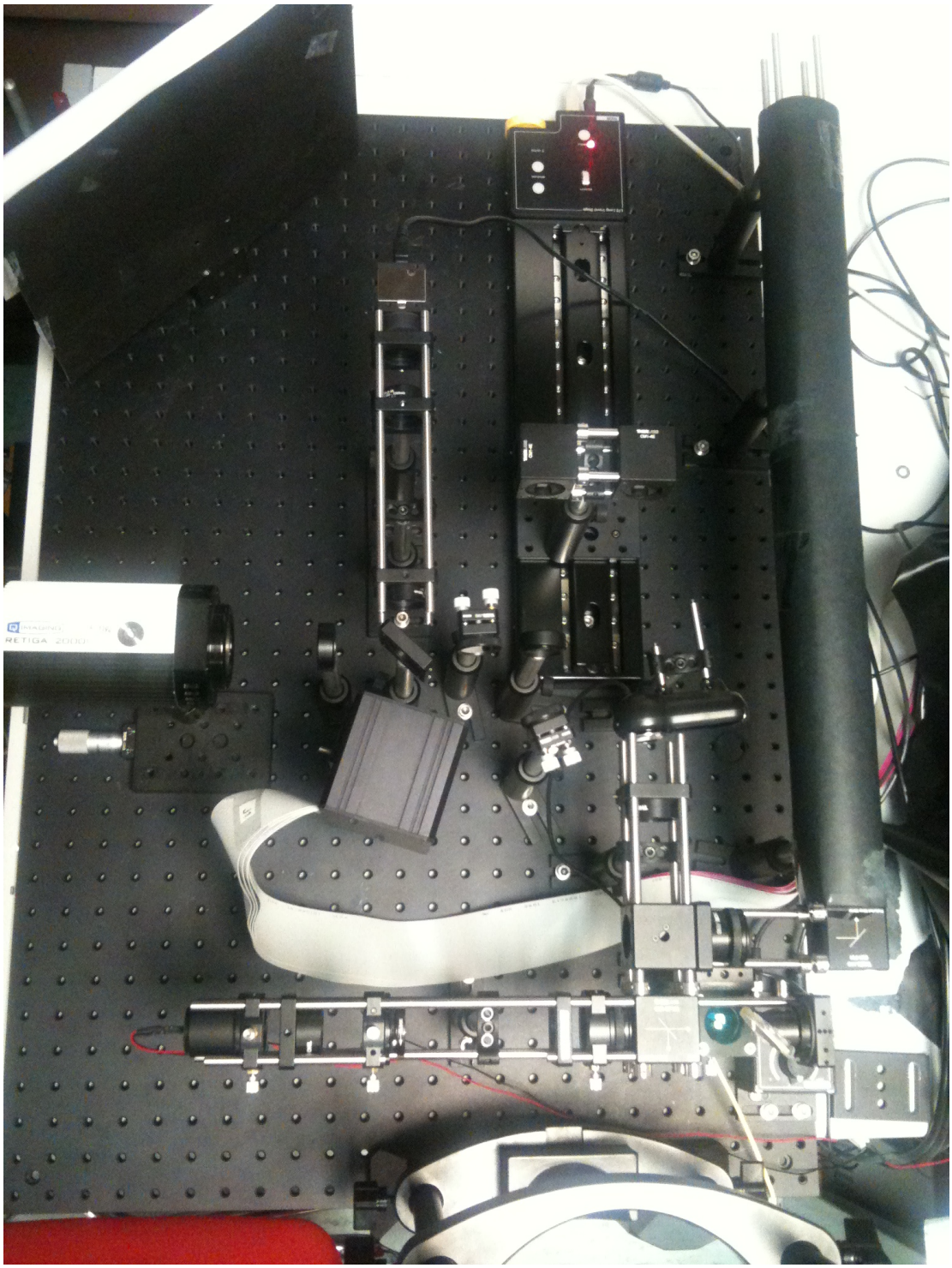

Fig. 5.8: A picture of the adaptive optics fundus camera. The breadboard dimensions are $60 \times 90\ cm^2$. The optical parts and paths are illustrated in Figure 5.7.

two hours per session.

The subjects are informed of any relevant hazards, and are asked to sign a consent form. An ethics approval has been granted to conduct this experiment by the Research Ethics Committee at the National University of Ireland, Galway (Ref 09/July/04).

6. SYSTEM ALIGNMENT

The underlying theory of the adaptive optics retinal imaging system was introduced in chapter 3, and the design considerations were discussed in chapter 5. This chapter goes on to discuss the considerations involved in building, aligning, and calibrating the optical system.

6.1 Alignment process

Many variables are involved when building an optical system. To achieve the optimum performance, the following parameters were considered:

- **Cage system:** A Thorlabs cage system was chosen for its high rigidity, stability, ease of alignment, and compatibility of the optical elements of the system. It uses rods that pass through optic mounts, ensuring all optical elements are lined-up. It can be used to bend the beam as well, mostly at right angles. However, it provides limited degrees of freedom. It is designed to propagate a straight beam through the centre of each optical element. It does not allow for tip/tilt corrections. Off-axis beams can be introduced using a pupil mounted on an "x-y linear translation mount". Therefore, the cage system was used throughout the straight parts of the optical system. Its shortcomings in lateral shifts, tip and tilt are discussed later.

- **Alignment beam:** It is vital that the beam used to align the system is stable and well-collimated. A $\mathbf{TEM}_{00}$ plane wave was produced using a stable 5 mW diode laser coming out of a single-mode fibre as a point source, coupled to a collimating lens. The fluctuation of measured phase of the source was $\sim 20 - 30$ nm. The plane wave was checked using a shear plate, where the interference pattern defines the divergence of the beam (see Figure 6.1). The shear plate reflects the light using two almost parallel surfaces placed at a $45° - 49°$ to the incident beam [107]. The separation between the two surfaces causes two effects; a lateral separation between the

Fig. 6.1: The shear plate uses two reflections of the same beam, separated by an optical path difference. Their interference causes a pattern that defines the beam's divergence. [108]

two reflections on the viewing screen, and an optical path difference (equal to twice the thickness of the plate) between the two reflections. If the beam is collimated in the plane of the viewing screen, the fringes due to the interference of two plane waves appears (i.e. a straight pattern of bright and dark fringes of equal width, parallel to the viewing line). When the beam is diverging (or converging), the spherical waves interference pattern shows tilted parallel fringes. The fringes are parallel assuming other aberrations are very small. The tilt direction is a design parameter and is given by the manufacturer. The wavefront of the beam was then checked using a Shack-Hartmann wavefront sensor (SHWS), and was optimised such that the magnitude of each Zernike polynomial was $< 10\ nm$ (see Figure 6.2). The source was used once as a plane wave (with a collimating lens) and once as a point source (discussed later).

- **Lateral shift, tip/tilt, and defocus:** One of the cage system's shortcomings by design is its inability to accommodate for lateral shifts and tip/tilt corrections. The alignment starts with a well-collimated beam (i.e. almost zero tip/tilt), and propagates straight throughout the system. A small lateral shift is introduced when the light passes through the first beamsplitter, therefore, the second beamsplitter was mounted the other way around to correct for this lateral shift. Throughout the system, stationary lateral shifts, tip, and tilt were accounted for using the two mirrors outside the cage system. The vertical alignment was tested by allowing the light to propagate along the laboratory, and its height was verified to stay constant. The horizontal alignment was verified using a fixed remote target, and adding a

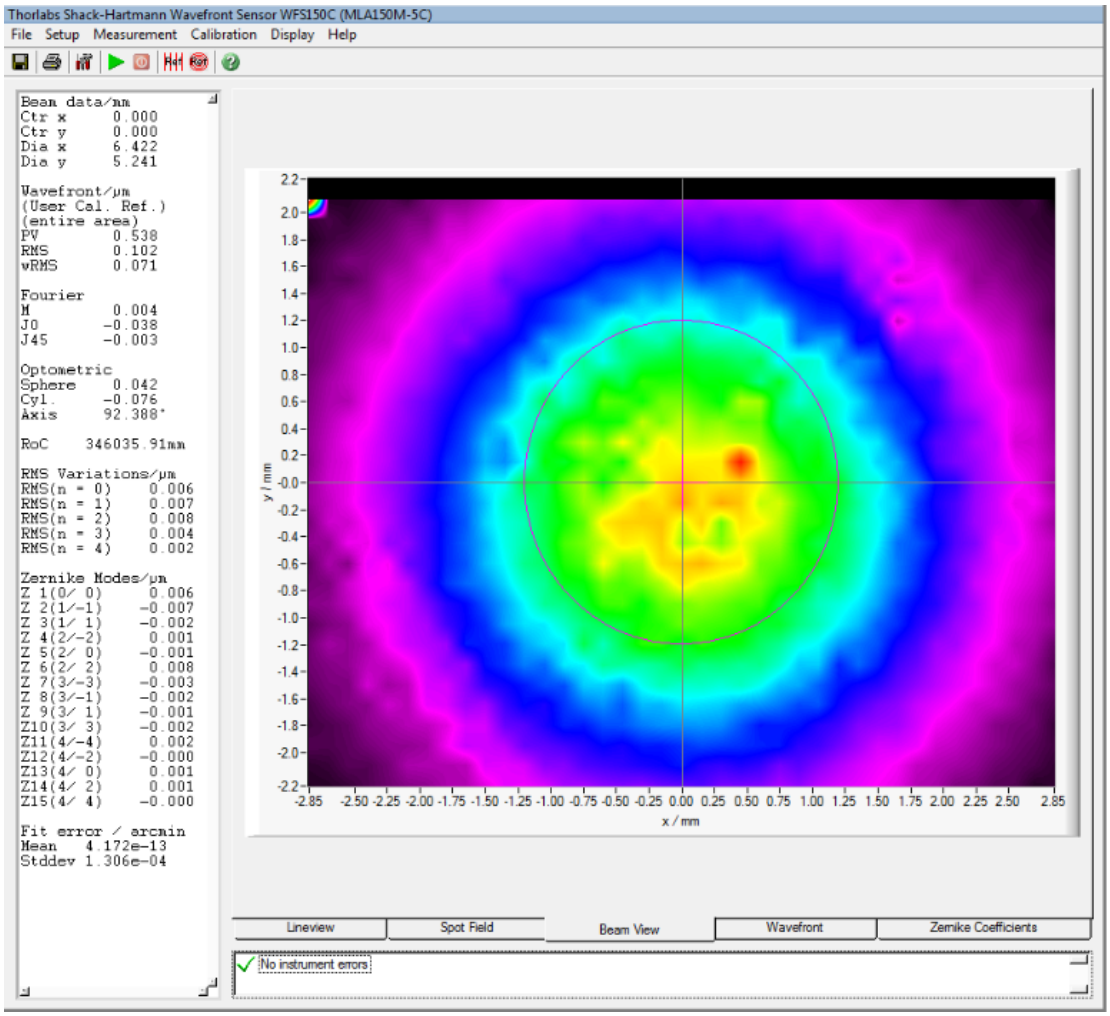

Fig. 6.2: Plane wave used to align and calibrate the system. Later confined using a 6 *mm* pupil.

single optical element at a time while maintaining spot position (while size varies) on the target. Two cage alignment targets were used throughout the cage parts of the system to ensure best alignment was achieved.

- **Pupil conjugate planes:** To ensure the minimal amount of error propagates through the system, the wavefront was measured in every pupil plane rather than just the start and end points. That was achieved using the shear plate and the SHWS. A plane wavefront has been measured at every pupil plane, at normal incidence, accounting for different pupil sizes. The system starts with a 6 mm beam diameter at the level of the eye's pupil, and is then 3.6 mm and 2.4 mm in the DM[1] and SHWS planes respectively.

  To test for conjugation in the illumination path (530 nm), the three LEDs were imaged in the eye's pupil plane. The assembly was modified until the sharpest image was achieved with their separation matching the theoretical prediction. To test for conjugation on the return path (from the eye to the SHWS), the alignment beam was used as a point source in the plane of the eye's pupil, and it was verified to converge to the smallest spot in the pupil conjugate planes.

- **Retinal conjugate planes:** Using the wavefront sensing LED without a pinhole as an extended source, a CCD camera was placed at every retinal conjugate plane to verify conjugation. Knowing the original emitter to be a square of sides 0.3 mm and the theoretical magnification of different sections of the system, the assembly was optimised to achieve a sharp image whose size matches the theoretical prediction in every retinal conjugate plane.

- **Pupil matching:** In pupil conjugate planes, it is important that the image of the entrance pupil falls at the exact position intended by design (in x and y coordinates). Therefore, the illumination LEDs were imaged in the pupil plane, through the entrance pupil to confirm correct alignment. A plane wave from the diode laser source was then placed at the entrance pupil, and the DM's surface was imaged to verify that the pupil is overlaid on the correct actuators (see Figure 6.3(a)). At the SHWS, the alignment process is more straight-forward as the device has a beam view showing which lenslets the beam passes through, and the beam centroid is calculated. The pupil

[1] The deformable mirror is positioned at a 22.5° angle of incidence with the beam in the design, yet the collimation was tested at normal incidence.

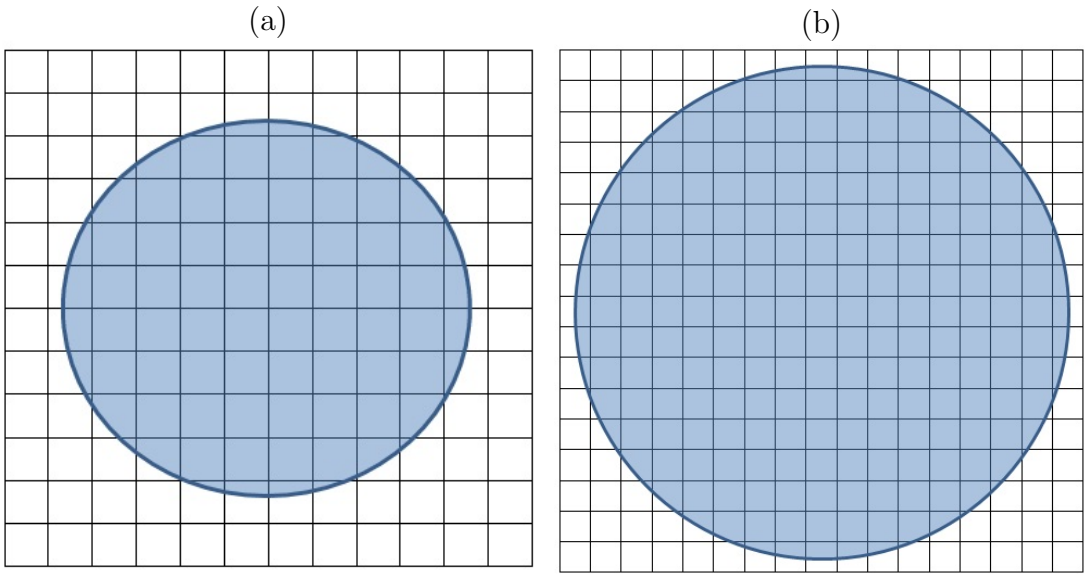

Fig. 6.3: (a) The elliptic pupil laid over the deformable mirror's actuator grid (actuator pitch = 450 μm), and (b) the circular pupil laid over the Shack-Hartmann lenslet array (lenslet pitch = 150 μm).

overlay at the SHWS lenslet array level is shown in Figure 6.3(b).

- **System calibration:** The last step of alignment is the calibration of system modes. The theory was discussed in section 3.4.3, and the practical steps taken to achieve that are discussed in detail in section 6.3.

6.2 Performance verification

For an optical system to have good performance, the aberrations at the end of each path (imaging and wavefront sensing arms in our case) should be minimised. This section discusses the steps taken to test the system performance using a model eye.

We start by testing the wavefront sensing arm. We start with a plane wave in the eye's pupil plane, and measure the wavefront error in the SHWS plane, having set the Badal optometer and the DM to their bias positions. This path's performance is defined by the RMS wavefront error and its corresponding Strehl ratio. The RMS error, as shown in Figure 6.4, is 21 nm; corresponding to a Strehl ratio of 0.95.

The next step was testing the imaging arm. This is achieved by imaging a point source positioned in the retinal plane. The PSF is shown in Figure 6.5. The Strehl ratio is given by [53]:

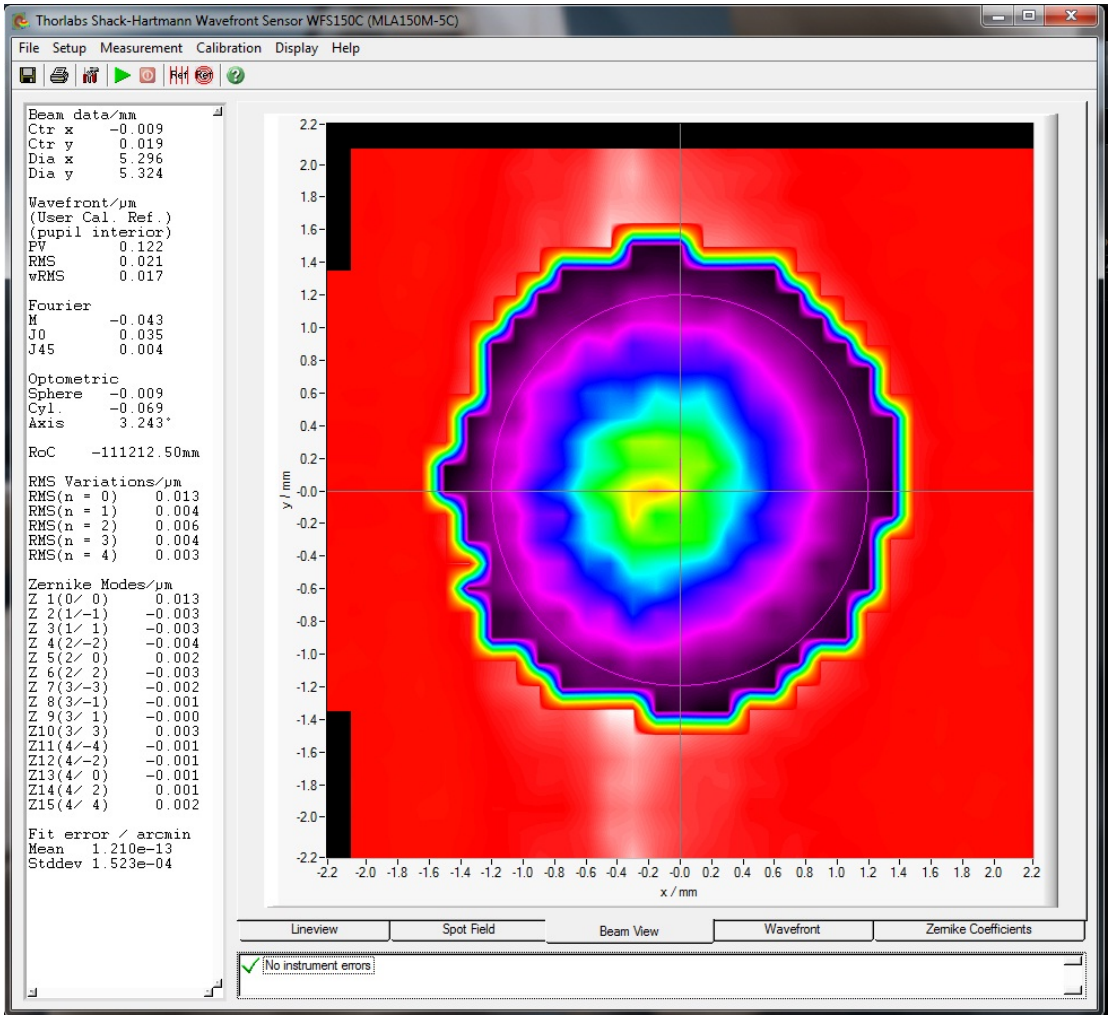

Fig. 6.4: System characterisation: wavefront measurement in the Shack-Hartmann wavefront sensor plane, used to verify the optical performance of the wavefront sensing arm.

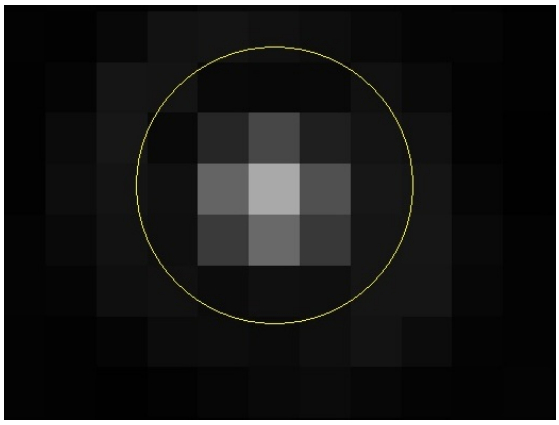

Fig. 6.5: System characterisation: point spread function at imaging CCD. The circle represents the theoretical Airy disc whose diameter is 4.34 pixels.

$$Strehl\ ratio = \frac{Intensity\ at\ peak\ (actual\ system)}{Intensity\ at\ peak\ (theoretical\ Airy\ disc)} \tag{6.1}$$

The Strehl ratio at the end of the imaging arm was 0.93. The actual and theoretical point spread functions are shown in Figure 6.6.

The adaptive optics correction loop was characterised using a model eye with a high fluctuating plane wavefront (highly fluctuating laser source, $> 80\ nm$ fluctuation). A residual RMS of $25 \pm 5\ nm$ was achieved under closed-loop operation. The loop runs at $8 \pm 1\ Hz$, limited by the lowest allowed exposure time for the SHWS. This correction level was achieved using the cubic equation modelling of the voltage (see Figures 6.7, 6.8), where the stroke-voltage matching is more realistic near the bias position. The repeatability of the system was tested using a model eye. The system was moved an re-aligned several times. After each iteration, a software code that acquires new phase maps, and creates a new influence function matrix was used to calibrate the DM-SHWS system. The new control matrix was plugged into the correction algorithm, and the same level of correction was achieved consistently.

6.3 System calibration

Several factors need to be taken into account to maximise the performance of a closed-loop system. Starting with a full characterisation of how the DM operates. The next step is modelling how the DM and the SHWS interact. Finally, the settings of the control system were optimised.

The first step is achieving the bias position for the DM. Unlike some DMs

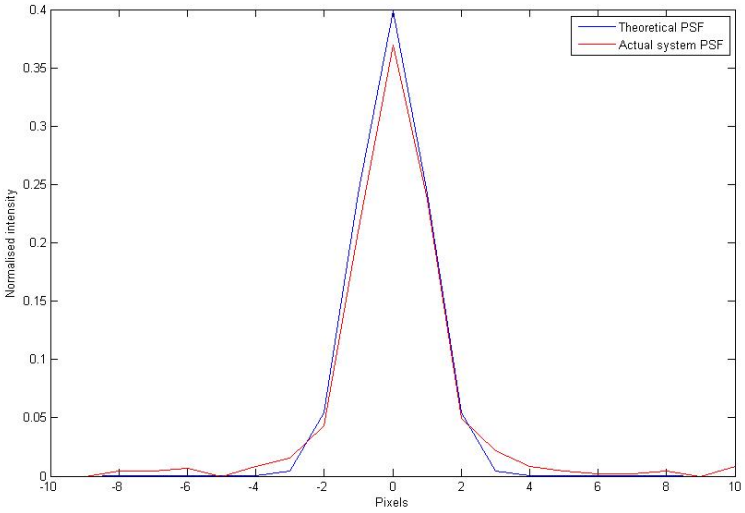

Fig. 6.6: System characterisation: Actual point spread function (red) compared to theoretical Airy disc (blue), used to calculate Strehl ratio at the imaging CCD.

(e.g. mirao 52-e) where it is straight-forward (bias position is at $0V$), the actuators of the BMC DM are fully contracted at $0V$. Furthermore, the relationship between stroke and applied voltage is not linear, and is different for different positioned actuators. This relationship has been characterised for each actuator (see Figures 6.7, 6.8), and the bias position was found at $167V$ (for the central four actuators), $174V$ (for all other actuators). Since the used DM has a continuous membrane, inter-actuator coupling was also taken into account (explained further in **Gain** below, see Figure 6.9). A cubic fit was found to best represent the relationship, and numerical solutions to the cubic equations were embedded into the code to translate stroke into voltage commands, to be sent to the DM controller.

The next step is characterising the system modes. After aligning the system, a computer programme automatically pushes and pulls each actuator to ± 0.5 of the maximum stroke. The phase maps are recorded (see Figure 6.10), and the influence function matrix is calculated as in section 3.4.3. In practice, the following factors need to be taken into account when calculating the pseudo-inverse and writing the correction algorithm:

- **Number of modes:** In section 3.4.3, matrix **W** is a diagonal matrix of size (140×140). The diagonal values represent the coefficients of the system modes whose spatial frequency increases with each row. When inverting this matrix, high frequency modes, which initially had very low coefficients, now

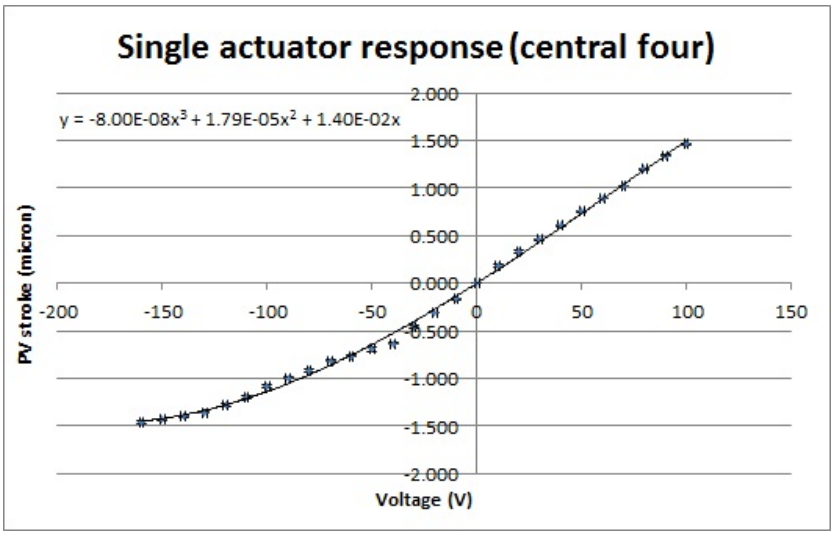

Fig. 6.7: Actuator peak-to-valley stroke as a function of applied voltage for the central actuators. The experiment was repeated many times, and produced consistent results, which led to the small error bars.

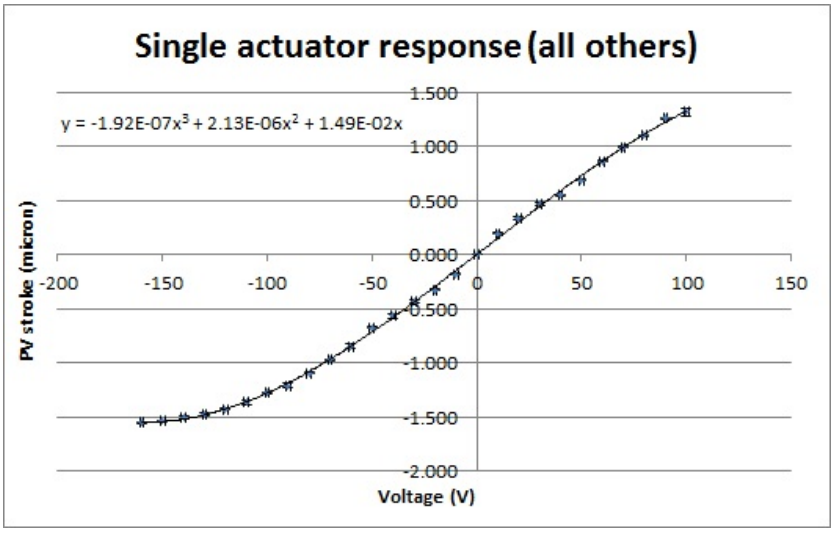

Fig. 6.8: Actuator peak-to-valley stroke as a function of applied voltage for all other actuators. The experiment was repeated many times, and produced consistent results, which led to the small error bars.

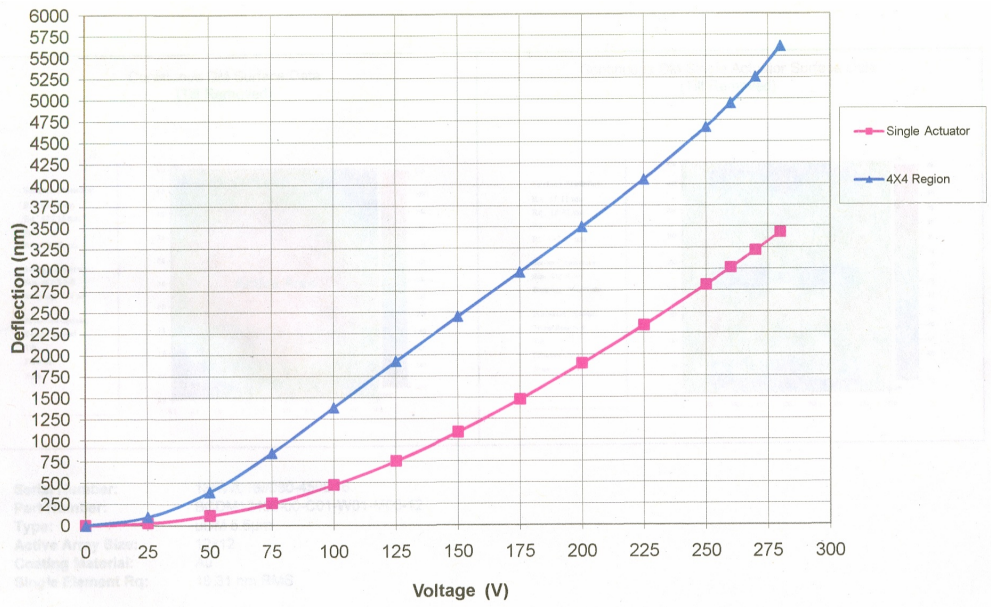

Fig. 6.9: System characterisation: deflection vs. voltage curves characterising deformable mirror inter-actuator coupling. [109]

have very high coefficients. However, these higher frequency modes become a source of noise, and typical DMs cannot correct for them. Their amplitudes become more abundant than the real signal. Therefore, the number of modes in **W** should be truncated to eliminate this source of noise, to a fixed number achieved empirically. In this setup, we are correcting for 25 system modes.

- **Removing tip/tilt:** Tip/tilt aberrations are less significant in vision-related applications as the eye positions itself to correct for that; however, beam wandering due to eye movements can create tip/tilt terms at the SHWS. Using a DM with limited stroke, correcting tip/tilt will saturate the DM, and impair its ability to perform the intended task. Hence, tip and tilt need not be accounted for. This is achieved in one of two ways:

  – Removing tip/tilt from the influence function matrix. This is done by removing average tip and tilt from the phase maps in the calibration phase. Since the modes in the matrix are orthogonal, the correction matrix becomes "blind" to tip/tilt terms.

  – Removing tip/tilt from the measured phase maps during closed-loop operation.

Due to microfluctuations of beam position at the lenslet array level, av-

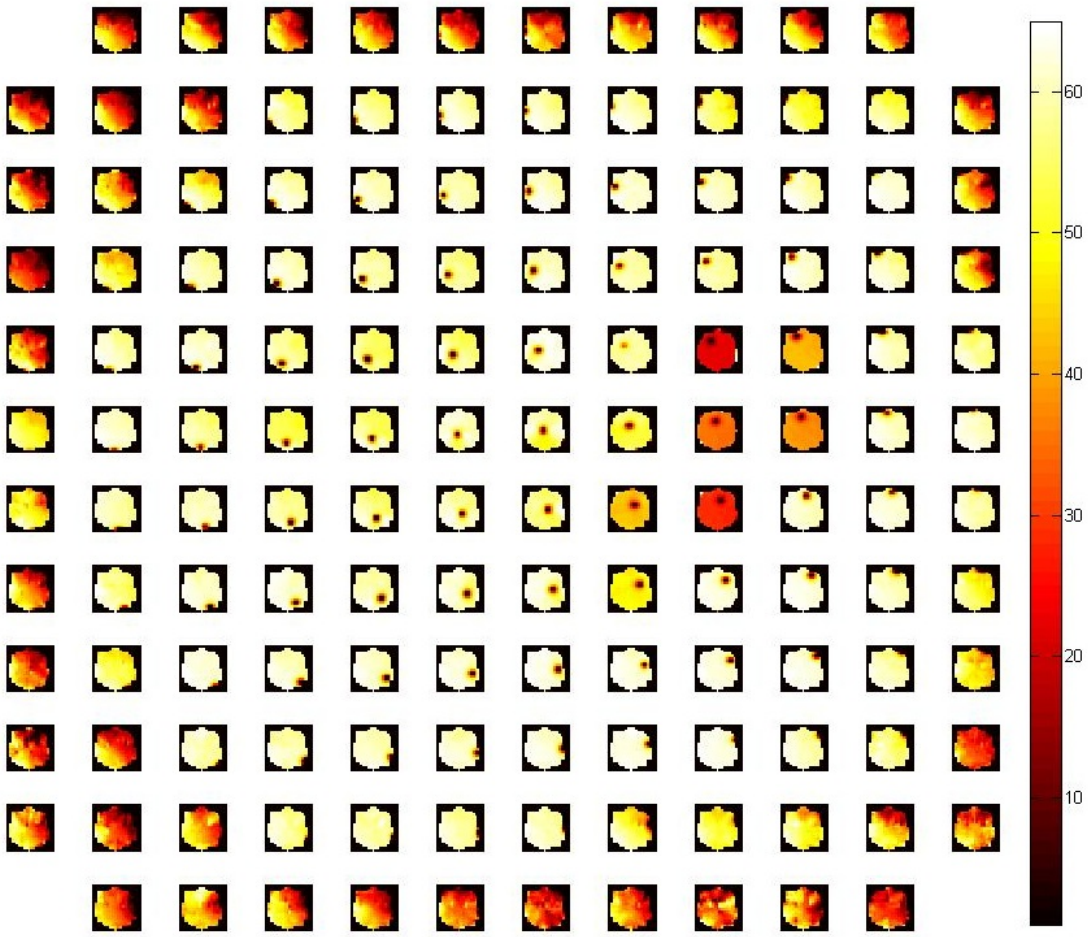

Fig. 6.10: Phase maps produced by poking actuators one at a time, used to calculate the influence function matrix. The scale on the right is in tens of nanometres.

erage tip/tilt could switch between high positive and high negative values when spots jump into their neighbouring search-blocks. Therefore, deleting average tip/tilt from each frame might alter the phase maps sent to the control algorithm. As a result, minor amounts of tip/tilt ($< 1\ \mu m$) were not removed from phase maps. Any values beyond that threshold were removed.

Tip/tilt can be removed before reconstructing phase, and new matrices of spot deviations are calculated as follows:

$$\begin{aligned} \mathbf{S}_{x1} &= \mathbf{S}_x - \bar{\mathbf{S}}_x \\ \mathbf{S}_{y1} &= \mathbf{S}_y - \bar{\mathbf{S}}_y \end{aligned} \tag{6.2}$$

where $\mathbf{S}_x$, $\mathbf{S}_y$ are the recorded deviation matrices in x and y, whose averages are $\bar{\mathbf{S}}_x$, $\bar{\mathbf{S}}_x$.

- **Gain:** In a closed-loop system, correction is achieved in several steps. A gain factor is introduced (< 1) to stop the DM from overshooting. In our case, this gain factor was used to account for inter-actuator coupling, too. Using the same driving voltage, four neighbouring actuators achieve a higher peak-to-valley stroke than a single actuator. Assuming a continuous phase map, this can be accounted for by lowering the gain factor. The optimum value for the gain factor in our setup (found empirically) is -0.3, where the negative sign comes from the sign notation used in the calibration step.

- **Missing data points:** During real eye measurements, missing data points are expected from the SHWS (e.g. if a point is out of the corresponding search-block, if the tear film starts to break up). In that case, our algorithm uses the value from the previous frame, in an assumption that the phase map at that location did not change much between frames. If the number of missing data points increases, or the system shows erratic behaviour, the DM is automatically restored to its bias position, and the correction algorithm starts over.

- **Defocus:** In section 4.1, we demonstrated that defocus needs to be corrected before the DM. The defocus term measured once at the beginning of the experiment is corrected for using a Badal optometer. The defocus term was still considered in the influence function matrix, so that the DM can

correct any residual defocus throughout the experiment.

7. SOFTWARE CONTROL ALGORITHMS

One major part of an adaptive optics system is the controller. This chapter describes the algorithms used to calibrate and control the adaptive optics retinal imaging system, and the software used to acquire images. The Labview block diagrams can be found in Appendix C.

7.1 Deformable mirror - Shack-Hartmann system calibration

The DM-SHWS system has to be recalibrated every time an alignment adjustment has been made. Therefore, it is impractical to do the calibration manually. Two separate Labview virtual instruments[1] (VI's) were designed. The first acquires phase maps, while the second uses those phase maps to build the control matrix $\mathbf{M}^{+}$.

7.1.1 Acquisition of phase maps

The algorithm for this VI is shown in Figure 7.1. The algorithm takes the settings set by the user in the graphical user interface (GUI, shown in Figure 7.2), pokes each actuator to previously stored voltages corresponding to ± 0.5 of the maximum actuator displacement, and records their corresponding phase maps. The algorithm yields 280 comma-separated-variables (*.csv) files, representing the phase maps of the 140 actuator in the positive and negative directions.

The acquisition time is less than five minutes. It is reasonable compared to a few hours of manual acquisition, and eliminates human errors. Two points are vital to achieve accurate calibration; the system must be well-aligned prior to the calibration, and a very low fluctuation light source with low ambient noise must be used.

[1] Programmes and functions in Labview are referred to as VI's and sub-VI's.

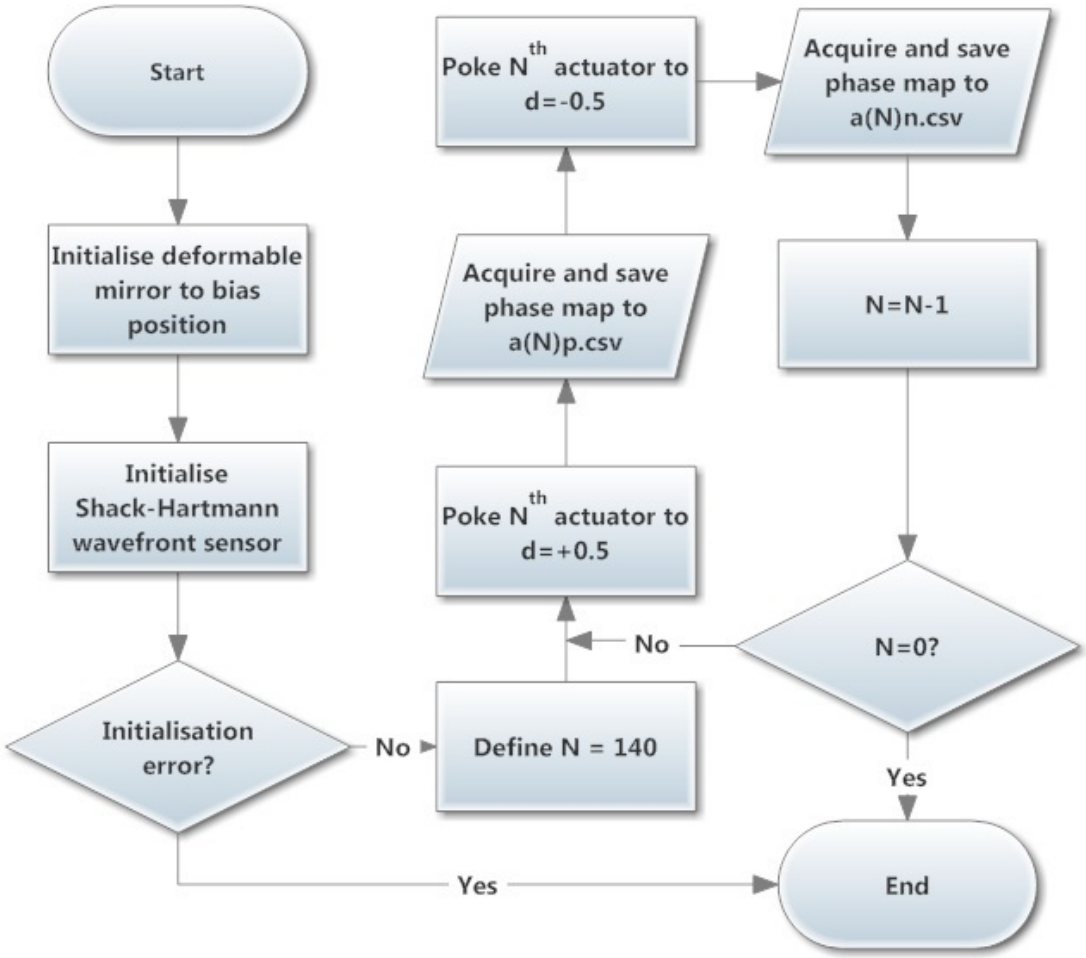

Fig. 7.1: Flowchart representing the algorithm used to acquire phase maps, used to calibrate the adaptive optics system and build the control matrix later.

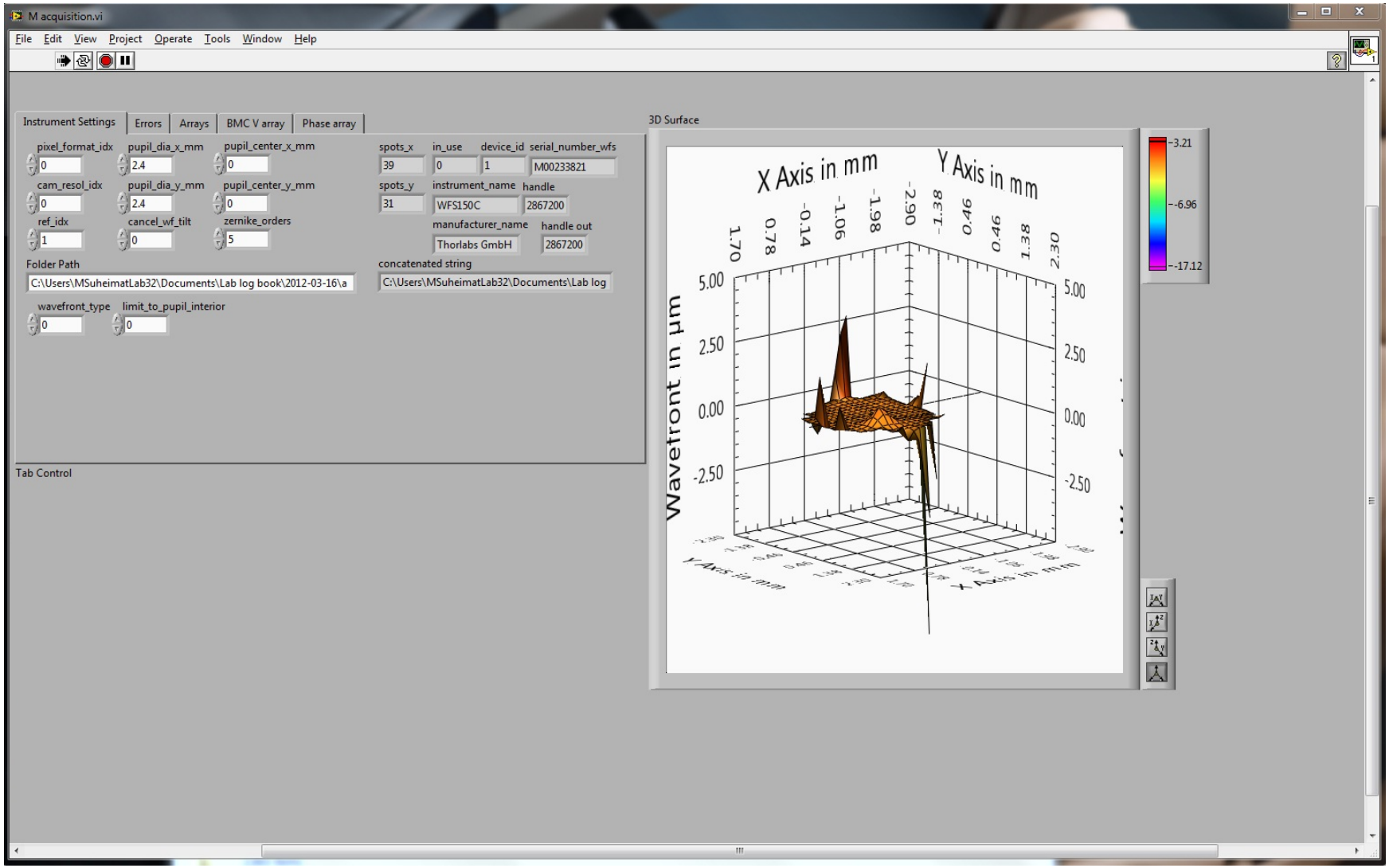

Fig. 7.2: GUI of the phase maps acquisition Labview VI. These settings are considered in the code. The 3D graph on the right shows phase maps during acquisition, which is monitored to ensure there is no systematic error while the acquisition is running. The spikes in the figure are outside the defined pupil and are cut off later during processing.

7.1.2 Building the control matrix

The algorithm for this VI is shown in Figure 7.3. It reads the 280 phase maps acquired using the previous algorithm, computes a normalised vector representing each actuator. The pupil at the Shack-Hartmann wavefront sensor level is then overlaid on that vector. The resulting vectors are gathered in a 197×140 influence function matrix $\mathbf{M}$ (where 197 is the number of spots inside the pupil, and 140 is the number of actuators.). $\mathbf{M}^+$, the pseudo-inverse of $\mathbf{M}$, is then computed and saved to be used as input for the adaptive optics correction algorithm (the theory is explained in section 3.4.3).

The main setting this algorithm considers is the number of system modes to include in the calculation of $\mathbf{M}^+$. Higher frequency mode coefficients are very small ($< 1\%$) compared to lower frequency mode coefficients. When inverted, they become very large, and their influence causes the adaptive optics loop to diverge. The set number determines the number of singular values that are retained in $\mathbf{W}$. The rest are set to zero.

7.2 Adaptive optics closed-loop control

This is the main virtual instrument (VI) which controls the adaptive optics closed-loop operation. The algorithm for this VI is shown in Figure 7.4. This algorithm imports the control matrix achieved by the algorithm described in section 7.1.2. It then sets the deformable mirror to the bias position and acquires phase maps. Some real-time processing helps achieve the best correction. Some operations are built-in as they are essential (e.g. pupil superposition, missing spots management) while other operations are optional (e.g. removing tip/tilt, wavefront type). The processed phase map is then multiplied by $\mathbf{M}^+$ on the left, and by the gain factor. The result is then the new displacement increments, which are added to the previous displacement matrix, converted into a voltage map, and sent to the deformable mirror driver.

The graphical user interface (GUI) is shown in Figure 7.5. The first tab has the instrument settings (see below) and operation warnings and read-outs. The second tab contains any errors produced by the DM or SHWS drivers. The third tab shows any intermediate stage arrays, and has been useful through the fine-tuning of the algorithm. The fourth tab shows an array of the phase map, displayed graphically below in the left window. The last tab shows an array of DM voltages sent to the DM, and displayed below in the right window. The top right

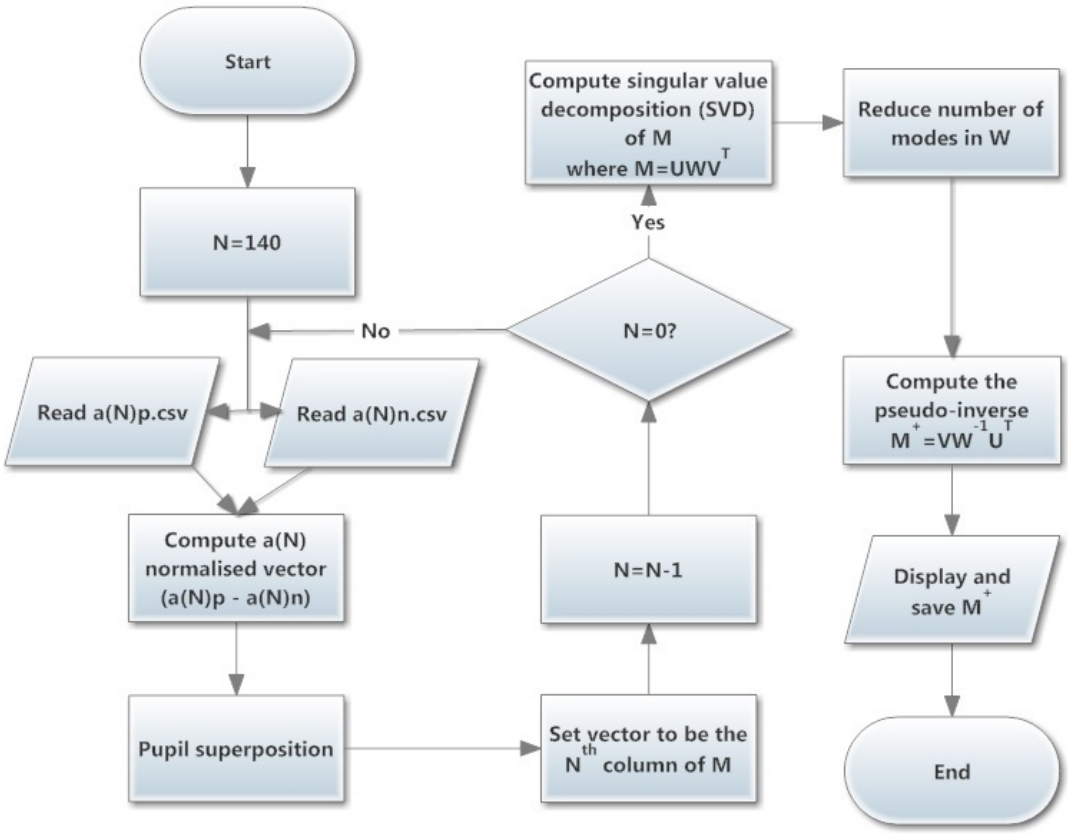

Fig. 7.3: Flowchart representing the algorithm used to calculate the adaptive optics control matrix.

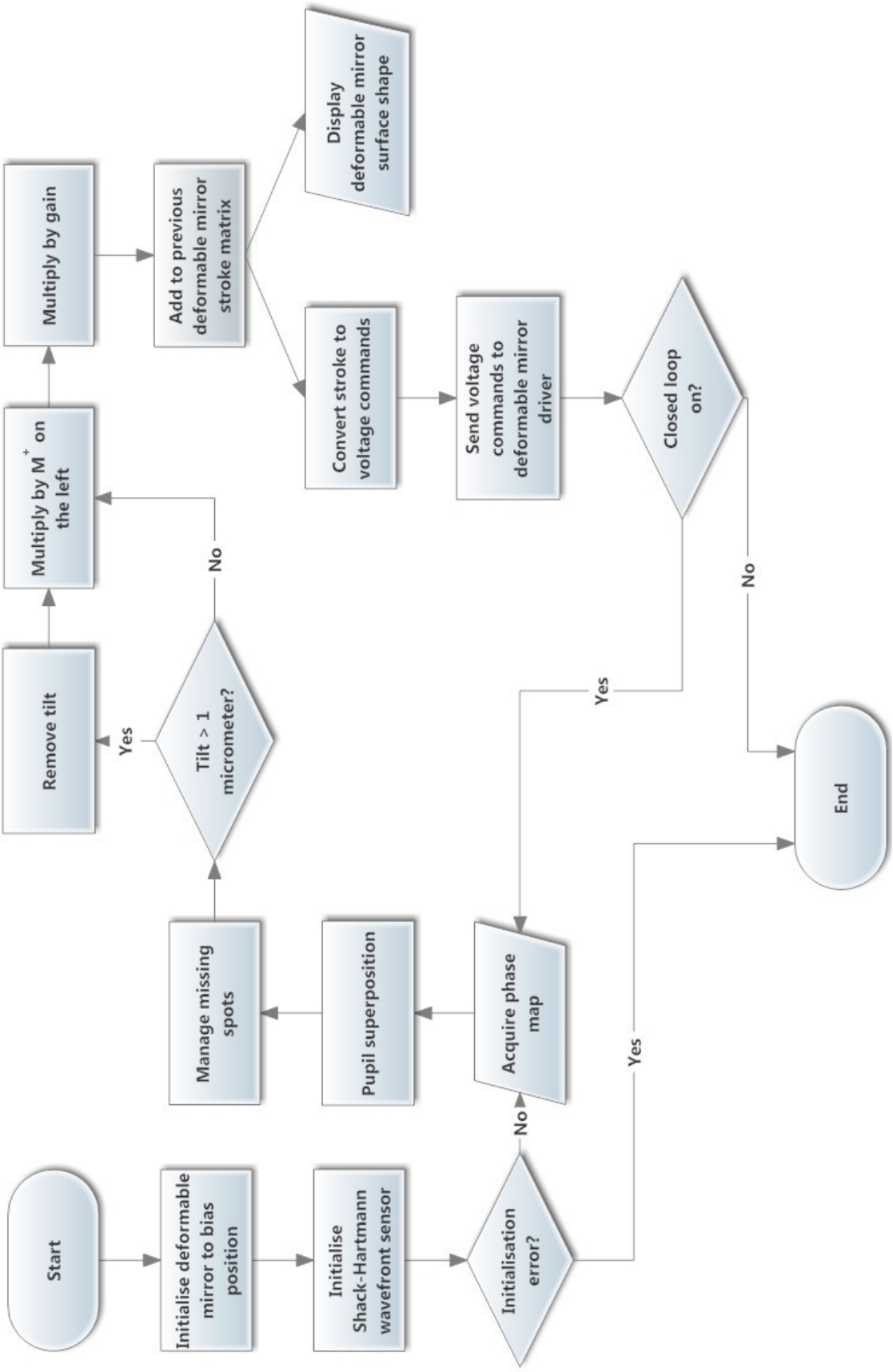

Fig. 7.4: Flowchart representing the algorithm used to control the adaptive optics loop.

box controls the translational stage therefore changing the vergence of the Badal optometer. The following is a list of command buttons, controls, and indicators included in this GUI. The ones not described here are straight-forward.

- **Command buttons:**
  - **Bias** This button restores the DM to its bias position by sending a position array of zeros to the DM driver.
  - **Plot mirror?** Since running two 3D plots simultaneously in a Labview VI slows down the loop time, the DM surface map is only plotted once when this button is clicked.
  - **AO loop** This button starts and stops the adaptive optics closed-loop operation. It is required for some other buttons to function (such as **Bias**). Stopping the loop using this command button pauses the loop, and maintains the current DM surface map (i.e. open-loop correction).
  - **STOP** This button performs a soft-stop operation on the VI. It should only be used after the **AO loop** button has been stopped. In contrast to the built-in stop button in Labview which crashes the code, this button allows the current sequence to finish, closes devices drivers, releases locked instruments, and achieves a safe stop.
- **LED indicators:**
  - **Ready** Since the initialisation stage of the algorithm requires some time to run, this LED turns on to indicate that the system is ready for AO loop correction to start. Starting the AO loop before this light turns on will produce an error.
  - **Power too high** This LED indicates that the light level at the SHWS camera is too high. The system will continue to operate, but the centroiding will be less accurate due to saturation of some pixels.
  - **Power too low** This LED indicates that the light level reaching the SHWS camera is too low, and is not (or barely) sufficient to achieve a phase map. The system will set the DM to its bias position in an attempt to restore light levels. If that does not work, then the system should be modified to deliver a higher light level.

- **High ambient level** This LED indicates that the signal-to-noise ratio has dropped at the SHWS camera. Ambient light sources should be blocked to achieve a more accurate phase reading.

- **Controls:**
  - `pixel_format_index:` This control sets the SHWS camera binning. Default value = 0 corresponding to 1×1 binning.
  - `cam_resol_idx:` This control sets the SWHS resolution. Default value = 0 corresponding to 1.3 megapixels.
  - `ref_idx` This control sets the SHWS to use the built-in calibrated wavefront reference (0) or the user calibrated wavefront reference (1 - default value).
  - `pupil_dia_x_mm` and `pupil_dia_y_mm:` These two controls define the beam diameter in x and y respectively. The default value for both is 2.4 mm corresponding to a 6 mm eye pupil.
  - `pupil_center_x_mm` and `pupil_center_y_mm:` These two controls define the beam center in x and y. These should be always set to their default values (0) as the DM-SHWS system is calibrated for that pupil position.
  - `wavefront_type` and `ArrayZernikeReconstruct:` The first control can be set to one of three values, depending on the wavefront type to be corrected for:
    - 0 : measured wavefront (default value)
    - 1 : reconstructed wavefront
    - 2 : residual wavefront

    The Zernike modes to be reconstructed are chosen from the second control, where setting a value of (1) next to a Zernike mode includes that mode in the reconstruction.
  - `limit_to_pupil_interior:` When set to (1), this control limits wavefront calculations (such as residual RMS) to the defined pupil. Default value = 0.
  - `Gain:` This control defines the correction loop gain, further explained in section 6.3.

  - `cancel_wf_tilt:` Setting this control to (1) removes wavefront tip/tilt from the phase map as an initial condition. Default value = 0.
  - `Max tilt:` This control sets the maximum allowed tip/tilt values before the system is automatically set to remove them from the wavefront in μm. Default value = 2.
  - `WFS gain:` This control defines the gain of the SHWS camera.
  - `WFS exposure time:` This control sets the SHWS camera's exposure time in seconds.

- **Indicators:**
  - `ArrayZernikeOrdersRms_um:` This indicator is an array of residual RMS (in μm) for each Zernike order.
  - `Residual RMS_um:` This indicator displays the residual RMS (in μm) calculated from the phase map in real time.
  - `WFS gain out:` This indicators displays the real SHWS camera gain value achieved in practice.
  - `WFS exposure time out:` This indicator displays the real exposure time used by the SHWS camera.
  - `correction rate:` This indicator displays the rate (in Hz) at which the adaptive optics loop is running.

The best practice to run this VI could be achieved using the following sequence:

1. Maintain all default values.
2. Turn on a reference laser.
3. Run the Labview VI, and wait until the **Ready** LED turns on.
4. Click the **AO loop** command button. At this stage, the wavefront sensing is turned on, but correction is not started yet.
5. Align the subject's pupil with the SHWS.
6. Click the **Bias** command button to start wavefront correction.
7. Adjust settings as necessary.

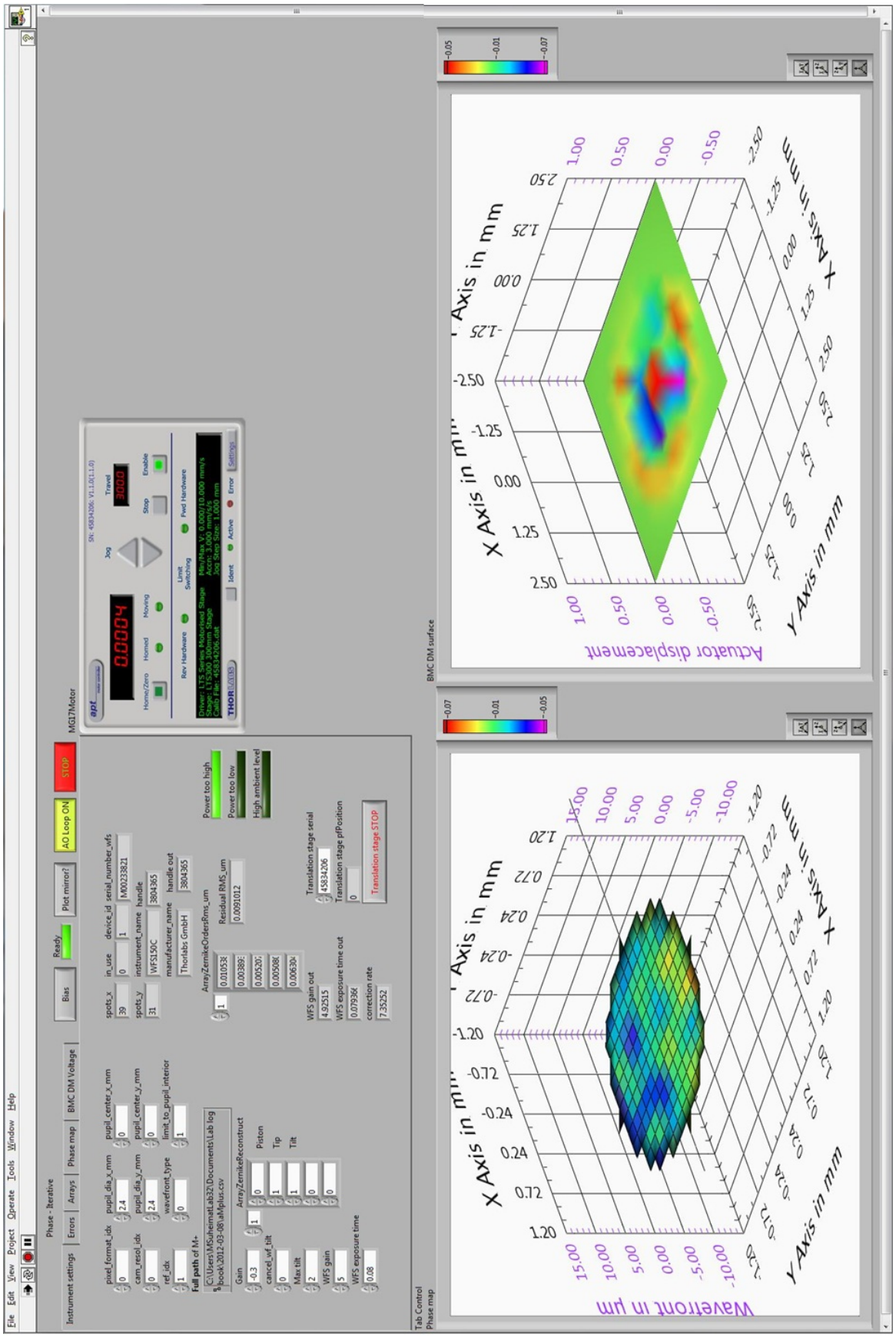

Fig. 7.5: GUI of the adaptive optics closed-loop correction Labview VI. These settings are considered in the code. The 3D graph on the left shows phase maps during acquisition, while the 3D graph on the right shows the deformable mirror's surface when requested.

7.3 Retinal image acquisition control

A Labview VI has been initially created to control the imaging camera. Further investigation led to the conclusion that more control over the camera can be achieved using the separately purchased QCapture Pro software, designed by the manufacturer of the camera. This is because the Labview driver is limited, and does not give enough control over the camera.

Images were acquired using the following sequence:

1. Turn both light sources on, while the subject is not aligned, and acquire a dark background frame.
2. Align the subject.
3. Turn the imaging source off, and acquire another background frame with the wavefront source turned on.
4. Turn the imaging source on.
5. Acquire a sequence of 30 frames.
6. Turn light sources off.
7. Ask the subject to relax.
8. Frames post-processing, including the subtraction of background frames and image enhancement.

8. RETINAL IMAGES

The proposed adaptive optics retinal imaging system was built as a proof-of-concept. Once the system became functional, stacks of thirty images at different layers of the retina were acquired from the right eyes of four subjects (young healthy eyes, defocus values of $-1.5 - 0\ D$ with an average of $-0.5\ D$). Their defocus was corrected using the Badal optometer, and then the adaptive optics loop was used to correct all other aberrations. The residual RMS of wavefront aberrations after defocus correction (using the Badal) was $0.95{-}1.20\ \mu m$, and after adaptive optics correction was $0.038 - 0.052\ \mu m$, good correction. The subject looks at the wavefront sensing LED as a fixation target. Their ability to fixate was considered an indication to how rested they were during the acquisition of the images. Minor movements did not affect the image quality since the correction was based on local tilts, and did not depend on the full phase map. However, the residual RMS value, which is calculated over the full pupil will have risen due to such minor movements. Major movements and blinks produced unusable images, and therefore the principle of lucky imaging was used. The researcher looks at the full sequence of thirty images, and chooses the usable images based on visual analysis. Consistent imaging quality was achieved with the four different subjects and at different eccentricities. This chapter shows the level of detail achieved with the built instrument, and argues that the structure shown on the retina is in fact photoreceptors, not speckle or artefacts.

A few sample images of different eyes at different eccentricities are shown in Figures 8.1, 8.2, and 8.3. The images show high contrast blood vessels and a fine repeating structure with slightly varying size. The high contrast of the blood vessels is due to the fact that a green ($\lambda = 530\ nm$) source was used as an illumination source [110]. Therefore, these images could be used for highly defined edge detection of blood vessels. As for the photoreceptors, better contrast of every type of photoreceptors ($S,\ L,\ M$ cones) has been achieved by bleaching the photoreceptors at different wavelengths [33].

Some basic image processing techniques were used for display purposes. First,

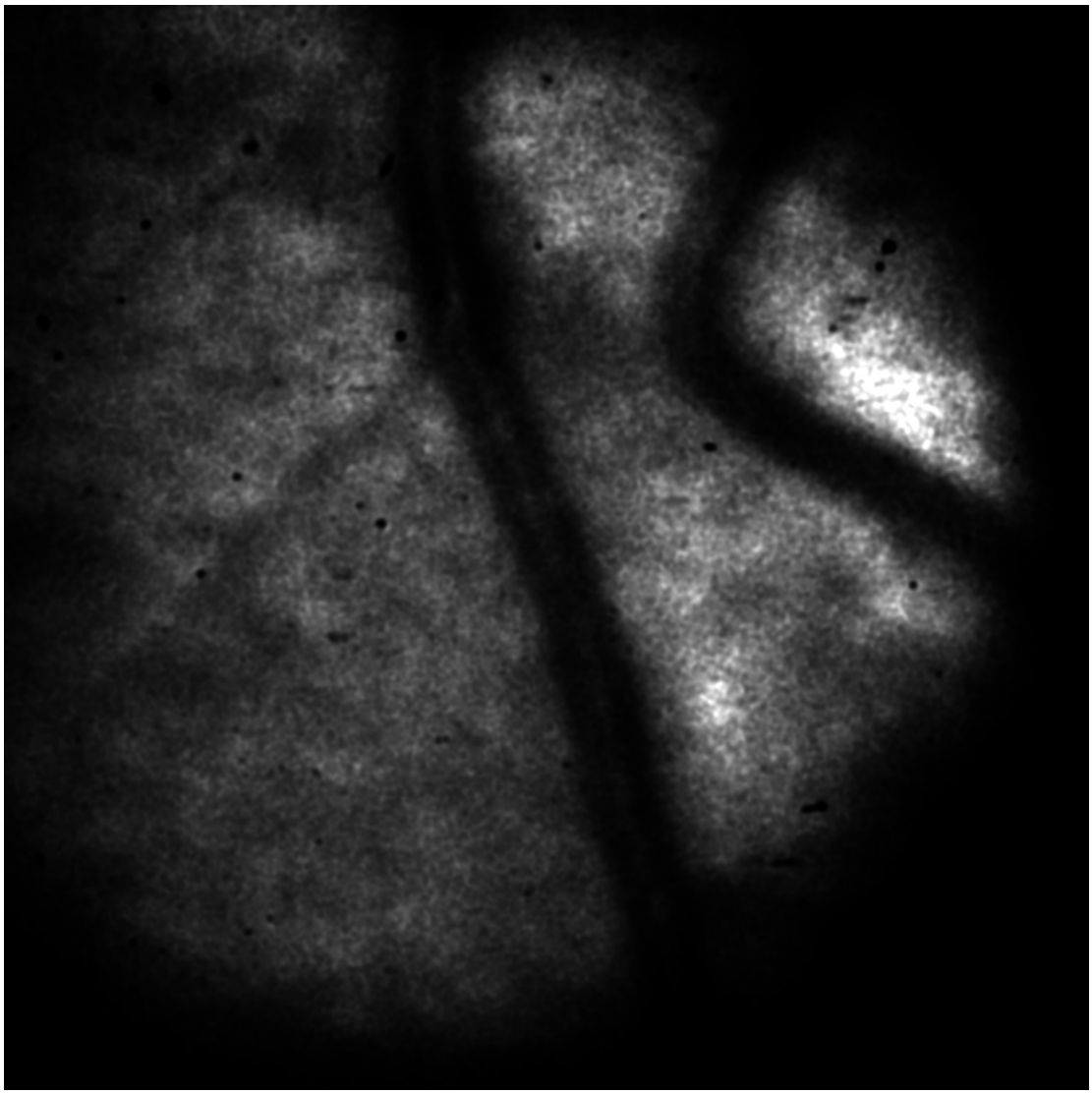

Fig. 8.1: A 4° field-of-view sample retinal image (subject OM, right eye, centred at 4° temporal, 6° inferior) showing high contrast blood vessels, lower contrast capillaries, and the cone mosaic.

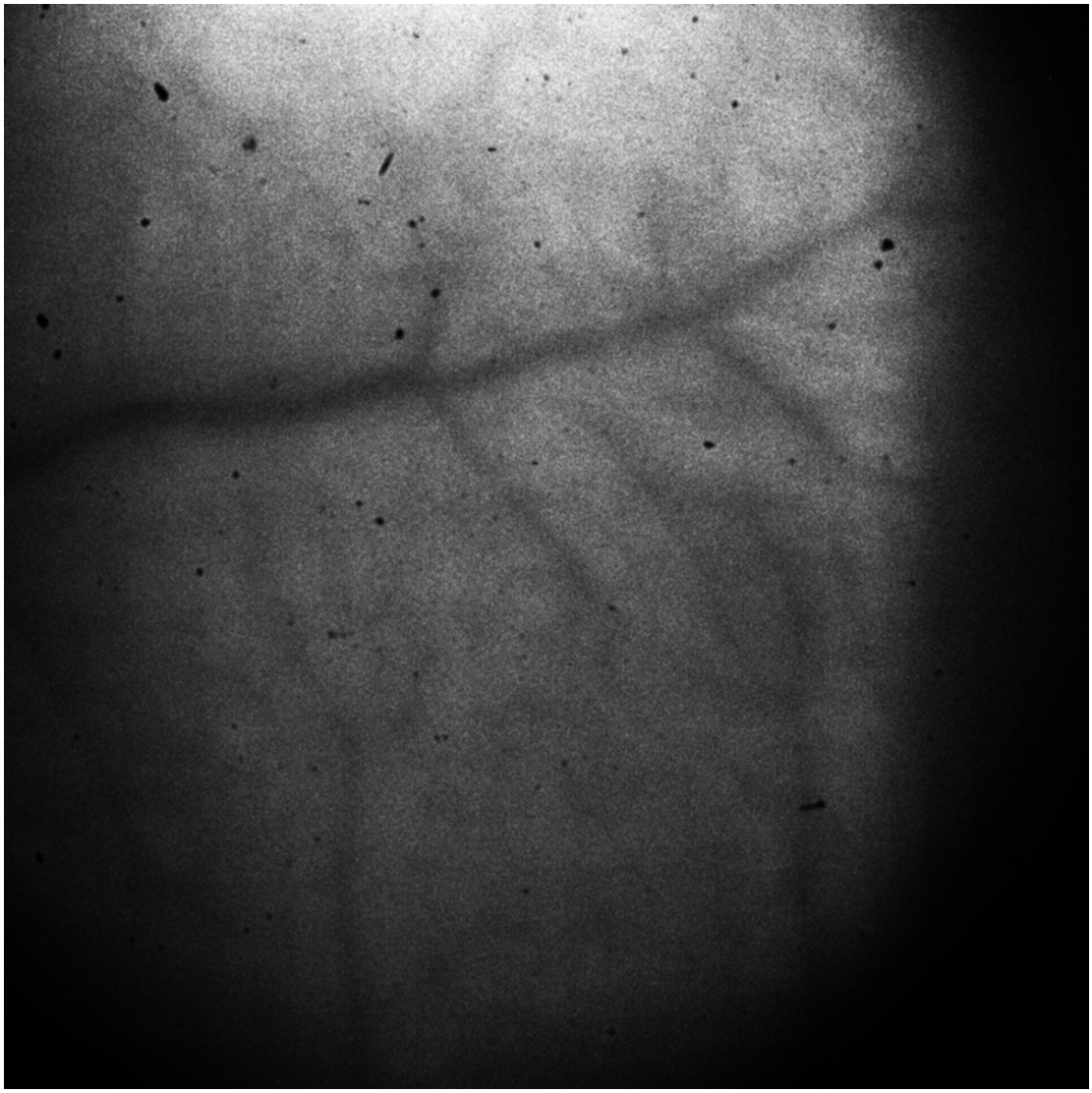

Fig. 8.2: A 4° field-of-view sample retinal image (subject SM, right eye, centred at 4° nasal)

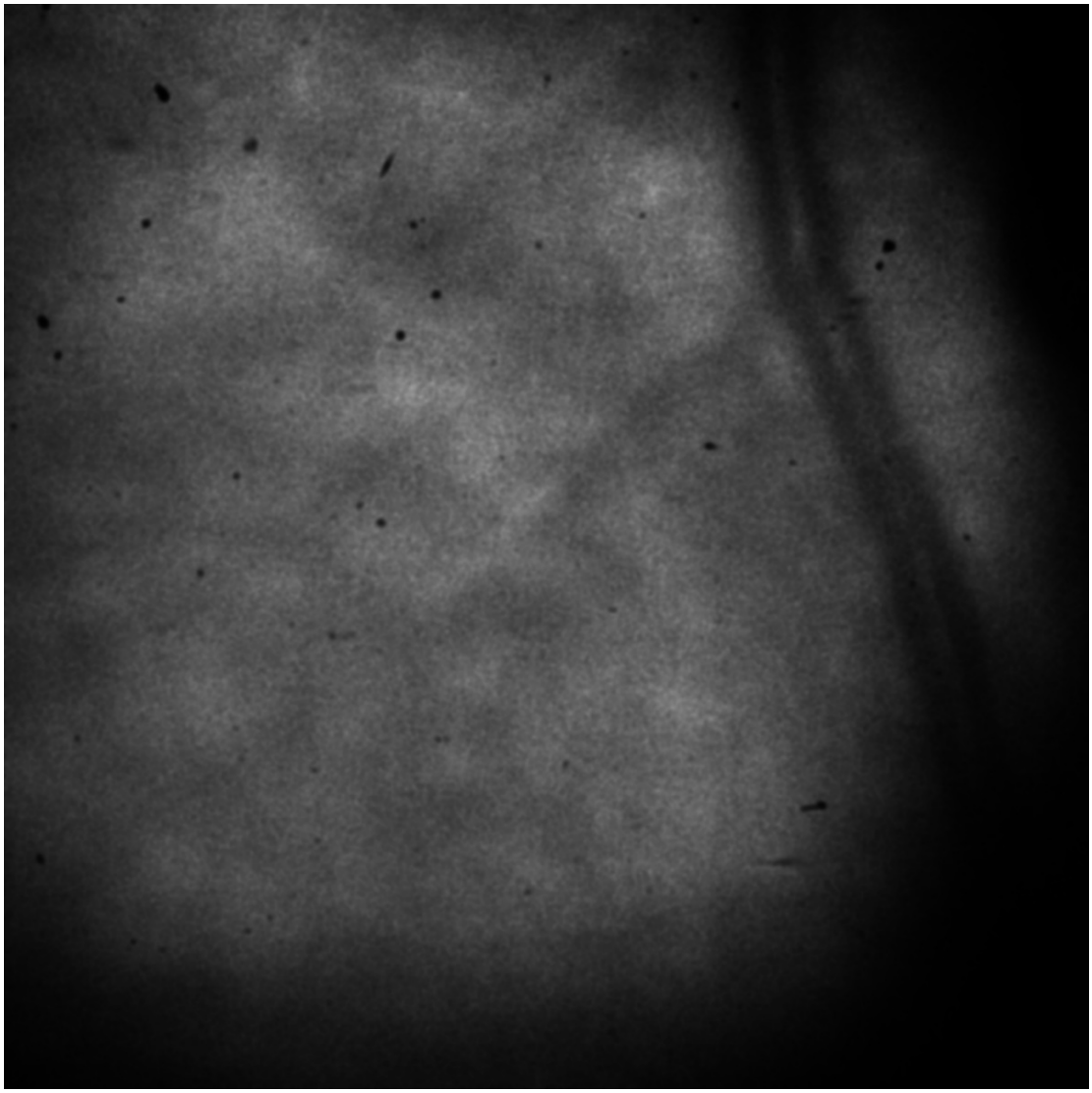

Fig. 8.3: A 4° field-of-view sample retinal image (subject OM, right eye, centred at 5° temporal, 7° inferior)

a Gaussian blur was introduced to get rid of random noise in the image. A Gaussian function whose full-width-at-half-maximum is 2 pixels was used to filter the image [111], and then the brightness and contrast were adjusted. To improve the image quality even further, more advanced post-processing techniques could be used. For instance, the retinal imaging system explained here acquires stacks of thirty frames. Image registration could be used to increase the signal-to-noise ratio where the different frames of the same sequence are lined up on top of each other and pixel values are averaged. The registration process involved moving one frame at a time over a reference frame, and calculating the correlation values. The highest correlation value, in principle, corresponds to the lined up position. However, only portions of the image who are clear of blood vessels should be used here. Since blood vessels lie in a different layer on the retina, performing image registration in reference to blood vessels will blur out the photoreceptors.

The objective of this project was to build a proof-of-concept for a low cost retinal imaging system, which can be used for the early detection of progressive diseases. The contrast of the acquired images was sufficient for image processing techniques for edge and feature detection. For instance, for the early detection of glaucoma, imaging the optic nerve and keeping track of the cup-to-disc ratio will assist in the detection and provide a good estimate of how fast the disease is progressing [36]. For the early detection and progress monitoring of age-related macular degeneration (AMD), a high resolution image that shows high reflectivities of photoreceptors is preferable, as it supplies enough contrast for automatic image processing algorithms to distinguish photoreceptors from the patches which cover them. As a first step towards this objective, the acquired images had to have clear photoreceptors in them. The images obtained with the retinal imaging system had fine structure in them, but a multi-step procedure had to be followed to identify the nature of those features:

- The power spectra of different frames within the same image sequence were computed and compared (see Figure 8.4). The figure shows a consistent frequency content of several images at the same location of a retina, which does not change with time. It has a wide peak corresponding to a quasi-periodic structure whose mean size is 3.25 μm. The one-dimensional power spectra in Figure 8.4 represent rotational averages over all possible angles of their corresponding two-dimensional power spectra (such as the one shown in Figure 8.5). The peak is wide because the image extends over a 4° field-of-view, where the cone sizes vary between $2.5 - 6.0$ μm in size (see

Figure 8.6). The vertical and horizontal streaks which appear in the two-dimensional power spectrum and their corresponding spikes that appear in the one-dimensional power spectra are artefacts due to the boundaries of the processed image [112].

- The power spectra of different frames acquired from two different subjects at different eccentricities were computed and compared (see Figure 8.7). The figure shows different broad peaks corresponding to different distributions of the fine structure on the retina. The mathematical mean of those peaks depicted a slight shift in position corresponding to the variation of cone sizes at different eccentricities in the retina.

- The power spectra of images without any correction, with defocus correction (Badal), and with full adaptive optics correction were compared (see Figure 8.7). The image without correction appears to be flat since it does not contain any information about the fine structure. Defocus correction shows some of the comparatively larger structure ($> 3.5\ \mu m$) while the curve drops faster since finer structures cannot be resolved. Adaptive optics corrected images show a higher content of the fine structure (i.e. higher resolution).

- The resolution limit of the built retinal imaging system could be quantified using the cut-off frequency shown in the power spectra figures, which in this case was 0.679 $cycles/\mu m$. This corresponds to a smallest feature size of 1.47 μm. This is a theoretical limit, which could be increased using a shorter wavelength; however, the human retina has a lower damage threshold at shorter wavelengths.

The procedure above was followed to ensure that the fine structure in the images has the statistical characteristics of photoreceptors. It differs from speckle in that it does not have time dependence, it is consistent for each retinal position, and it changes when changing positions. The analysis proves that the structure is not due to a systematic artefact or post-processing algorithms; as if it was, the structure pattern (and therefore its power spectrum) should not vary with different imaging positions.

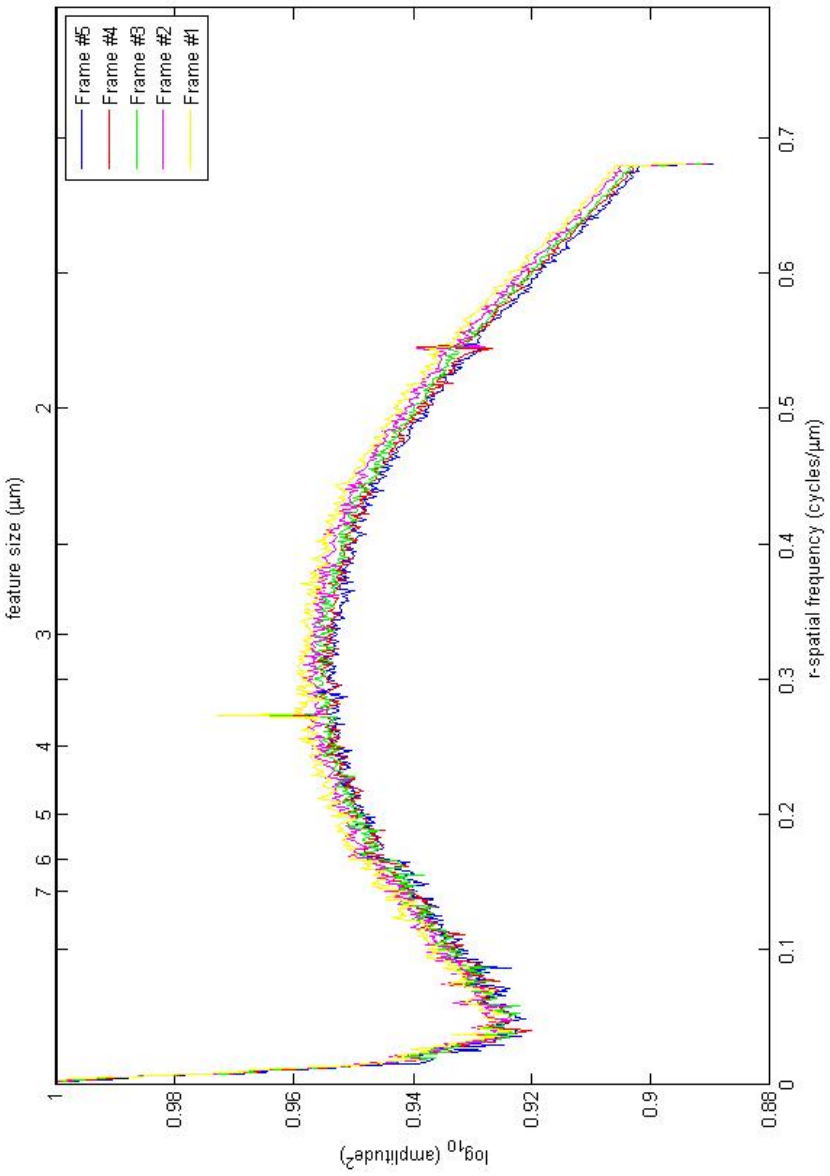

Fig. 8.4: Power spectra of five frames from the same image sequence, representing consistent frequency content with a peak whose mean correspond to a feature size of 3.25 μm.

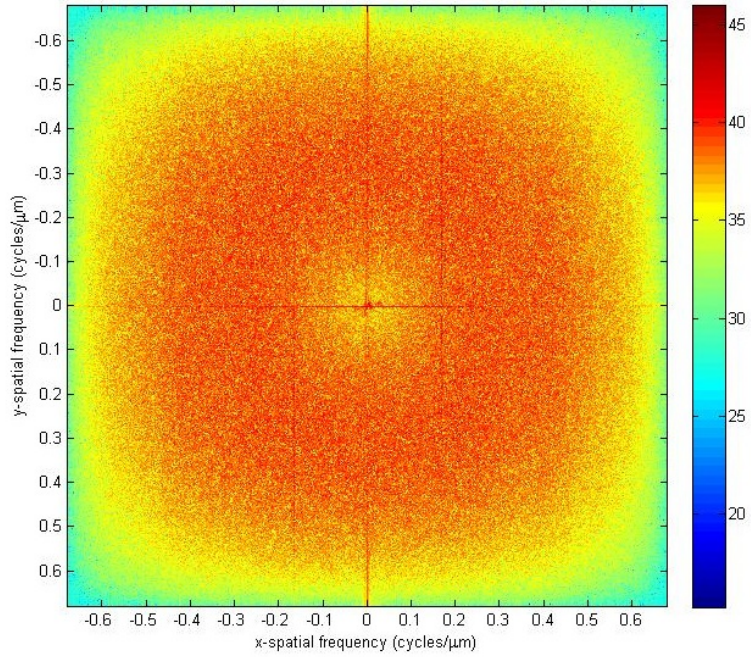

Fig. 8.5: A two-dimensional power spectrum of Figure 8.1 showing a wide peak over all angles corresponding to a mean feature size of 3.25 μm. Note the arefacts near ± 0.2 $cycles/\mu m$ which are discussed in the text.

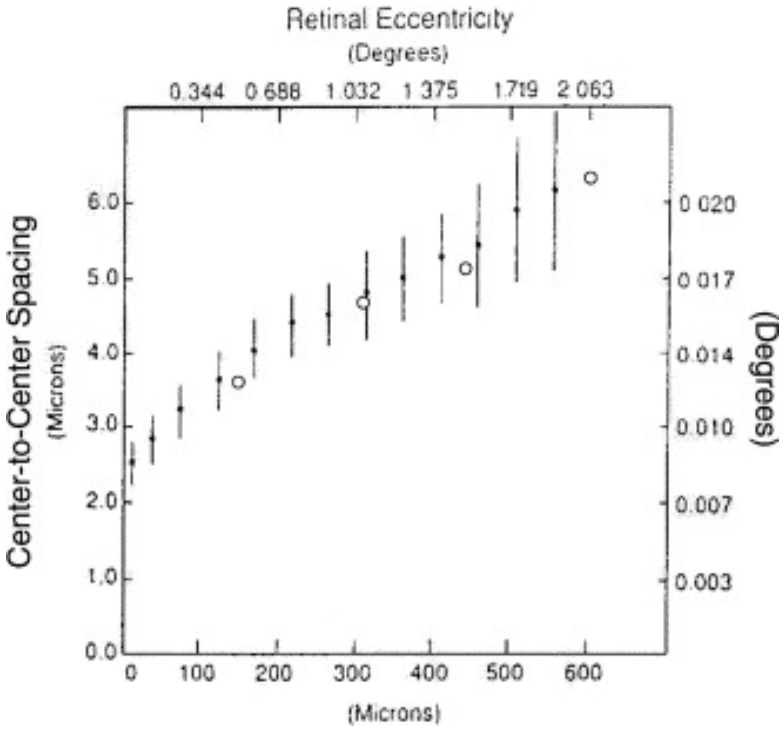

Fig. 8.6: Center-to-center cone spacing versus eccentricity. Circles (∘) are measurements from [113], dots (.) are measurements from [114].

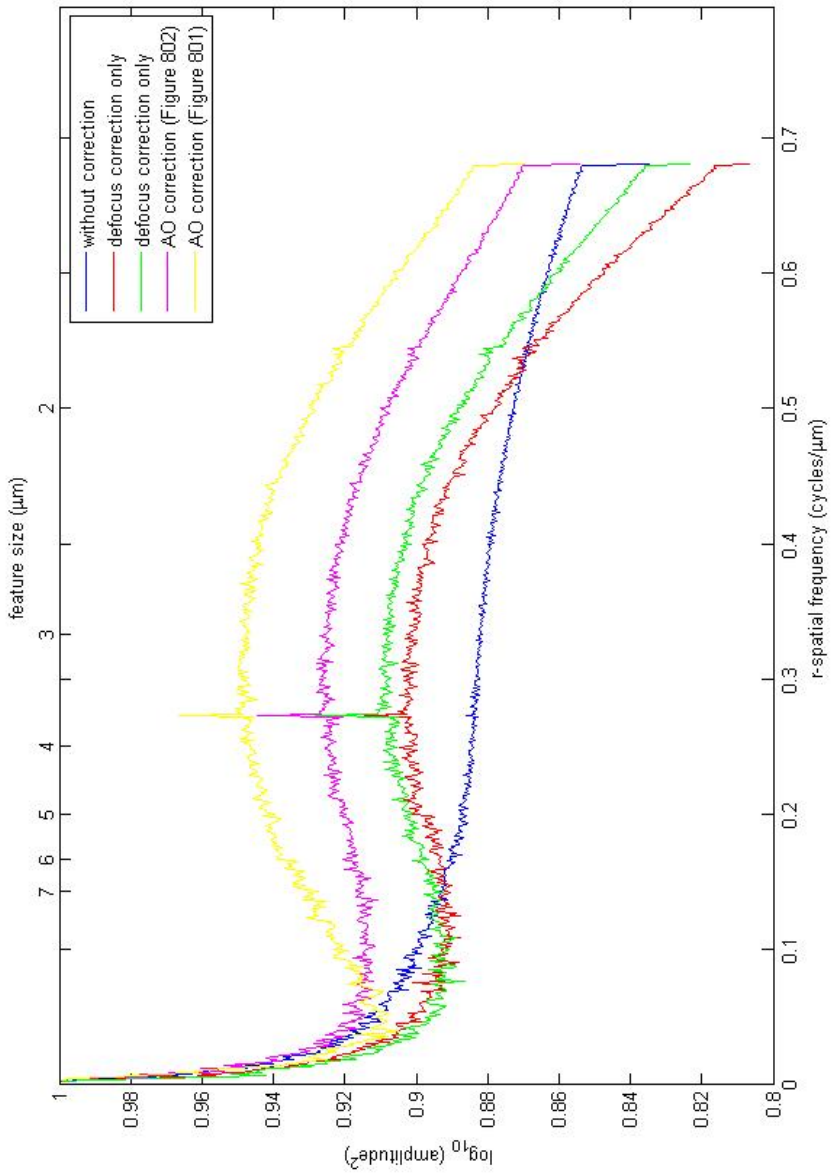

Fig. 8.7: Power spectra comparison of images without aberration correction, with defocus correction, and with adaptive optics correction showing an increased resolution of finer structure in corrected images. The figure also shows images taken from different subjects at different eccentricities showing different frequency contents.

9. CONCLUSIONS

An adaptive optics retinal imaging system was designed and built, and its performance was tested. The aim was to prove, in concept, that potentially low-cost high-resolution imaging of a 4° field-of-view can be achieved. Using light emitting diodes for both illumination and wavefront sensing, a Boston Micromachines Corporation deformable mirror as a corrector, and a Thorlabs Shack-Hartmann wavefront sensor; the system could achieve retinal images with visible features in the range of $2 - 6\ \mu m$.

In chapter 4, a simulation of the deformable mirror showed that it is capable of correcting mildly aberrated eyes to the diffraction limit, when accompanied by a Badal optometer for defocus correction. Chapter 5 shows the Zemax optimisation of the optical setup, and shows diffraction-limited performance at the end of both wavefront sensing and imaging arms, over the whole intended field-of-view. The methods used to align the optical setup and to verify its performance are discussed in chapter 6. We report actual Strehl ratios of 0.95 and 0.93 were achieved at the end of the wavefront sensing and imaging arms respectively. These figures are only representative of the optical setup's performance without a human eye aligned into the setup. Chapter 7 discusses the control algorithms which were used to calibrate and control the adaptive optics closed-loop operation. Chapter 8 shows a few samples of the retinal images which have been obtained using the optical system, and uses a power spectrum metric to quantify image quality and investigate the fine structure.

It is important to point out that this study is a single step towards achieving a low-cost high-resolution retinal imaging system. The images acquired at this stage are just a proof-of-concept. The quality of these images can be improved with some modifications to the optical design (discussed in section 9.1) and with image processing. For instance, image registration of tens of frames leads to better defined cones in an image. The images displayed in chapter 8 are raw frames with minimum processing for display purposes. The optical system needs a good amount of work before it qualifies to be an industry prototype.

The main cost associated with commercialising this instrument is the deformable mirror; however, we estimate that its cost will drop well below €10,000 when manufactured in larger quantities. CCD camera, and even suggested back-illuminated CMOS cameras, have dropped in cost that they are fitted as add-ons on mobile phones.

9.1 Future work

This optical setup serves as a proof-of-concept for a potentially low-cost high-resolution retinal imaging system. The next step is to improve upon image quality, optical design, and mobility of the optical setup. Based on building and testing this optical setup, the following improvements are suggested:

- The Boston Micromachines Corporation deformable mirror in its commercial casing is a bulky object, which results in an overall larger system dimensions. Upon coordination with Boston Micromachines Corporation, the deformable mirror should be taken out of its casing, and the cables leading to it should be channelled out using a mechanical rigid construction. The cables are heavy, and not channelling them correctly would result in a less than stable alignment of the setup.

- The imaging camera could be replaced with a new back-illuminated CMOS camera, of smaller pixel size. As a result, the system will have higher light sensitivity which translates into higher image quality in low light conditions. In addition, using smaller pixels means less optical magnification at the same sampling rate. This shortens the required axial travel distance for the camera when moving through the different layers of the retina. However, smaller pixel size leads to more noise. Therefore, the pixel size should be optimised to achieve a reasonable magnification without compromising the signal-to-noise ratio.

- The current imaging light emitting diodes assembly was bought off-the-shelf. By customising this assembly and bringing the LEDs closer together, the LED assembly could be brought closer to the eye resulting in a lower light loss factor.

- The wavefront sensing process can be optimised by using a back-illuminated CMOS camera to increase the sensitivity, and by using a cross-correlation

algorithm for more accurate centroiding.

- A low resolution wide-field camera ($20° - 30°$) is a good add-on to the system, and helps the photographer determine the exact imaging position on the retina.

- For the instrument to be operable as a stand-alone device in a clinical setup, the control computer could be replaced by a field programmable gate array (FPGA) or a graphics processing unit (GPU). A laptop could then be used to acquire and store images, and manage patients databases.

APPENDICES

A. ZERNIKE POLYNOMIALS

Zernike polynomials are a sequence of orthonormal polynomials that describe different types of aberrations. A wavefront can be represented as a linear combination of Zernike polynomials, each polynomial effect is weighed by its coefficient. Zernike polynomials have different mathematical definitions in the literature where polynomials like Z_3^{-3} and Z_3^3 might be swapped for instance. That is why the notation used should be defined considering Zernike polynomials.

In our study,the notation used is shown in Table A.1 below.

Tab. A.1: The first 15 Zernike polynomials according to the notation used in our study. [100].

$j =$ index	$n =$ order	$m =$ frequency	Aberration type	$Z_n^m(\rho, \theta)$	$Z_n^m(x, y)$
1	0	0	Piston	1	1
2	1	-1	Tip y	$2\rho \sin\theta$	$2y$
3	1	1	Tilt x	$2\rho \cos\theta$	$2x$
4	2	-2	Astigmatism $\pm 45°$	$\sqrt{6}\rho^2 \sin 2\theta$	$\sqrt{6}(2xy)$
5	2	0	Defocus	$\sqrt{3}(2\rho^2 - 1)$	$\sqrt{3}(2x^2 + 2y^2 - 1)$
6	2	2	Astigmatism $0°, 90°$	$\sqrt{6}\rho^2 \cos 2\theta$	$\sqrt{6}(x^2 - y^2)$
7	3	-3	Trefoil y	$\sqrt{8}\rho^3 \sin 3\theta$	$\sqrt{8}(3x^2y - y^3)$
8	3	-1	Coma x	$\sqrt{8}(3\rho^3 - 2\rho) \sin\theta$	$\sqrt{8}(3x^2y + 3y^3 - 2y)$
9	3	1	Coma y	$\sqrt{8}(3\rho^3 - 2\rho) \cos\theta$	$\sqrt{8}(3x^3 + 3xy^2 - 2x)$
10	3	3	Trefoil x	$\sqrt{8}\rho^3 \cos 3\theta$	$\sqrt{8}(x^3 - 3xy^2)$
11	4	-4	Tetrafoil y	$\sqrt{10}\rho^4 \sin 4\theta$	$\sqrt{10}(4x^3y - 4xy^3)$
12	4	-2	Sec. Astigmatism y	$\sqrt{10}(4\theta^4 - 3\rho^2) \sin 2\theta$	$\sqrt{10}(8x^3y + 8xy^3 - 6xy)$
13	4	0	Sperical Aberr. 3	$\sqrt{5}(6\rho^4 - 6\rho^2 + 1)$	$\sqrt{5}(6x^4 + 12x^2y^2 + 6y^4 - 6x^2 - 6y^2 + 1)$
14	4	2	Sec. Astigmatism x	$\sqrt{10}(4\theta^4 - 3\rho^2) \cos 2\theta$	$\sqrt{10}(4x^4 - 3x^2 - 4y^4 + 3y^2)$
15	4	4	Tetrafoil x	$\sqrt{10}\rho^4 \cos 4\theta$	$\sqrt{10}(x^4 - 6x^2y^2 + y^4)$

B. HEALTH AND SAFETY CALCULATIONS

This appendix includes the calculations of safety limits involved with illuminating the eyes. The calculations were done according to both the European and the American standards.

B.1 European safety standards (ICNIRP)

European safety standards are given in units of irradiance (mW/cm^2). The irradiance due to our illumination LED (530 nm) at the pupil was 0.106 mW/cm^2 with a 6 mm pupil. The irradiance of our wavefront sensing LED (850 nm) at the pupil was 7.68 $\mu W/cm^2$ with a 6 mm pupil. The calculations below are based on continuous wave (CW) operation for an exposure time of up to 30 ks (8 hours 20 minutes) [115].

The maximum permissible radiant exposure due to more than one source is safe if:

$$\frac{E_{\lambda 1}}{EL[\lambda_1]} + \frac{E_{\lambda 2}}{EL[\lambda_2]} + ... < 1 \tag{B.1}$$

Photochemical exposure limit only applies to the 530 nm source, and is given by:

$$\begin{aligned} EL(530\ nm - Ph) &= 0.1 C_B\ mW/cm^2 \\ &= 0.1 \times 10^{0.02(\lambda - 450)}\ mW/cm^2 \\ &= 3.981\ mW/cm^2 \end{aligned} \tag{B.2}$$

Comparing the photochemical limit (from equation B.2) to the irradiance of the LED used in our setup:

$$\begin{aligned} \frac{E_{530\ nm}}{EL[530\ nm]} &\overset{?}{<} 1 \\ \frac{0.212}{3.981} &\overset{?}{<} 1 \\ 0.0533 &< 1 \end{aligned} \tag{B.3}$$

Thermal and photoacoustic exposure limit for both light sources is given by:

$$\begin{aligned} EL(530\ nm - Th) &= 1.8 C_E T_2^{-0.25}\ mW/cm^2 \\ &= 1.8 \times \frac{\alpha}{\alpha_{min}} \times 100^{-0.25}\ mW/cm^2 \\ &= 1.8 \times \frac{169}{1.5} \times 100^{-0.25}\ mW/cm^2 \\ &= 64.13\ mW/cm^2 \end{aligned} \tag{B.4}$$

$$\begin{aligned} EL(850\ nm - Th) &= 1.0 C_A C_C\ mW/cm^2 \\ &= 1.0 \times 10^{0.002(\lambda - 700)} \times 1\ mW/cm^2 \\ &= 1.995\ mW/cm^2 \end{aligned} \tag{B.5}$$

Comparing thermal safety limits (from equations B.4, B.5) to the irradiance of the LEDs used in our setup:

$$\begin{aligned} \frac{E_{530\ nm}}{EL[530\ nm]} + \frac{E_{850\ nm}}{EL[850\ nm]} &\overset{?}{<} 1 \\ \frac{0.212}{64.13} + \frac{0.00768}{1.995} &\overset{?}{<} 1 \\ 0.00716 &< 1 \end{aligned} \tag{B.6}$$

Thus the irradiance of the LEDs at the level of the pupil is $< 6\%$ of European safety limits.

B.2 American safety standards (ANSI)

The maximum permissible exposure was calculated according to the ANSI —136.1-2000 standard for protection of the human eye. A more thorough analysis and further explanation of the calculations involved here could be found in [116]. The maximum permissible radiant power ($MP\Phi$) entering the natural or dilated pupil is given in units of radiant power (W). The calculations below are based on continuous wave (CW) operation for an exposure time of up to $30ks$ (8 hours 20 minutes).

Photochemical $MP\Phi$ only applies to the 530 nm source, and is given by:

$$\begin{aligned} MP\Phi(530\ nm - Ph) &= 5.56 \times 10^{-10} C_B\ \alpha^2 \\ &= 5.56 \times 10^{-10} \times \frac{1}{10^{0.020(\lambda - 450)}} \times 169^2 \\ &= 632\ \mu W \end{aligned} \tag{B.7}$$

Comparing the photochemical $MP\Phi$ (from equation B.7) to the irradiance of the LED used in our setup:

$$\begin{aligned} \frac{\Phi_{530\ nm}}{MP\Phi[530\ nm]} &\overset{?}{<} 1 \\ \frac{60}{632} &\overset{?}{<} 1 \\ 0.0949 &< 1 \end{aligned} \tag{B.8}$$

Thermal and photoacoustic $MP\Phi$ for both light sources is given by:

$$\begin{aligned} MP\Phi(530\ nm - Th) &= 6.93 \times 10^{-5} C_T C_E P^{-1} \\ &= 6.93 \times 10^{-5} \times 1 \times (6.67 \times 10^{-3} \times \alpha^2) \times 5.44^{-1} \\ &= 2.43\ mW \end{aligned} \tag{B.9}$$

$$\begin{aligned} MP\Phi(850\ nm - Th) &= 1.8 \times 10^{-3} C_T C_E T_2^{-0.25} t \\ &= 1.8 \times 10^{-3} \times 10^{0.002(\lambda - 700)} \times 1 \times 10^{-0.25} \times 1 \\ &= 2.02\ mW \end{aligned} \tag{B.10}$$

Comparing thermal $MP\Phi$ (from equations B.9, B.10) to the irradiance of the LEDs used in our setup:

$$\begin{aligned} \frac{\Phi_{530\ nm}}{MP\Phi[530\ nm]} + \frac{\Phi_{850\ nm}}{MP\Phi[850\ nm]} &\overset{?}{<} 1 \\ \frac{60}{2430} + \frac{8.44}{2020} &\overset{?}{<} 1 \\ 0.0289 &< 1 \end{aligned} \tag{B.11}$$

Thus the radiant power of the LEDs at the level of the pupil is $< 10\%$ of American safety limits.

C. LABVIEW CODE

This appendix includes the main Labview VI's described in chapter 7. Each contains several sub-VI's which are not shown in detail. The figures correspondence is shown in Table C.1.

Tab. C.1: Virtual instrument titles and their corresponding figures.

VI title	Corresponding figures
Acquisition of phase maps	Figure C.1 Figure C.2 Figure C.3
Building the control matrix	Figure C.4 Figure C.5 Figure C.6
Adaptive optics closed-loop control	Figure C.7 Figure C.8 Figure C.9 Figure C.10 Figure C.11

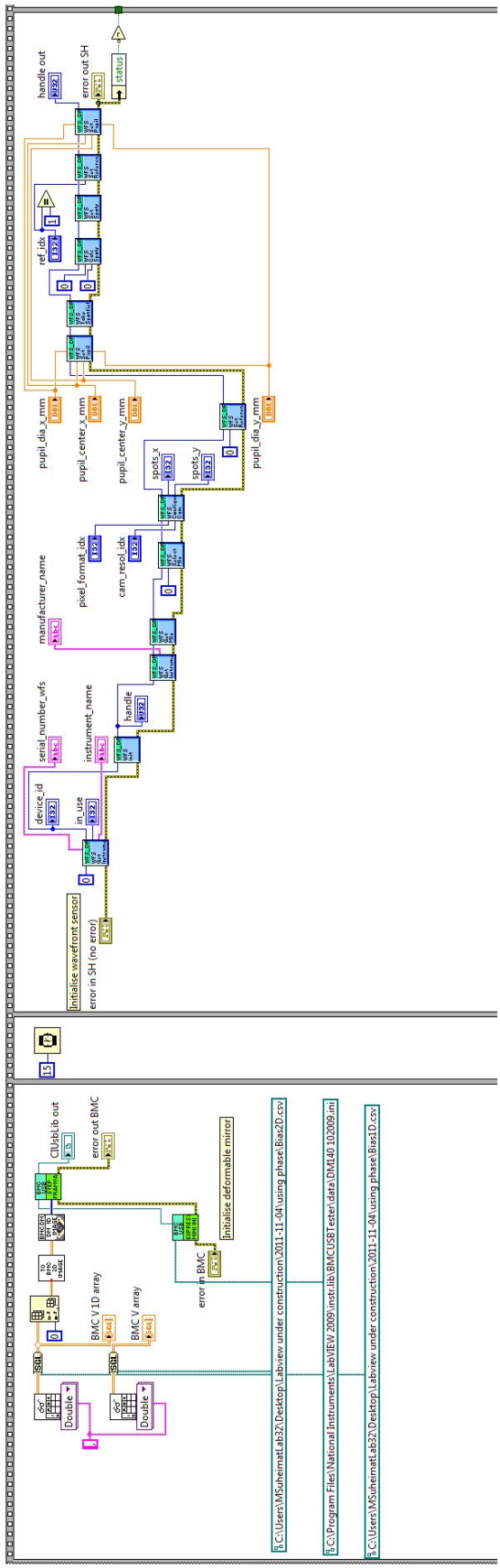

Fig. C.1: Acquisition of phase maps (1/3): Variable definitions; deformable mirror and Shack-Hartmann wavefront sensor initialisation; settings read-out.

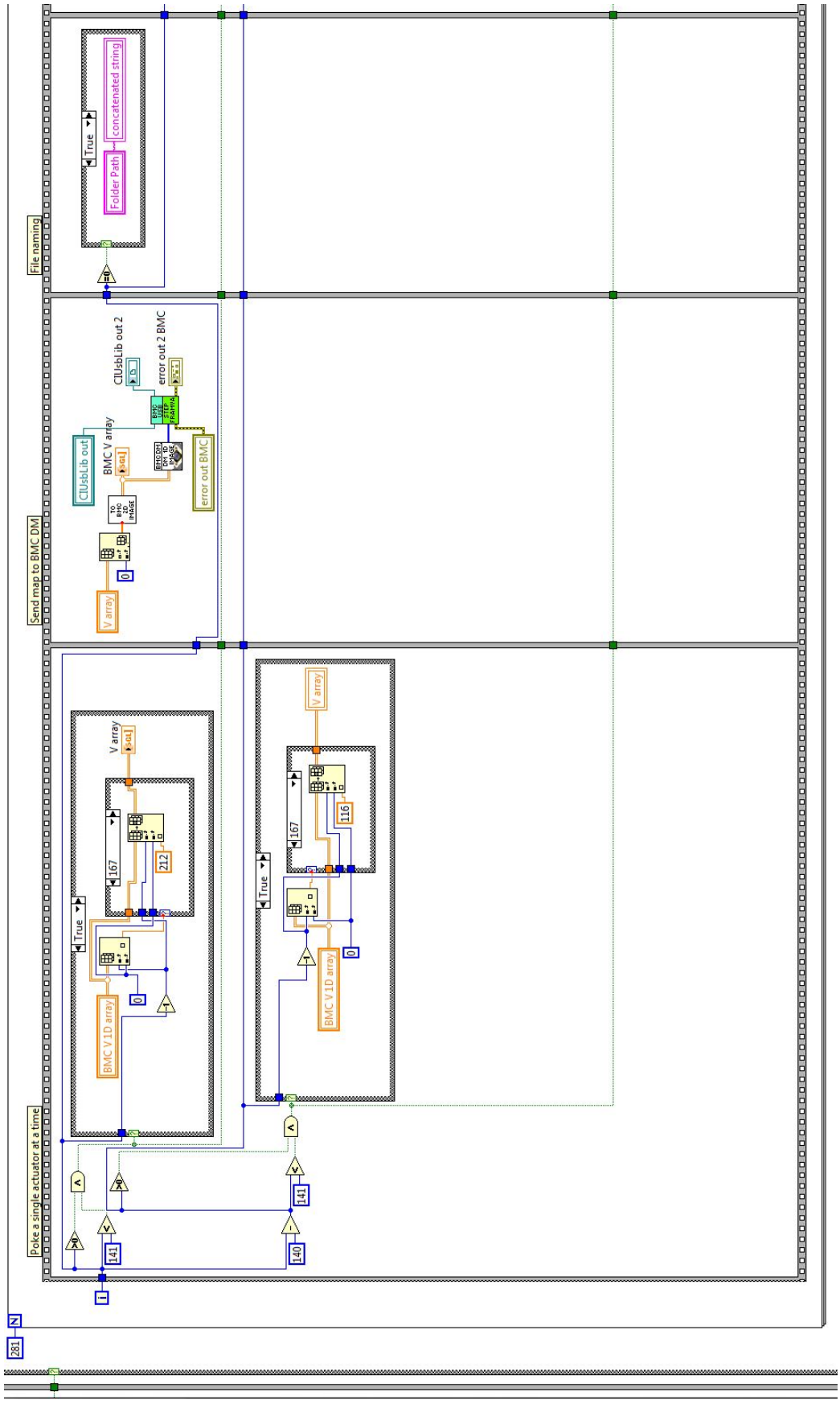

Fig. C.2: Acquisition of phase maps (2/3): Poking one actuator at a time to ± 0.5 of its maximum displacement; voltage conversion; voltage map sent to deformable mirror; automatic file naming.

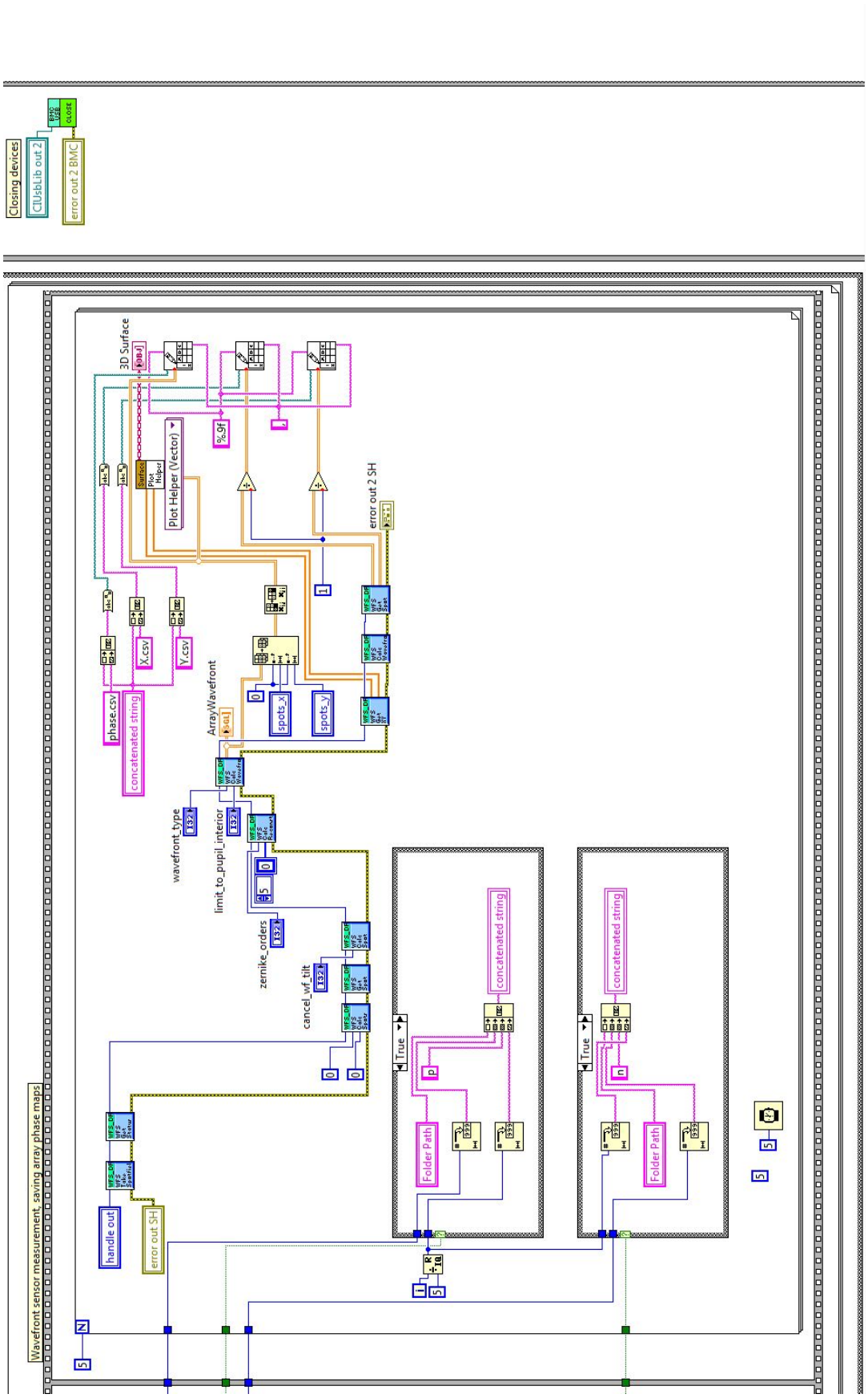

Fig. C.3: Acquisition of phase maps (3/3): Wavefront sensor measurement, phase maps acquisition; files saved; devices stopped and matrices cleared.

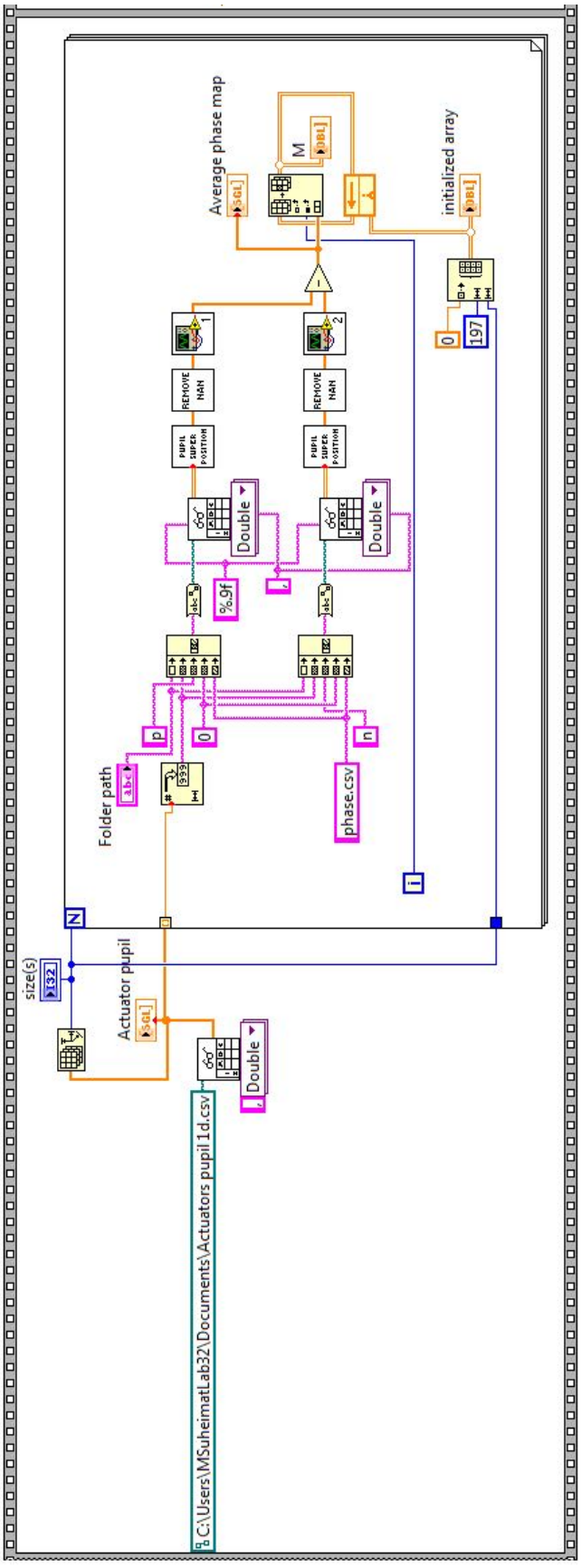

Fig. C.4: Building the control matrix (1/3): Phase maps read-out from saved files; pupil superposition; phase maps processed; influence function matrix **M** is built.

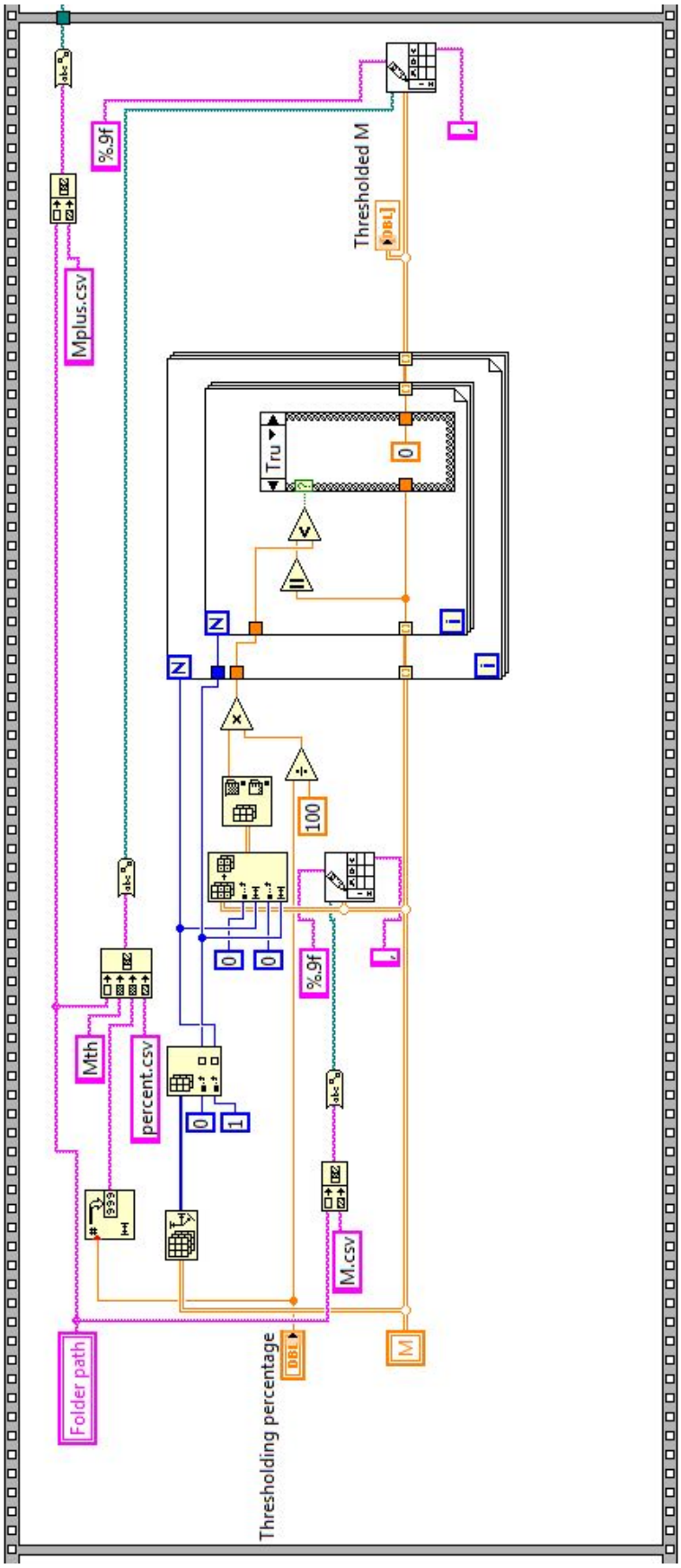

Fig. C.5: Building the control matrix (2/3): Thresholding option (disabled by default).

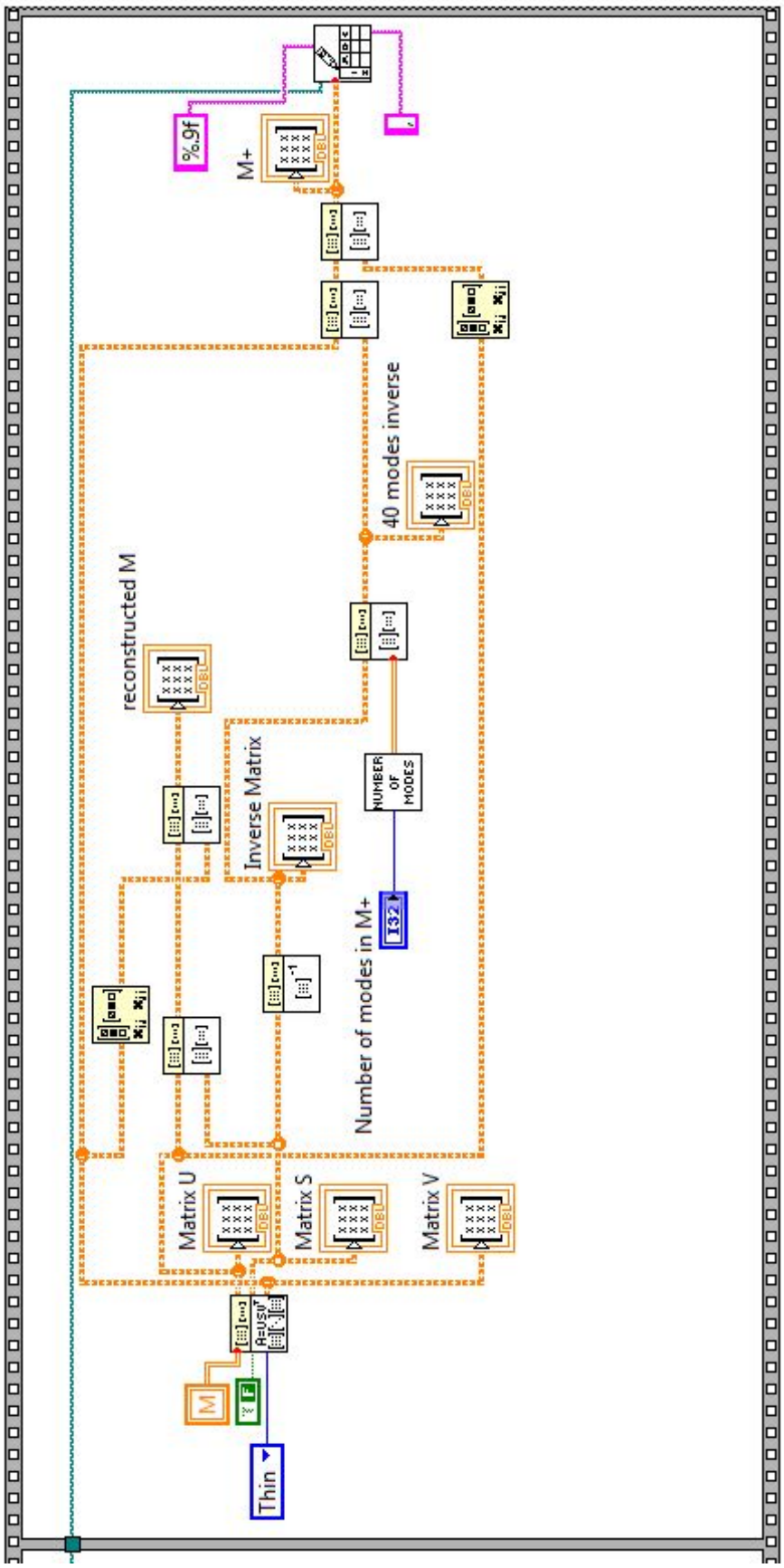

Fig. C.6: Building the control algorithm (3/3): Singular value decomposition of $\mathbf{M}$; $\mathbf{W}$ is reduced to the input "Number of modes in M+"; $\mathbf{M}^+$ is calculated and saved.

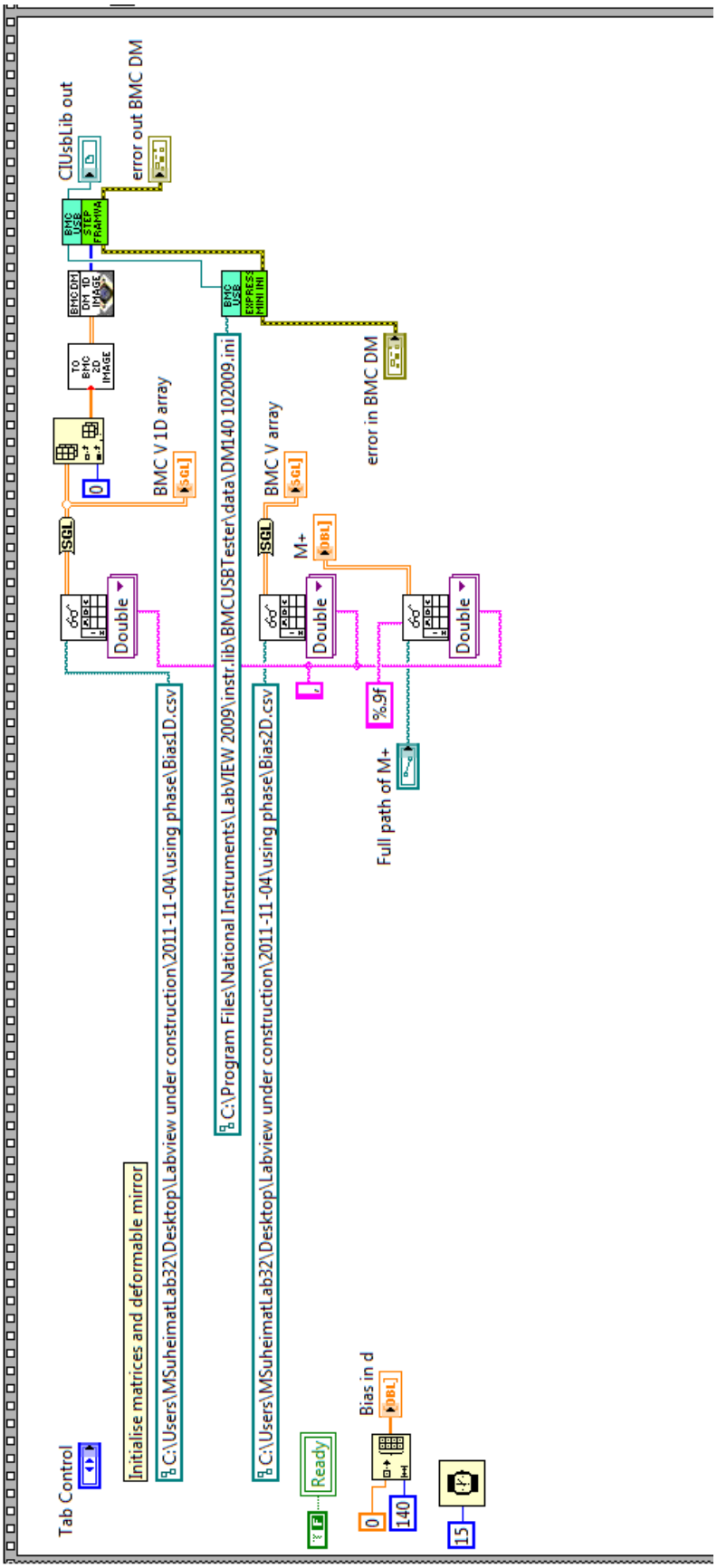

Fig. C.7: Adaptive optics closed-loop operation (1/5): Variable definitions and deformable mirror initialisation.

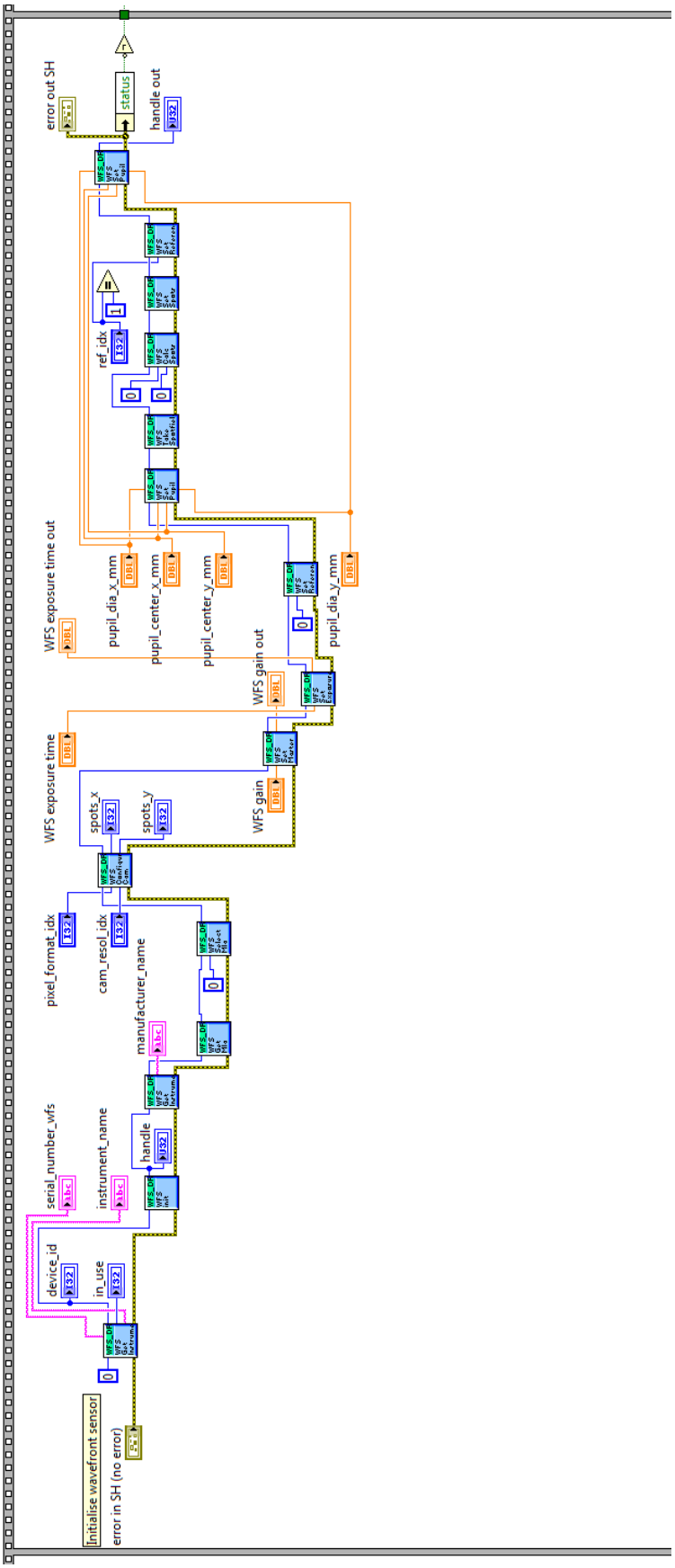

Fig. C.8: Adaptive optics closed-loop operation (2/5): Settings read-out and Shack-Hartmann wavefront sensor initialisation.

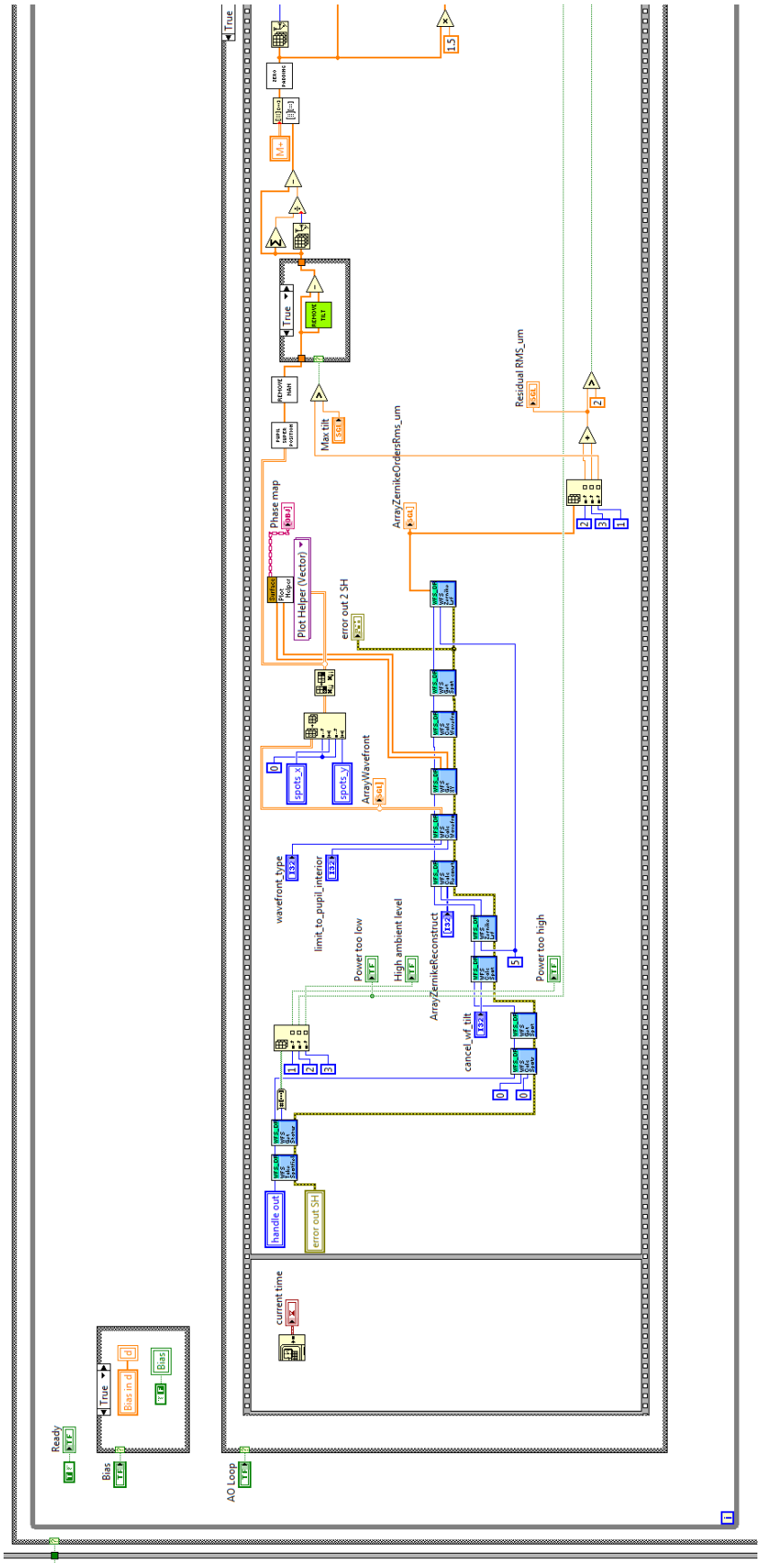

Fig. C.9: Adaptive optics closed-loop operation (3/5): Timer starts; phase map read-out and display; input settings application; control matrix multiplication; displacement matrix calculation.

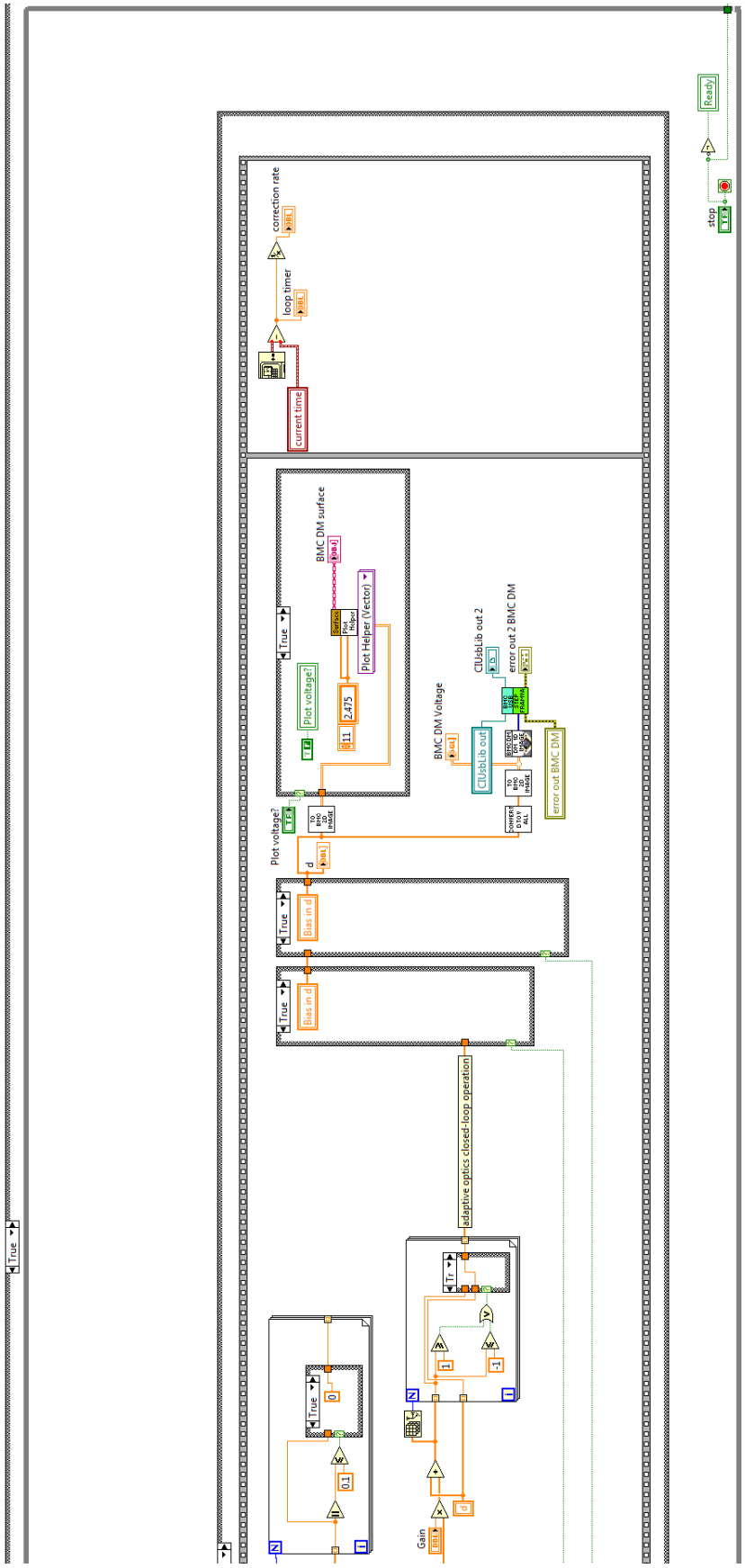

Fig. C.10: Adaptive optics closed-loop operation (4/5): Logical conditions application; displacement to voltage conversion; voltage map display and output to the deformable mirror driver; timer stops.

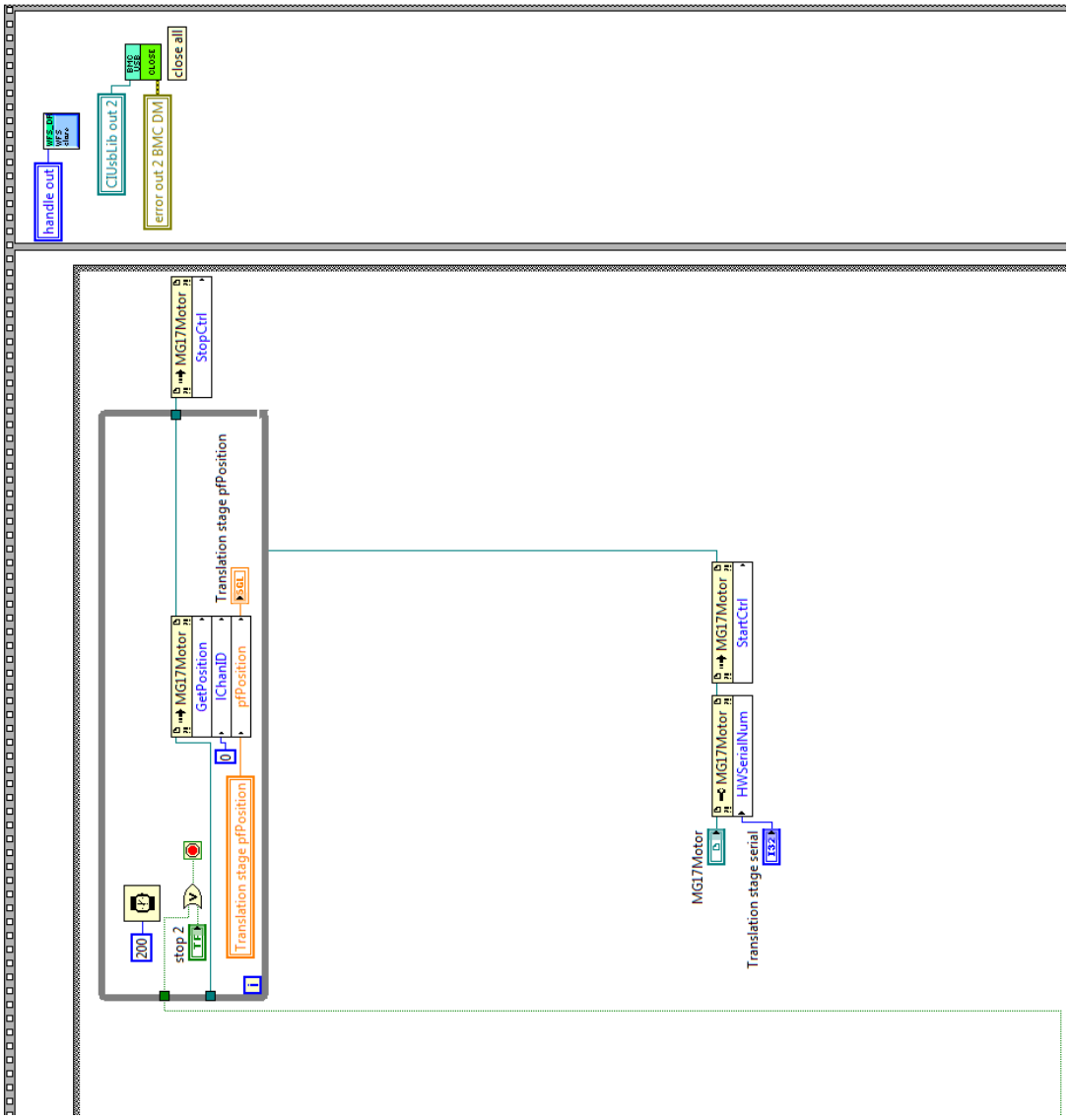

Fig. C.11: Adaptive optics closed-loop operation (5/5): Translational stage control. Devices stopped and matrices cleared.

BIBLIOGRAPHY

[1] Toshiaki Nakagawa, Takayoshi Suzuki, Yoshinori Hayashi, Yutaka Mizukusa, Yuji Hatanaka, Kyoko Ishida, Takeshi Hara, Hiroshi Fujita, and Tetsuya Yamamoto. Quantitative depth analysis of optic nerve head using stereo retinal fundus image pair. *Journal of biomedical optics*, 13(6):064026, 2008.

[2] Yueli Chen, Daina L Burnes, Martijn de Bruin, Mircea Mujat, and Johannes F de Boer. Three-dimensional pointwise comparison of human retinal optical property at 845 and 1060 nm using optical frequency domain imaging. *Journal of biomedical optics*, 14(2):024016, 2009.

[3] M. Hammer, T. Riemer, W. Vilser, S. Gehlert, and D. Schweitzer. A new imaging technique for retinal vessel oximetry: principles and first clinical results in patients with retinal arterial occlusion and diabetic retinopathy. *Proceedings of SPIE*, 7163:71630P–71630P–12, 2009.

[4] Heidi Hofer, Joseph Carroll, Jay Neitz, Maureen Neitz, and David R Williams. Organization of the human trichromatic cone mosaic. *Journal of Neuroscience*, 25(42):9669–9679, 2005.

[5] Jessica I Wolfing, Mina Chung, Joseph Carroll, Austin Roorda, and David R Williams. High-resolution retinal imaging of cone-rod dystrophy. *Ophthalmology*, 113(6):1019.e1, June 2006.

[6] Niall Patton, Tariq M Aslam, Thomas MacGillivray, Ian J Deary, Baljean Dhillon, Robert H Eikelboom, Kanagasingam Yogesan, and Ian J Constable. Retinal image analysis: concepts, applications and potential. *Progress in retinal and eye research*, 25(1):99–127, January 2006.

[7] Robert K. Tyson. *Introduction to Adaptive Optics*. Spie, 2000.

[8] C Paterson, I Munro, and J Dainty. A low cost adaptive optics system using a membrane mirror. *Optics express*, 6(9):175–85, April 2000.

[9] Alexander Dubinin. Anisoplanatism in human retina imaging. *Proceedings of SPIE*, 5894:589409–589409–7, 2005.

[10] W. T. Jackman and J. D. Webster. On photographing the retina of the living human eye. *Philadelphia Photography*, 23:275–276, 1886.

[11] P J Saine. Landmarks in the historical development of fluorescein angiography. *The Journal of ophthalmic photography*, 15(1):17–23, April 1993.

[12] Junzhong Liang, David R. Williams, and Donald T. Miller. Supernormal vision and high-resolution retinal imaging through adaptive optics. *Journal of the Optical Society of America A*, 14(11):2884, November 1997.

[13] Austin Roorda, Fernando Romero-Borja, III Donnelly, Hope Queener, Thomas Hebert, and Melanie Campbell. Adaptive optics scanning laser ophthalmoscopy. *Optics Express*, 10(9):405–412, May 2002.

[14] Donald T. Miller. Coherence gating and adaptive optics in the eye. *Proceedings of SPIE*, 4956:65–72, 2003.

[15] Austin Roorda. Adaptive optics for studying visual function: a comprehensive review. *Journal of vision*, 11(7), January 2011.

[16] H W Babcock. The possibility of compensating astronomical seeing. *Publications of the Astronomical Society of the Pacific*, 65(386):229–236, 1953.

[17] J W Hardy, J E Lefebvre, and C L Koliopoulos. Real-time atmospheric compensation. *Journal of the Optical Society of America*, 67(3):360–369, 1977.

[18] A W Dreher, J F Bille, and R N Weinreb. Active optical depth resolution improvement of the laser tomographic scanner. *Applied Optics*, 28(4):804–808, 1989.

[19] Thomas Nirmaier, Gopal Pudasaini, and Josef Bille. Very fast wave-front measurements at the human eye with a custom CMOS-based Hartmann-Shack sensor. *Optics Express*, 11(21):2704, October 2003.

[20] K.M. Hampson. Adaptive optics and vision. *Journal of Modern Optics*, 55(21):3425–3467, December 2008.

[21] E J Fernández, I Iglesias, and P Artal. Closed-loop adaptive optics in the human eye. *Optics Letters*, 26(10):746–748, 2001.

[22] Guang-ming (George) Dai. *Wavefront Optics for Vision Correction (SPIE Press Monograph Vol. PM179)*. SPIE Publications, 2008.

[23] R Navarro, E Moreno, and C Dorronsoro. Monochromatic aberrations and point-spread functions of the human eye across the visual field. *Journal of the Optical Society of America A*, 15(9):2522–2529, 1998.

[24] Alexander Dubinin. Human eye anisoplanatism: eye as a lamellar structure. *Proceedings of SPIE*, 6138:613813–613813–7, 2006.

[25] Ignacio Iglesias, Roberto Ragazzoni, Yves Julien, and Pablo Artal. Extended source pyramid wave-front sensor for the human eye. *Optics express*, 10(9):419–28, May 2002.

[26] Stéphane R Chamot, Chris Dainty, and Simone Esposito. Adaptive optics for ophthalmic applications using a pyramid wavefront sensor. *Optics Express*, 14(2):518–526, 2006.

[27] Eugenie Dalimier and Chris Dainty. Comparative analysis of deformable mirrors for ocular adaptive optics. *Optics express*, 13(11):4275–85, May 2005.

[28] Nathan Doble, Donald T Miller, Geunyoung Yoon, and David R Williams. Requirements for discrete actuator and segmented wavefront correctors for aberration compensation in two large populations of human eyes. *Applied Optics*, 46(20):4501–4514, 2007.

[29] S. Bonora, D. Coburn, U. Bortolozzo, C. Dainty, and S. Residori. High resolution wavefront correction with photocontrolled deformable mirror. *Optics Express*, 20(5):5178, February 2012.

[30] Enrique J Fernández, Pedro M Prieto, and Pablo Artal. Binocular adaptive optics visual simulator. *Optics letters*, 34(17):2628–30, September 2009.

[31] Christina Schwarz, Pedro M. Prieto, Enrique J. Fernández, and Pablo Artal. Binocular adaptive optics vision analyzer with full control over the complex pupil functions. *Optics Letters*, 36(24):4779, December 2011.

[32] C D Saunter and G D Love. FPGA technology for high-speed low-cost adaptive optics. *5th International Workshop on Adaptive Optics for Industry and Medicine Edited by Jiang Wenhan Proceedings of the SPIE Volume 6018*, dvanced Wa:107, 2007.

[33] A Roorda and D R Williams. The arrangement of the three cone classes in the living human eye. *Nature*, 397:520–522, 1999.

[34] Katherine Mancuso, William W Hauswirth, Qiuhong Li, Thomas B Connor, James A Kuchenbecker, Matthew C Mauck, Jay Neitz, and Maureen Neitz. Gene therapy for red-green colour blindness in adult primates. *Nature*, 461(7265):784–787, 2009.

[35] D S Shin, N B Javornik, and J W Berger. Computer-assisted, interactive fundus image processing for macular drusen quantitation. Technical Report 6, Computer Vision Laboratory, Scheie Eye Institute, University of Pennsylvania School of Medicine, Philadelphia 19104, USA., 1999.

[36] Chisako Muramatsu, Toshiaki Nakagawa, Akira Sawada, Yuji Hatanaka, Takeshi Hara, Tetsuya Yamamoto, and Hiroshi Fujita. Determination of cup-to-disc ratio of optical nerve head for diagnosis of glaucoma on stereo retinal fundus image pairs. *Proceedings of SPIE*, 7260:72603L–72603L–8, 2009.

[37] R J Winder, P J Morrow, I N McRitchie, J R Bailie, and P M Hart. Algorithms for digital image processing in diabetic retinopathy. *Computerized medical imaging and graphics : the official journal of the Computerized Medical Imaging Society*, 33(8):608–22, December 2009.

[38] Imagine Eyes. rtx1 adaptive optics retinal camera. `http://www.imagine-eyes.com/content/view/122/124/`, Date cited: October 18, 2011.

[39] Luis Diaz-Santana, Cristiano Torti, Ian Munro, Paul Gasson, and Chris Dainty. Benefit of higher closed-loop bandwidths in ocular adaptive optics. *Optics express*, 11(20):2597–605, October 2003.

[40] Kate Grieve, Pavan Tiruveedhula, Yuhua Zhang, and Austin Roorda. Multi-wavelength imaging with the adaptive optics scanning laser ophthalmoscope. *Opt. Express*, 14(25):12230–12242, Dec 2006.

[41] Fred Reinholz, Ross A. Ashman, and Robert H. Eikelboom. Simultaneous three wavelength imaging with a scanning laser ophthalmoscope. *Cytometry*, 37(3):165–170, 1999.

[42] Daniel X. Hammer, R. Daniel Ferguson, Chad E. Bigelow, Nicusor V. Iftimia, Teoman E. Ustun, and Stephen A. Burns. Adaptive optics scanning laser ophthalmoscope for stabilized retinal imaging. *Opt. Express*, 14(8):3354–3367, Apr 2006.

[43] Stephen A. Burns, Remy Tumbar, Ann E. Elsner, Daniel Ferguson, and Daniel X. Hammer. Large-field-of-view, modular, stabilized, adaptive-optics-based scanning laser ophthalmoscope. *J. Opt. Soc. Am. A*, 24(5):1313–1326, May 2007.

[44] David Merino, Chris Dainty, Adrian Bradu, and Adrian Gh Podoleanu. Adaptive optics enhanced simultaneous en-face optical coherence tomography and scanning laser ophthalmoscopy. *Optics Express*, 14(8):3345–3353, 2006.

[45] Diana C. Chen, Steven M. Jones, Dennis A. Silva, and Scot S. Olivier. High-resolution adaptive optics scanning laser ophthalmoscope with dual deformable mirrors. *J. Opt. Soc. Am. A*, 24(5):1305–1312, May 2007.

[46] Alfredo Dubra and Yusufu Sulai. Reflective afocal broadband adaptive optics scanning ophthalmoscope. *Biomedical optics express*, 2(6):1757–68, June 2011.

[47] B. Hermann, E. J. Fernández, A. Unterhuber, H. Sattmann, A. F. Fercher, W. Drexler, P. M. Prieto, and P. Artal. Adaptive-optics ultrahigh-resolution optical coherence tomography. *Opt. Lett.*, 29(18):2142–2144, Sep 2004.

[48] Yan Zhang, Jungtae Rha, Ravi Jonnal, and Donald Miller. Adaptive optics parallel spectral domain optical coherence tomography for imaging the living retina. *Opt. Express*, 13(12):4792–4811, Jun 2005.

[49] Enrique J. Fernández, Angelika Unterhuber, Boris Považay, Boris Hermann, Pablo Artal, and Woflgang Drexler. Chromatic aberration correction of the human eye for retinal imaging in the near infrared. *Optics Express*, 14(13):6213, June 2006.

[50] Robert J. Zawadzki, Barry Cense, Yan Zhang, Stacey S. Choi, Donald T. Miller, and John S. Werner. Ultrahigh-resolution optical coherence tomography with monochromatic and chromatic aberration correction. *Opt. Express*, 16(11):8126–8143, May 2008.

[51] Jörgen Thaung, Per Knutsson, Zoran Popovic, and Mette Owner-Petersen. Dual-conjugate adaptive optics for wide-field high-resolution retinal imaging. *Optics express*, 17(6):4454–67, March 2009.

[52] Thomas Berkefeld, Dirk Soltau, and Oskar Von Der Luhe. Multi-conjugate adaptive optics at the Vacuum Tower Telescope, Tenerife. *Proceedings of SPIE - The International Society for Optical Engineering*, 4538:119–127, 2002.

[53] M Born and E Wolf. *Principles of Optics: Electromagnetic Theory of Propagation, Interference and Diffraction of Light*, volume 49. Cambridge University Press, 1999.

[54] Geunyoung Yoon. Aberration Theory. `http://cfao.ucolick.org/pubs/presentations/eyedesign/05_aberrations_GY.pdf`, Date cited: October 19, 2011.

[55] X Zhang, A Bradley, and L N Thibos. Experimental determination of the chromatic difference of magnification of the human eye and the location of the anterior nodal point. *Journal of the Optical Society of America A Optics and image science*, 10(2):213–220, 1993.

[56] L N Thibos, A Bradley, D L Still, X Zhang, and P A Howarth. Theory and measurement of ocular chromatic aberration. *Vision Research*, 30(1):33–49, 1990.

[57] Donald T. Miller, Barry Cense, Erik Koperda, Ravi S. Jonnal, and Weihua Gao. Does transverse chromatic aberration limit performance of AO-OCT retinal imaging? *Proceedings of SPIE*, 7139(1):71390Z–71390Z–6, 2008.

[58] D Van Norren and L F Tiemeijer. Spectral reflectance of the human eye. *Vision Research*, 26(2):313–320, 1986.

[59] F C Delori and K P Pflibsen. Spectral reflectance of the human ocular fundus. *Applied Optics*, 28(6):1061–1077, 1989.

[60] J M Gorrand and F C Delori. Reflectance and curvature of the inner limiting membrane at the foveola. *Journal of the Optical Society of America A*, 16(6):1229–1237, 1999.

[61] Jan Van De Kraats and Dirk Van Norren. Optical density of the aging human ocular media in the visible and the UV. *Journal of the Optical Society of America A*, 24(7):1842–1857, 2007.

[62] Dan Roberts. Anatomy of the Eye. `http://www.mdsupport.org/anatomy.html`, Date cited: December 2, 2011.

[63] Larry N Thibos, Raymond A Applegate, James T Schwiegerling, and Robert Webb. Standards for reporting the optical aberrations of eyes. *Journal of refractive surgery Thorofare NJ 1995*, 18(5):S652–S660, 2000.

[64] Peter G. Shaw-McMinn. Review of Optometry: How to Provide High-Resolution Vision. `http://cms.revoptom.com/index.asp?ArticleType=SiteSpec&Page=osc/105418/lesson.htm`.

[65] David A. Goss and Roger W. West. *Introduction to the Optics of the Eye [Paperback]*. Butterworth-Heinemann; 1st edition, 2002.

[66] I M Barton, S N Dixit, L J Summers, K Avicola, and J Wilhelmsen. Diffractive Alvarez lens. *Optics letters*, 25(1):1–3, January 2000.

[67] D A Atchison, A Bradley, L N Thibos, and G Smith. Useful variations of the Badal Optometer. *Optometry and vision science official publication of the American Academy of Optometry*, 72(4):279–284, 1995.

[68] Bart Jaeken, Linda Lundström, and Pablo Artal. Peripheral aberrations in the human eye for different wavelengths: off-axis chromatic aberration. *Journal of the Optical Society of America A*, 28(9):1871, August 2011.

[69] Vladimir Sacek. Eye chromatism, total eye aberrations and diffraction. `http://www.telescope-optics.net/eye_chromatism.htm`, Date cited: January 27, 2012.

[70] Alexander V. Goncharov and Chris Dainty. Wide-field schematic eye models with gradient-index lens. *Journal of the Optical Society of America A*, 24(8):2157, August 2007.

[71] Brian Flynn and Michael Davidson. Nikon MicroscopyU Interactive Java Tutorials: Chromatic Aberration. `http://www.microscopyu.com/tutorials/java/aberrations/chromatic/index.html`, Date accessed: January 30, 2012.

[72] F Roddier. *Adaptive Optics in Astronomy*, volume 47. Cambridge University Press, 1999.

[73] R Navarro and E Moreno-Barriuso. Laser ray-tracing method for optical testing. *Optics Letters*, 24(14):951–953, 1999.

[74] R Navarro and M A Losada. Aberrations and relative efficiency of light pencils in the living human eye. *Optometry and vision science : official publication of the American Academy of Optometry*, 74(7):540–7, July 1997.

[75] Roberto Ragazzoni. Pupil plane wavefront sensing with an oscillating prism. *Journal of Modern Optics*, 43(2):289–293, 1996.

[76] E Gaviola. On the quantitative use of the Foucault knife-edge test. *Journal of the Optical Society of America*, 26(4):163, 1936.

[77] Anna Burvall, Elizabeth Daly, Stéphane R Chamot, and Christopher Dainty. Linearity of the pyramid wavefront sensor. *Optics Express*, 14(25):11925–11934, 2006.

[78] Elizabeth M Daly and Christopher J Dainty. Measuring phase aberrations using a pyramid wave front sensor. *Proceedings of SPIE*, 7726(2):77260W–77260W–6, 2010.

[79] C. Leroux and C. Dainty. A simple and robust method to extend the dynamic range of an aberrometer. *Optics Express*, 17(21):19055, October 2009.

[80] Junzhong Liang, Bernhard Grimm, Stefan Goelz, and Josef F. Bille. Objective measurement of wave aberrations of the human eye with the use of a Hartmann-Shack wave-front sensor. *Journal of the Optical Society of America A*, 11(7):1949, July 1994.

[81] Robert K. Tyson. *Principles of Adaptive Optics, Second Edition*. Academic Press, 1997.

[82] Geunyoung Yoon. Wavefront Sensing and Diagnostic Uses. In *Adaptive Optics for Vision Science*, pages 63–84. Wiley, New York, 2006.

[83] C Leroux and C Dainty. Estimation of centroid positions with a matched-filter algorithm: relevance for aberrometry of the eye. *Optics Express*, 18(2):1197–1206, 2010.

[84] Erkin Sidick, Joseph J Green, Rhonda M Morgan, Catherine M Ohara, and David C Redding. Adaptive cross-correlation algorithm for extended scene Shack-Hartmann wavefront sensing. *Optics letters*, 33(3):213–5, February 2008.

[85] Nicholas Devaney, Derek Coburn, Chris Coleman, J. Christopher Dainty, Eugenie Dalimier, Thomas Farrell, David Lara, David Mackey, and Ruth Mackey. Characterisation of MEMs mirrors for use in atmospheric and ocular wavefront correction. *Proceedings of SPIE*, 6888(Mmdm):688802–688802–10, 2008.

[86] Boston Micromachines Corportation Multi-DM Product Page. `http://www.bostonmicromachines.com/vision-science.htm`, Date cited: February 8, 2012.

[87] Boston Micromachines MEMS Mirrors Product Information Page. `http://www.bostonmicromachines.com/mems.htm`, Date cited: February 8,2012.

[88] C Leahy, C Leroux, C Dainty, and L Diaz-Santana. Temporal dynamics and statistical characteristics of the microfluctuations of accommodation: dependence on the mean accommodative effort. *Optics Express*, 18(3):2668–2681, 2010.

[89] Mingxia Zhu. *Microfluctuations of wavefront aberrations of the eye*. PhD thesis, Queensland University of Technology, 2005.

[90] David L. Fried. Least-square fitting a wave-front distortion estimate to an array of phase-difference measurements. *Journal of the Optical Society of America*, 67(3):370, March 1977.

[91] W H Southwell. Wave-front estimation from wave-front slope measurements. *Journal of the Optical Society of America*, 70(8):998, 1980.

[92] Alfredo Dubra. Wavefront sensor and wavefront corrector matching in adaptive optics. *Optics Express*, 15(6):2762–2769, 2007.

[93] R Conan, C Bradley, P Hampton, O Keskin, A Hilton, and C Blain. Distributed modal command for a two-deformable-mirror adaptive optics system. *Applied Optics*, 46(20):4329–4340, 2007.

[94] Larry N Thibos. Retinal image quality for virtual eyes generated by a statistical model of ocular wavefront aberrations. *Ophthalmic & physiological optics : the journal of the British College of Ophthalmic Opticians (Optometrists)*, 29(3):288–91, May 2009.

[95] Enrique Fernández, Angelika Unterhuber, Pedro Prieto, Boris Hermann, Wolfgang Drexler, and Pablo Artal. Ocular aberrations as a function of wavelength in the near infrared measured with a femtosecond laser. *Optics Express*, 13(2):400–409, 2005.

[96] Thorlabs. LED780E Ultra Bright NIR LED Specifications and Documentation.

[97] Wesentliche Merkmale, Safety Advices, and Ordering Code. High Power Infrared Emitter (850 nm) SFH 4550 Specifications Sheet. pages 1–7, 2010.

[98] Andrew O'Brien. *Simple device to measure the macular pigment optical density in vivo*. PhD thesis, National University of Ireland, Galway, 2008.

[99] Philips Lumileds. LUXEON Rebel and LUXEON Rebel ES Color Portfolio. `http://www.luxeonstar.com/v/vspfiles/downloadables/DS68.pdf`, 2012.

[100] Optical Wavefront Sensors (Shack-Hartmann Sensors). WFS Series. Operation Manual. `http://www.thorlabs.de/Thorcat/19900/19905-D02.pdf`.

[101] QImaging. Retiga-2000R Product Datasheet. `http://www.qimaging.com/products/datasheets/Retiga2000R.pdf`, Date cited: January 13, 2012.

[102] Deepak Vedhachalam. Personal communication with Thorlabs engineer, 2009.

[103] Thorlabs. Thorlabs FM03 Cold Mirror Specifications. `http://www.thorlabs.com/Thorcat/7200/7280-E0W.pdf`, Date cited: January 19, 2012.

[104] M Pircher, R J Zawadzki, J W Evans, J S Werner, and C K Hitzenberger. Simultaneous imaging of human cone mosaic with adaptive optics enhanced scanning laser ophthalmoscopy and high-speed transversal scanning optical coherence tomography. *Optics letters*, 33(1):22–4, January 2008.

[105] Rainer Wegerhoff, Olaf Weidlich, and Manfred Kässens. The resolving power. *Basics of Light Microscopy & Imaging*, (Special Edition).

[106] ICNIRP. ICNIRP statement on light-emitting diodes (LEDS) and laser diodes: implications for hazard assessment. International Commission on Non-Ionizing Radiation Protection. *Health Physics*, 78(6):744–752, 2000.

[107] M V R K Murty. The use of a single plane parallel plate as a lateral shearing interferometer with a visible gas laser source. *Applied Optics*, 3(4):531, 1964.

[108] Thorlabs. Thorlabs shearing interferometer overview. `http://www.thorlabs.com/NewGroupPage9.cfm?ObjectGroup_ID=2970&gclid=CPmEqaieoK4CFQEa4QodjE0j4A`, Date accessed: February 15, 2012.

[109] Boston Micromachines Corporation. Boston Micromachines Corportation Multi-DM Specifications Sheet.

[110] Luo Gang, Opas Chutatape, and Shankar M Krishnan. Detection and measurement of retinal vessels in fundus images using amplitude modified second-order Gaussian filter. *IEEE Transactions on Biomedical Engineering*, 49(2):168–172, 2002.

[111] A Numerical Tour of Signal Processing: Image Denoising with Linear Methods - File Exchange - MATLAB Central. `http://www.mathworks.com/matlabcentral/fileexchange/9554-a-numerical-tour-of-signal-processing/content/numerical-tour/denoising_linear/index.html`, Date cited: July 02, 2012.

[112] Olshausen Bruno. Power Spectrum calculation - VS212B - Lab #2. `http://redwood.berkeley.edu/bruno/VS212B/lab2/lab2.html`, Date cited: July 02, 2012.

[113] M Glanc, E Gendron, F Lacombe, D Lafaille, J.-F Le Gargasson, and P Léna. Towards wide-field retinal imaging with adaptive optics. *Optics Communications*, 230(4-6):225–238, February 2004.

[114] Joy Hirsch and Christine A. Curcio. The spatial resolution capacity of human foveal retina. *Vision Research*, 29(9):1095–1101, January 1989.

[115] R Matthes, C P Cain, D Courant, D A Freund, B A Grossman, P A Kennedy, D J Lund, M A Mainster, A A Manenkov, and W J Marshall. Revision of guidelines on limits of exposure to laser radition of wavelengths between 400 nm and 1.4 micron. *Health Physics*, 79(4):431–440, 2000.

[116] François C Delori, Robert H Webb, and David H Sliney. Maximum permissible exposures for ocular safety (ANSI 2000), with emphasis on ophthalmic devices. *Journal of the Optical Society of America A*, 24(5):1250–1265, 2007.